ROLE OF LOCAL THERMODYNAMIC COUPLING IN THE LIFE CYCLE OF THE INTRASEASONAL OSCILLATION IN THE INDO-PACIFIC WARM POOL

A Thesis
Presented to
The Academic Faculty

by

Paula A. Agudelo

In Partial Fulfillment
of the Requirements for the Degree
Doctor of Philosophy in the
School of Earth and Atmospheric Sciences

Georgia Institute of Technology
December 2007

ROLE OF LOCAL THERMODYNAMIC COUPLING IN THE LIFE CYCLE OF THE INTRASEASONAL OSCILLATION IN THE INDO-PACIFIC WARM POOL

Approved by:

Dr. Judith A. Curry, Advisor
School of Earth and Atmospheric Sciences
Georgia Institute of Technology

Dr. Peter J. Webster
School of Earth and Atmospheric Sciences
Georgia Institute of Technology

Dr. Annalisa Bracco
School of Earth and Atmospheric Sciences
Georgia Institute of Technology

Dr. Rong Fu
School of Earth and Atmospheric Sciences
Georgia Institute of Technology

Dr. Carol Anne Clayson
Department of Meteorology
Florida State University

Date Approved: 21 August 2007

A mi Familia,

Por todo el amor, apoyo y confianza

A Carlos,

Novio ni modo, te toco quedarte conmigo el resto de la vida pa'ver si alcanzo a agradecerte todo lo que has hecho por mi :)

ACKNOWLEDGEMENTS

I would like to thank my advisor, Dr. Judith Curry for her support and guidance as well as Dr. Peter Webster for his enlightening academic discussions and ideas.

I want to thank Dr. Carol Anne Clayson for providing me the ocean model and for all her help.

Thanks to the members of my committee for taking the time to read the thesis and for their useful comments and suggestions.

I want to thank my family (la mamá, el papá, pepín, juancho, y santy) for all their effort to give me a good education that allowed me to get to this point. Also for all their love and trust during all these years.

Finally, I'd like to thank Carlos ("el novio") for being with me, helping me with everything he could and more. For being my support in the difficult times and also for enjoying the good moments with me. For his academic ideas and help which got me out of trouble many times. For his love, trust and company.

TABLE OF CONTENTS

LIST OF TABLES

LIST OF FIGURES

SUMMARY

Intraseasonal oscillations (ISOs) are important elements of the tropical Indo-Pacific climate with time-scales in the 20-80 day period range during which time they modulate higher frequency tropical weather. The ISO is poorly simulated and predicted by numerical models. This work presents a joint diagnostic and modeling study of the ISO that examines the hypothesis that local coupling between the ocean and the atmosphere is essential to the existence and evolution of the intraseasonal oscillation in the Indo-Pacific warm pool region. It is found that during the transition between the suppressed and active periods of the ISO, the ocean and the atmosphere undergo gradual, but large-scale and high-amplitude changes, especially the moistening of the lower troposphere by the anomalously warm sea surface temperature arising from minimal cloud coverage and weak winds during the suppressed phase and the large-scale subsidence that inhibits the formation of deep convection locally. The low-level moistening preconditions the atmosphere for deep convection. The regional and local vertical structure of ISO from numerical forecasts using the ECMWF coupled model during different phases of the oscillation as well as the skill of the numerical model in simulating the processes that occur during the transition from suppressed to active convection were studied. Results suggest that forecast skill of the tropospheric vertical structure associated with the ISO is greater for winter ISO cases than for summer events. Predictability of the convective period is poor when initialized before the transitional phase. However, when initialized within the transition period including lower tropospheric moistening, predictability increases substantially, although the model convective parameterization appears to trigger convection too quickly without

allowing an adequate buildup of CAPE during the transition. The model tends to simulate a relatively more stable atmosphere compared to data, limiting the production of deep convective events associated with the ISO. Two different one-dimensional coupled models are used to analyze the role of local ocean-atmosphere coupling in generating ISO. In both models, the ocean component is a one-dimensional mixed layer model. In the first model the atmospheric component corresponds to the SCCM. Results suggest that convection in the model tends to be "overactive," inhibiting development of lower frequency oscillations in the atmosphere. In the second case, the atmospheric component is a semi-empirical one-dimensional model that allows reproducing the coupled ISO over long integration periods including only local mechanisms and without convective parameterization. In the semi-empirical scheme the rate of change of atmospheric variables is statistically related to changes in SST. The stable state of this simple model is a quasi-periodic oscillation with a time scale between 25 and 80 days that matches well the observed ISO. Further experimentation suggest that the dominant period of the oscillation depends on the characteristics of the ocean mixed layer, with a higher frequency oscillation for a shallow mixed layer and vice versa.

CHAPTER I

INTRODUCTION

Tropical convection, especially over the Indo-Pacific warm pool, plays a significant role in global redistribution of heat, moisture and momentum (e.g., Webster 1994, Lin and Johnson 1996). Not only does this region possess the warmest open-ocean sea surface temperature (SST) and the largest annual precipitation on the planet, but also the associated latent heat drives global-scale atmospheric circulation patterns (e.g., Webster 1972, Gill 1980).

Throughout the Indo-Pacific warm pool region, large amplitude variability is evident in surface and upper tropospheric winds, precipitation, radiation, latent and sensible heat fluxes. The intraseasonal oscillation (ISO) comprises a large fraction of the observed tropical variability. Referred alternatively as the Madden-Julian oscillation (MJO), the ISO is usually manifested as an eastward propagating planetary scale convective wave (Madden and Julian 1972, 1994). The ISO is strongest and most frequent during the boreal winter and spring (e.g. Zhang 2005). This eastward propagating convective anomaly typically originates in the Indian Ocean; weakens as it moves across the maritime continent, and re-intensifies in the western Pacific warm pool region. During the boreal summer the oscillation has a slightly different nature in its convective signal over the Indian Ocean, interacting with the Indian summer monsoon (e.g. Lawrence and Webster 2002, Hoyos and Webster 2005). In addition to a generally west to east propagation, the convective mode tends to bifurcate in the eastern Indian Ocean with modes propagating poleward in each hemisphere. The northern hemisphere mode becomes the active phase of the South Asian monsoon. During summer, intraseasonal variability is also very important especially over

the Indian Ocean. Summer ISO not only modulates the rainfall associated with the South-East Asian Monsoon but also plays an important role defining the average spatial structure of the overall summer rainfall as well as introducing internal interannual variability in the monsoon system (Hoyos and Webster 2007).

During the boreal winter there is some evidence that the mode circumnavigates the entire globe in the vicinity of the equator before attaining strong convective characteristics in the equatorial Indian Ocean (Hendon and Salby 1994). The detailed structure of the ISO is very complicated. Contrary to the eastward movement of the ISO system, individual cloud clusters propagate westward as sets of short Rossby waves moving through the ISO packet (Nakazawa 1988). Whereas the ISO has the structure of equatorially trapped modes, it does not project directly onto any normal mode structure for reasonable values of equivalent depth (e.g., Wheeler and Kiladis, 1999). Rather, the mode appears to propagate eastward more at the phase speed of an ocean Kelvin wave than its atmospheric counterpart.

In general, the variability in convection associated with the ISO is characterized by periods of organized deep convective systems referred to as "active" phases, and periods of isolated, shallow convective systems known as "suppressed" phases. Oceanic responses to ISO-related atmospheric forcing have also been observed in sea surface temperature, subsurface temperatures, oceanic currents, and the mixed layer depth (e.g., Zhang and McPhaden 2000; Woolnough et al. 2000).

Several weather and climate phenomena have been related to the different phases and characteristics of the ISO. The onset and break activity of the Asian-Australian monsoon system is strongly influenced by the propagation and evolution of ISO events (e.g., Yasunari 1980; Lau and Chan 1986; Hendon and Liebmann 1990). The passage of ISO events over the western Pacific Ocean has been found to significantly modify the thermocline structure in the equatorial eastern Pacific Ocean via their connection to westerly wind bursts (e.g., McPhaden and Taft 1988; Kessler et al. 1995; Hendon

et al. 1998), potentially playing an important role in triggering variations in El Niño-Southern Oscillation (e.g., Lau and Chan 1988; Weickmann 1991; McPhaden 1999; Kessler and Kleeman 2000). The weather in different regions is also influenced by the ISO. The development of persistent North Pacific circulation anomalies during Northern Hemisphere winter has been linked to the evolution and eastward progression of convective anomalies associated with ISO events (e.g., Weickmann 1983; Liebmann and Hartman 1984; Higgins and Schubert 1996; Higgins et al. 1997; Mo 2000). In fact, a link has been shown to exist between rainfall variability along the western United States, including extreme events, and the longitudinal position of ISO convective anomalies (Mo and Higgins 1998a,b; Jones 2000; Whitaker and Weickmann 2001). In addition, ISO convective activity has been linked to Northern Hemisphere summertime precipitation variability over Mexico and South America as well as to wintertime circulation anomalies over the Pacific-South American sector (Nogues-Paegle and Mo 1997; Jones and Schemm 2000; Paegle et al. 2000). Other studies have also shown that particular phases of the ISO are more favorable than others in regards to the development of tropical storms/hurricanes in both the Atlantic and Pacific sectors (Maloney and Hartmann 2000; Mo 2000; Higgins and Shi 2001). All this regional and global effects of the ISO reinforce the necessity of a clear understanding of all its different phases and the potential importance of the ocean-atmosphere coupling in its development and evolution.

Many attempts to simulate the ISO by numerical models have met with difficulties in reproducing its characteristics or obtaining realistic propagation speed in case of the MJO. Comparisons of the ISO in 15 general circulation models (GCMs) as part of the Atmospheric Model Intercomparison Project (AMIP; Slingo et al. 1996) indicated that most GCMs have weaker than observed intraseasonal activity; they tended to simulate slightly shorter periods than observations and failed to capture the seasonality of the oscillation. Inness and Slingo (2003) note that many general

circulation models (GCMS) produce some aspects of the ISO but all have problems with determination of the amplitude, the propagation speed, and reproducing the different seasonal aspects. Subsequent studies (Waliser et al. 2003a, b) have found similar model behavior in which models tend to lose the spectral peak associated with the ISO. However, empirical prediction studies (e.g., Webster and Hoyos 2004, Jones et al. 2004) have shown that there is predictability of the ISO.

Lin et al. (2006a) evaluated the tropical intraseasonal variability in 14 CGCMs participating in the Inter-governmental Panel on Climate Change (IPCC) Fourth Assessment Report (AR4). The results showed that current state-of-the-art GCMs have significant problems in simulating tropical intraseasonal variability. In most of these 14 models the total intraseasonal variance of precipitation is too weak. The MJO variance approaches the observed value in only 2 of the 14 models, and is less than half of the observed value in the other 12 models. Also there is lack of the coherent eastward propagation of the MJO. Moreover, the MJO variance in 13 of the 14 models does not come from a pronounced spectral peak, but usually comes from part of an over-reddened spectrum, which in turn is associated with too strong persistence of equatorial precipitation (Lin et al. 2006a). The fidelity of MJO simulations in other models not include in the IPCC study were also tested by Lin et al. (2006b), these seasonal-to-interannual prediction models are the ECMWF, Meteo France, and UKMO. This study shows that the MJO variance approaches the observed value in the Meteo France model, but is less than half of the observed value in ECMWF and UKMO models. Too weak precipitation variance in the MJO wavenumber-frequency band has been a long-standing problem in GCMs, in spite of the fact that many of these models have reasonable values of zonal wind variance. The Meteo France model displays a highly coherent eastward propagating signal, although the phase speed is too slow. The ECMWF and UKMO models primarily show standing intraseasonal oscillations.

Factors hypothesized to be important for MJO simulations by Lin et al. (2006a) include model physics, model resolution, and air-sea coupling. Previous modeling studies showed that MJO simulations are quite sensitive to changes in model physics like the vertical heating profile (Park et al. 1990; Lin et al. 2004), cloud radiative heating (Lee et al. 2001; Lin and Mapes 2004) and the deep convection scheme (Slingo et al. 1996). Also MJO simulation has been found to be improved when using higher horizontal resolution (e.g., Kuma 1994) and/or vertical resolution (Inness et al. 2001). Hoyos and Webster (2007) found evidence suggesting that high frequency errors introduced by the convective parameterization erode the envelope of intraseasonal variability in the model considerably reducing its skill.

During the last years some models have been able to better represent the MJO variance and/or to have more coherent eastward propagation, however Waliser et al. (2003c), pointed that when a model does exhibit a relatively good MJO, one can at best only give vague or plausible explanations for its relative success. This inhibits the extension of the success of a model success to others, even its future versions.

In the last decades the interaction of the atmospheric component of the ISO and the near-surface ocean has become increasingly important with regard to our understanding of both weather and climate and the ability to simulate them. This is especially due to the ISO's extensive interactions with other components of our weather/climate system, in conjunction with evidence that air-sea coupling may play an important role in defining the characteristics of the ISO. There is a growing interest in the role that SSTs may play in the simulation, maintenance, and propagation of the ISO. Many theoretical studies of the ISO have assumed a background state in which SSTs remain fixed (Emanuel 1987; Neelin et al. 1987; Lau and Peng 1987; Chang and Lim 1988; Hendon 1988) often having difficulties representing some of the prominent features since coupled processes between surface heat fluxes and the SSTs have not been accounted for and given the significant variability in surface

heat fluxes and SSTs on intraseasonal time scales (e.g., Krishnamurti et al. 1988; Zhang 1996; Lau and Sui 1997; Jones et al. 1998). These studies and the problems that they found in simulating the oscillation, suggest that SST and its variations on intraseasonal time scales have the potential to significantly impact the ISO and possibly provide a positive feedback (Lau et al. 1997; Jones et al. 1998) strengthening the power of the oscillation and influence its eastward propagation (e.g., Kawamura 1991, Jones and Weare 1996; Flatau et al. 1997; Lau and Sui 1997). An example of the impact of SST variability in the framework of a numerical experiment is presented by Kim et al. (2007), where the same atmospheric model was forced with SST of different time resolution (monthly, weekly and daily), finding better representation and predictability of the MJO when using daily SST as boundary conditions for the AGCM. However, the lack of coupling between ocean and atmosphere results in an unrealistic phase in the relationship between SST and convection.

Understanding the role of coupling of the atmosphere would in fact be necessary for the prediction of the ISO, since the air-sea interaction would alter the structure, period, and coherence of the oscillation (e.g., Flatau et al. 1997; Waliser et al. 1999). Recent observational and modeling studies have suggested that interactions between the ocean and the atmosphere may be important elements of the ISO. Webster (1994) showed strong relationships between wind strength, insolation and the magnitude of the SST and the total heat content of the upper ocean. These interactions are central to the ISO feedbacks that determine the 20-50 day time scale of the ISO (Stephens et al. 2004). Clayson and Chen (2002) point out that the SST and the ocean mixed layer structure are both very sensitive to variations in surface fluxes. This sensitivity places a large obligation on model fidelity because a number of studies (e.g., Palmer and Mansfield 1984) have found that, in turn, the atmospheric circulation is very sensitive to small changes in SST in the Indo-Pacific warm pool region.

However some studies (Kemball-Cook et al. 2002) still argue that it is not clear

from observational analyses whether the air-sea interaction is fundamental to the existence of the ISO, is merely a by-product of it, or plays a supporting role, such as intensification and organization of the disturbance. Kemball-Cook et al. (2002) suggest that the ISO is primarily a mode of the atmosphere, and that the ISO does not rely upon coupling between the ocean and atmosphere for its existence. However, interaction with the sea surface, while not critical for the existence of the ISO plays a role in its organization and intensification, and also in the setting of its phase speed. Why models tend to fail in simulating the ISO as said before is difficult to determine. A possible cause may be the inability of a numerical models to simulate adequately the properties of clouds and their interaction with the lower boundary during the life cycle of the ISO or the interaction of the atmosphere with the upper ocean (e.g., Flatau et al. 1997; Wang and Xie 1998; Waliser et al. 1999). Changes in cloud cover associated to ISO events affect both the atmospheric and oceanic boundary layers through a variety of possible feedbacks that involve precipitation, wind speed, and sea surface temperature (e.g., Webster et al. 1996). Different cloud types play different roles in the climate, with convective clouds providing the dominant contribution to precipitation and the layered clouds with the large horizontal extent having a grater influence on the radiative fluxes (e.g., Liu et al. 1995). Johnson et al. (1999) showed that three cloud types, cumulus, congestus, and cumulonimbus, are important components of the tropical convective cloud spectrum, and that these three cloud populations vary significantly with a timescale of 30-60 days. , Wang et al. (2005) analyzed cloud variations during the summer ISO in terms of cloud top temperature. Overall, cloud related feedbacks in the climate system are not well understood, and these uncertainties are considered to be one of the major obstacles in the prediction of climate variability and climate change (e.g. Stephens et al. 2002). Specifically, with respect to the ISO, cloud feedbacks are even less well understood. Kikuchi and Takayabu (2004) have classified convection in different stages of the ISO

using cloud top temperatures to define suppressed, developing, mature, and decaying stages. To that extent, the cloud characteristics of the ISO are well described. A more detailed description of cloud-dynamic interactions has been attempted by Stephens et al. (2004). They define a classification of stages during ISO, which include a destabilization phase, a convective phase, and a restoring phase. Stephens et al. (2004) proposed a feedback cycle between the ocean, the evolving structure of the troposphere and the related cloudiness to explain the transition from one stage of the ISO to the next. Similar cycles for the Indian Ocean ISOs have been proposed by Wang et al. (2005) using TRMM data. Wang et al. (2005) and Stephens et al (2004) argue that the ISO is an instability of the coupled ocean-atmosphere system of the warm pools that is critical for the maintenance of their climatological structure. Stephens et al. (2004) referred to the ISO as a "self-regulating oscillator" and defined a "destabilization" phase that rendered the system amenable for a subsequent "convective" phase. The convective phase was followed by a "restoring" phase where the system stabilizes before entering into another period of destabilization. The period of time needed to destabilize the lower troposphere through the warming of the SST (by enhanced downward solar radiation during the suppressed phase) and the cooling of the upper troposphere (enhanced long-wave cooling) determined the time scale of the ISO. Wang et al. (2005) added a spatial aspect to the self-regulating oscillator of Stephens et al (2004). They noticed that the ascending region of the convective phase of the ISO in the eastern Indian Ocean produced a region of strong subsidence in the western basin, prompting a reduction of cloudiness and a destabilization period similar to the Stephens et al. concept. In this manner one part of the oscillation was producing the next ISO. Wang et al. (2005) referred to this sequence as "self-induction". The two theories are complementary and both point to the transition period between the suppressed and convective stages of the oscillation as critical elements of the ISO. It is important to note that both the self-regulating oscillation and

the self-induction theories refer to the coupled ocean-atmosphere system. Indeed, a number of studies have shown ocean responses to ISO-related atmospheric forcing observed in sea surface temperature, subsurface temperatures, oceanic currents, and the mixed layer depth (e.g., Lukas and Lindstrom 1991, Webster 1994, Zhang and McPhaden 2000; Woolnough et al. 2000, Loschnigg and Webster 2000).

In the present study, we hypothesize that physical processes occurring in the transition between the suppressed and active phases are critical to the development of the onset and evolution of the ISO. To test this hypothesis, a diagnostic study is conducted with a concentration on the transition phase between the suppressed and active periods of convection. Using data collected during the intensive observing period (IOP) of the Tropical Ocean Global Atmosphere (TOGA) Coupled Ocean-Atmosphere Response Experiment (COARE: Webster and Lukas, 1992), the general features of two ISO events during the IOP, as well as a diagnostic study of different variables involved in the corresponding transition stages are described in Chapter 2. Chapter 2 also includes analysis of the populations of different types of clouds occurring during the ISO phase transitions, obtained by using a cloud classification scheme. Chapter 3 evaluates and interprets the performance of an experimental ensemble simulation using the European Centre for Medium-Range Weather Forecasts (ECWMF) coupled climate model in the transition stages during the IOP and during a summer ISO events during 2002 and 2004. Specifically, in this study it is argue that it is essential that Stephens et al.'s destabilization period be modeled correctly for the appropriate degree of convective available potential energy (CAPE) to be built up in order to allow the correct time-scale of the ISO to be modeled. If this does not occur, it is speculated that weak and short period oscillations ensue. To test this hypothesis, a combined diagnostic and coupled ocean-atmosphere modeling study is conducted with a concentration on the transition phase between the suppressed and active periods of convection.

In chapter 4 a numerical experiment using a coupled single column model is conducted to study the role of the atmosphere and the ocean, as well as their interaction, in triggering and sustaining the low-level moistening present during the transition periods associated to intraseasonal activity. The atmospheric component of the couple system corresponds to the single column model version of the NCAR Community Climate Model 3.6 (SCCM). The ocean component is the one-dimensional ocean mixed layer model described by Kantha and Clayson (1994, 2004). In this framework, the evolution of the transition period is studied under several different ocean-atmosphere configurations.

In Chapter 5 we study the role of local ocean-atmosphere coupling in generating intraseasonal variability. The role of the oceanic mixed layer dynamics in determining the time-scale of the resulting oscillation is also revised. For this study a semi-empirical single column model is designed. In this model the atmospheric component is an empirical scheme in which the rate of change of atmospheric variables is statistically related to changes in SST. Discussion and conclusions of this work are presented in Chapter 6.

CHAPTER II

DIAGNOSTICS OF THE TRANSITION BETWEEN SUPPRESSED TO ACTIVE PHASES OF INTRASEASONAL OSCILLATIONS IN THE INDO-PACIFIC WARM POOL

To address the crucial role of the Pacific warm pool in determining the state of the global climate, extensive measurements were carried out during the intensive observing period (IOP) of the Tropical Ocean Global Atmosphere (TOGA) Coupled Ocean-Atmosphere Response Experiment (COARE: Webster and Lukas, 1992), from November 1992 to February 1993. In this chapter we use high resolution observations from TOGA COARE to study processes occurring during the transition phase from suppressed to active convection for both the ISOs that occurred during this period and to present analyses that will be used in the following section to be compared with the model simulations.

One of the main objectives of the IOP was the determination of the principal processes responsible for the coupling of the ocean and the atmosphere in the western Pacific warm pool region (Webster and Lukas 1992). The experiment provided extensive observations of the coupled ocean-atmosphere tropical warm pool system (Godfrey et al. 1998), leading to an identification of dominant physical processes determining the mean state of the warm pool and its intraseasonal variability. TOGA COARE provided the first detailed observations of the large amplitude intraseasonal oscillations (ISOs, or alternatively Madden-Julian Oscillations MJOs) of the Indo-Pacific warm pool evident in lower and upper tropospheric winds, cloudiness, precipitation and surface atmosphere-ocean radiative and turbulent heat fluxes.

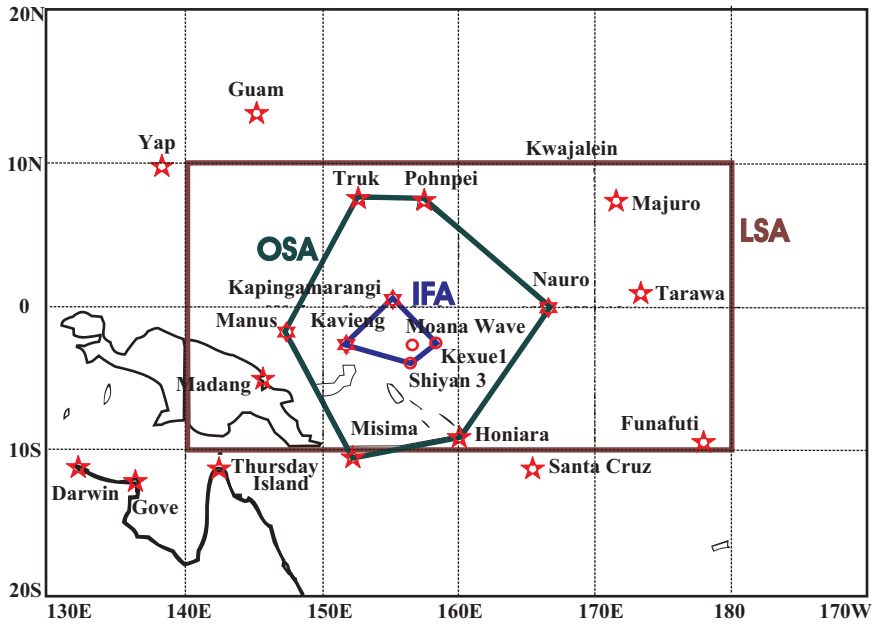

Figure 1: Domains of the TOGA COARE IOP the large-scale array (LSA), the outer sounding array (OSA) and the intensive flux array (IFA).

The observational network (Figure 1) consisted of three spatially overlapping observational arrays, the large-scale array (LSA), the outer sounding array (OSA) and the intensive flux array (IFA). The interactions between the larger-scale circulation of the atmosphere and ocean were measured by the LSA. Mesoscale circulations associated with convection in the atmosphere were resolved by the OSA and the IFA. The IFA was centered at 2°S, 156°E and was bounded by a polygon formed by two islands (Kapingamarangi and Kavieng, Papua New Guinea) and two anchored research vessels (Kexue #1 and Shiyan #3). Located within the IFA was the Improved METeorological surface mooring (IMET; Weller and Anderson 1996). Other research vessels conducted special cruises within the IFA, and a number of research aircraft flights also supplied cloud observations and measurements of other atmospheric properties. Soundings at sites within the IFA were conducted four times daily at 00, 06, 12, and 18 UTC. The TOGA COARE observing strategy and the observing network is described in detail by Webster and Lukas (1992). An overview of the data collected

during the IOP is provided by Godfrey et al. (1998). Soundings over the IFA and the LSA provide detailed information of the vertical structure of the atmosphere during the IOP. Version 2.1 of the IFA-averaged fields and the LSA gridded data set by Ciesielski et al. (2003) was used in this study, which was prepared using the humidity corrected radiosonde data by Wang et al. (2002).

2.1 General features observed during TOGA COARE

2.1.1 Dynamics and thermodynamics

As it has been shown in previous studies (e.g. Lau and Sui 1997; Weller and Anderson 1996; Gutzler et al. 1994), two eastward propagating ISO events were identified in the December 1992-February 1993 period (Figure 2). Heavy precipitation occurred during the last two weeks of December 1992 and later between the end of January and beginning of February 1993 (Figure 3a) resulting from enhanced convection as ISOs propagated across the Pacific warm pool.

The ISO signal also appears in the Outgoing Long-wave Radiation (OLR) field shown in Figure 3b. Estimates of OLR are from the NOAA polar-orbiting satellites (Liebmann and Smith 1996). Negative anomalies of OLR are directly associated with high clouds which, in the tropics, are usually related to disturbed environments, characterized by heavy rainfall, strong ascending motion and enhanced convection. Positive anomalies of OLR denote clear conditions, which in turn indicate the absence of deep convection. Figure 3c to Figure 3f show Outgoing Long-wave Radiation (OLR) anomalies in the intraseasonal band (defined here as the variability between 25-80 days) at different stages of large-scale convection over the western Pacific. Each OLR diagram corresponds to a vertical line in Figure 3a and Figure 3b. Intraseasonal anomalies were obtained using Fourier analysis. Collectively, Figure 2 and Figure 3 show that the two ISOs occurring during TOGA COARE possessed time scales similar to the canonical or average ISO (e.g. Wheeler and Kalidis 1999, Zhang 2005) and

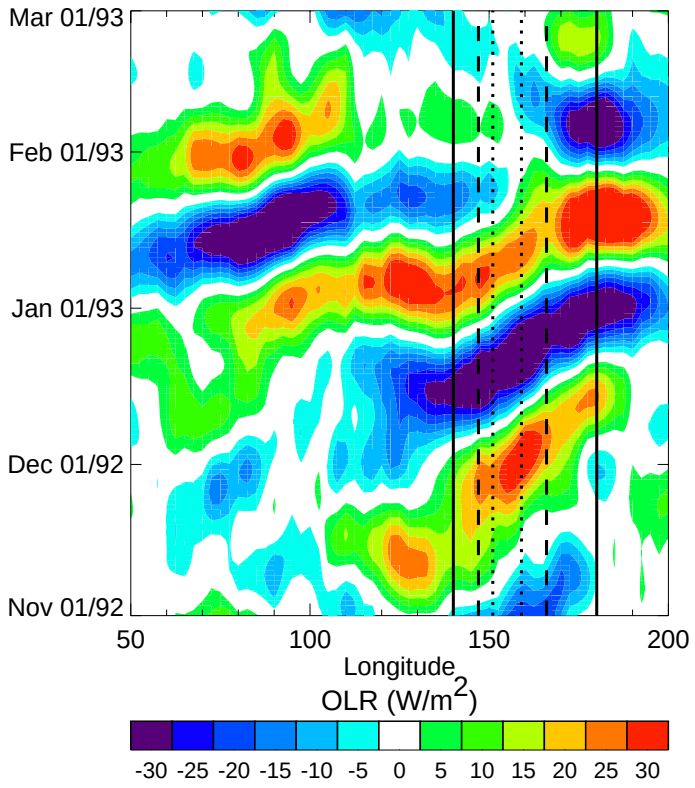

Figure 2: Longitude-time diagram of average OLR during the IOP for latitudes between 10°S and 10°N showing two eastward propagating ISO events. Lines represent the domains of the TOGA COARE IOP: the large-scale array (LSA; solid lines), the outer sounding array (OSA; dashed lines) and the intensive flux array (IFA; dotted lines).

that both suppressed and active convection phases of both ISO events are large-scale features. Figure 3b shows the dates selected based on the filtered OLR time series corresponding to the suppressed (November 25 to December 3 1992 and January 6 to January 15 2003), transition (December 4 to December 17 1992 and January 16 to January 22 2003) and active (December 19 to December 29 1992 and January 23 to January 29 2003) phases of convection during the first ISO event. Although an exact definition of a transition is elusive because of the large degree of intermittency in the atmosphere, the intraseasonal signal within the OLR fields is used as a proxy to define the timing of the transition stage during the TOGA COARE IOP.

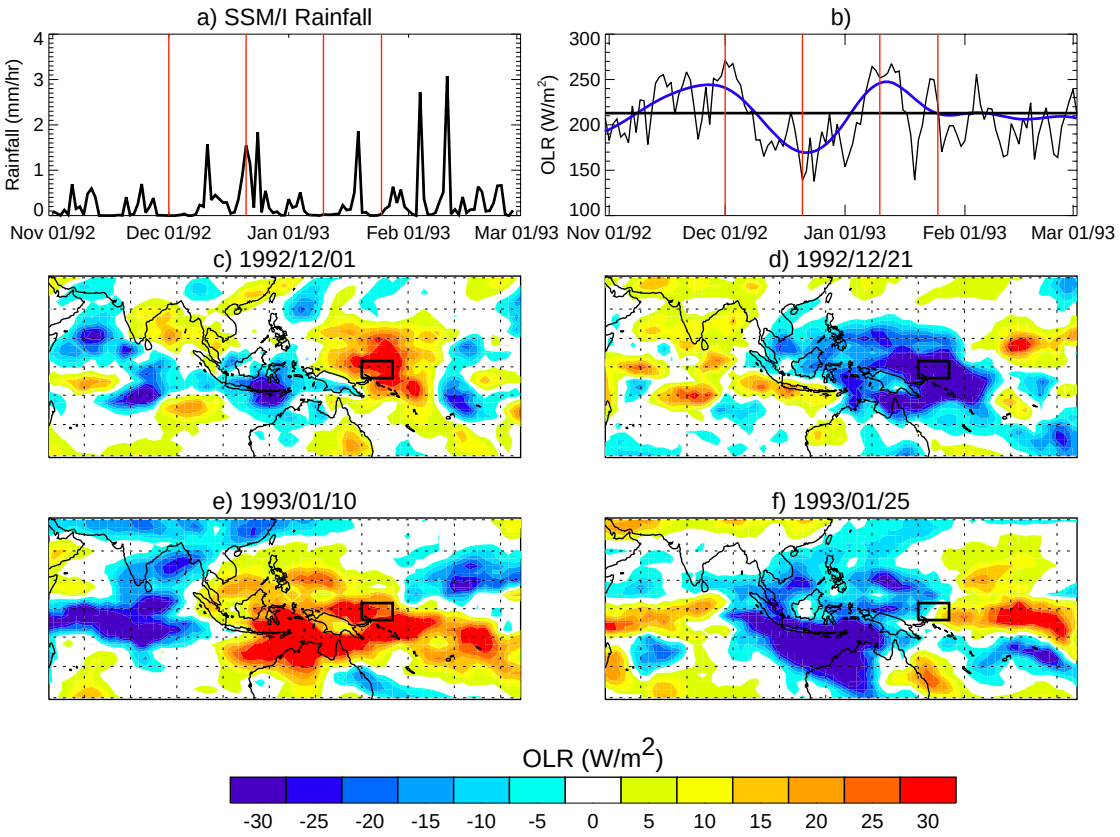

Figure 3: Special sensor microwave/imager (SSM/I; Hollinger et al. 1990) rainfall (mm/hr) time series during the IOP over a region enclosing the IFA (4°S to 2°N, 150°E to 160°E). b) OLR time series during the IOP over the IFA. Horizontal line represents the mean OLR during the IOP. Blue line represents the OLR in the intraseasonal band. Vertical red lines correspond to dates where intraseasonal variability of OLR (W/m^2) is displayed in scenes c) to f). The black rectangle corresponds to IFA.

Figure 4 to Figure 6 show vertical distribution of specific humidity, zonal winds and temperature anomalies over the IFA during the IOP. Anomalies for different phases of the ISO are computed for each level relative to the mean value during whole period. The major features apparent in Figure 4 are associated with the intraseasonal variability. These are anomalously moist and dry periods associated with active and suppressed convection. The mean zonal flow over the IFA is westerly in the lower troposphere and easterly in the upper troposphere (Figure 5). One of the most interesting features is the reversal of the wind anomalies, which occurs throughout

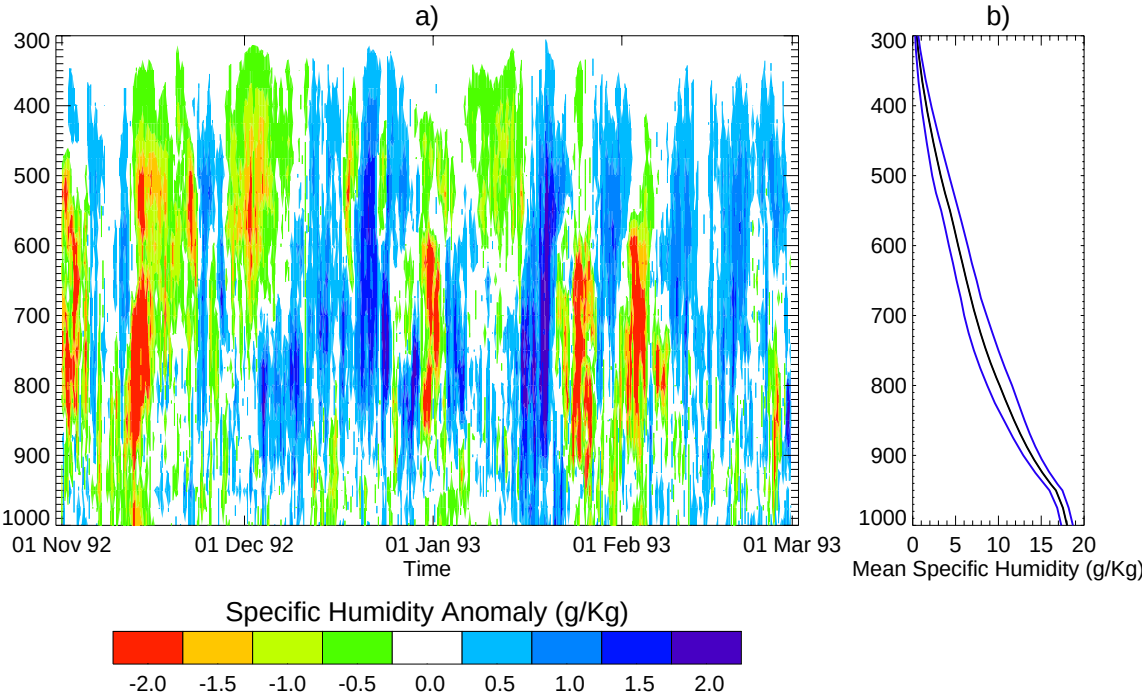

Figure 4: a) Vertical distribution of specific humidity anomalies over the IFA during the IOP computed for each level relative to the mean value for the whole period. b) Mean vertical profile and standard deviation (blue lines) of specific humidity during the whole period.

the entire atmospheric column during the phase transitions of the ISO. Moistening of the atmosphere, precipitation and wind reversal signals are accompanied by warming of the atmosphere, especially significant over 500 hPa (Figure 6).

Table 1 shows the anomalies in the SST, the lower tropospheric zonal wind component, and the OLR, relative to the means for the IOP for three phases of the ISO: suppressed, transitional and convective. It is clear that the major variability of these variables occur on intraseasonal timescales: weak easterlies, a dry and cool middle and upper troposphere characterize the suppressed periods; and strong deep westerlies, a moist middle and upper troposphere and a relatively warm upper troposphere characterize the convective periods.

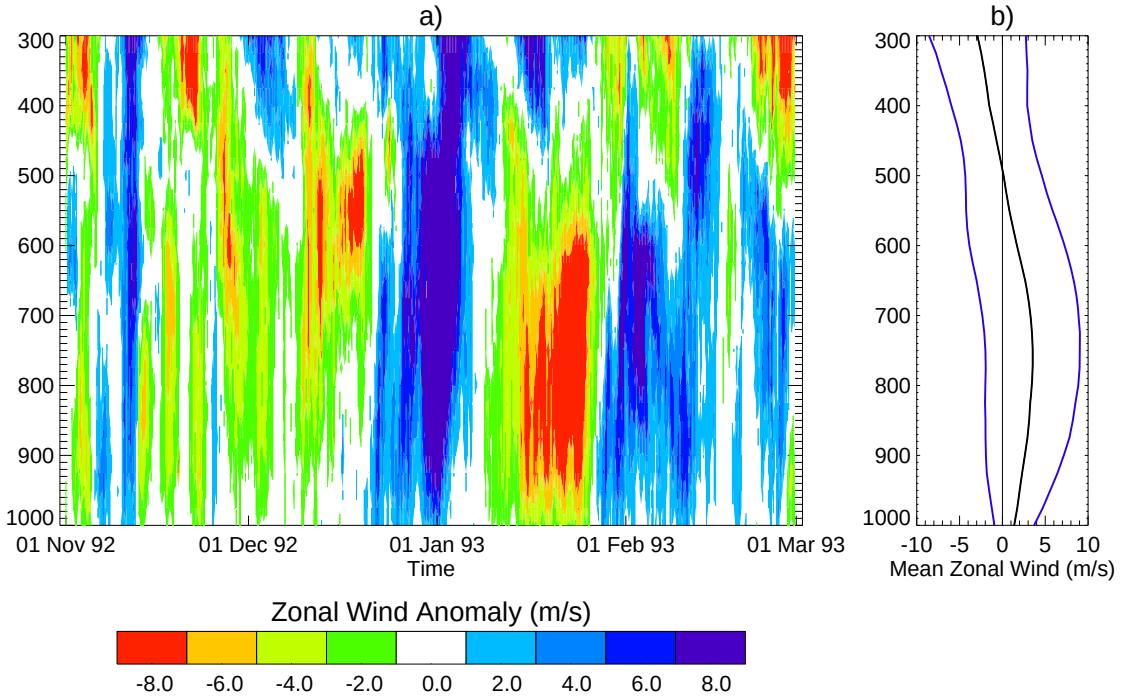

Figure 5: Same as Figure 4 for zonal winds.

Table 1: Average values during the IOP, and during suppressed, transition and active phases relative to the IOP mean.

Variable	Phases			
	IOP	**Suppressed**[1]	**Transition**[2]	**Active**[3]
SST (°C)	29.4	0.42 (0.31)	0.43	-0.32
Zonal wind ($ms^{-}1$)	1.8	-0.54 (-1.81)	0.34	3.2
OLR ($Wm^{-}2$)	213.1	31.9 (36.9)	-15.9	-39.4
Net heat flux ($Wm^{-}2$)	3.3	67.4 (83.1)	8.0	-65.0
Net shortwave radiation ($Wm^{-}2$)	191.3	42.6 (17.4)	3.2	-50.1
Latent heat flux ($Wm^{-}2$)	-115.7	32.3 (57.2)	10.1	-15.4
Specific humidity 900-200mb (g/kg)	5.4	-0.22 (-0.14)	0.23	0.50

[1] November 25 to December 3 1992 (January 5 to January 15 1993), [2] December 4 to December 17 1992, [3] December 19 to December 29 1992.

2.1.2 SST and heat fluxes

Two marked warming phases with maximum SST occurred at the beginning of December 1992 and in mid-January 1993, leading the enhanced convection seen in Figure

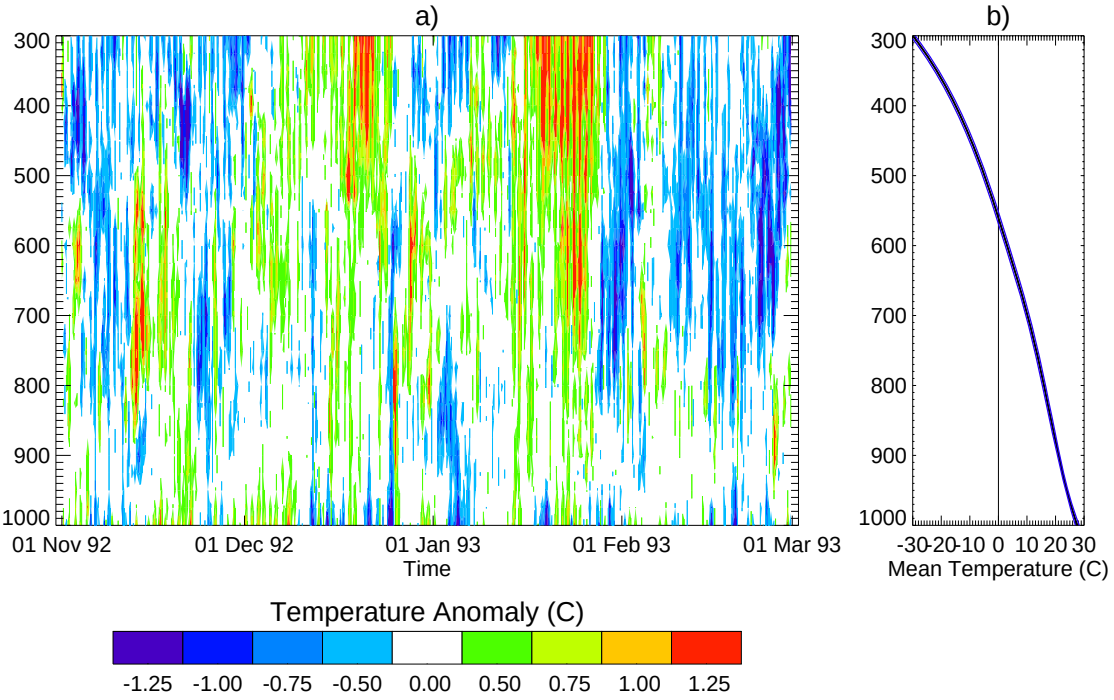

Figure 6: Same as Figure 4 for temperature.

3 by about approximately a week (see Table 1). These positive SST anomalies were followed by a marked cooling, which is especially intense after the first event (late December and early January). In addition, the amplitude of the diurnal variation is severely modulated by the ISO. This is due to the lack of clouds during the suppressed phase, indicating that the intraseasonal activity modulates the amplitude of the SST diurnal cycle (Figure 7a). This warming accompanies an increase in ocean heat storage.

In summary, the SST during the undisturbed periods is warmer than SST during disturbed periods. A number of previous studies have also shown a modulation of the SSTs by the ISO (e.g. Flatau et al. 1997; Lau and Sui 1997, Jones et al. 1998; Woolnough et al. 2000, Stephens et al. 2004, Wang et al. 2005), suggesting that the ISO is a coupled mode of the atmosphere-ocean system. However, how the

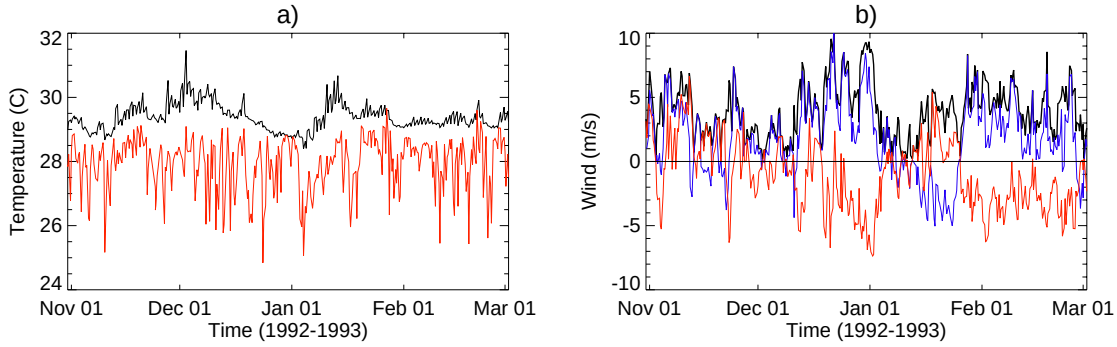

Figure 7: Time series of data from the IMET buoy: a) hourly SST (black line) and atmospheric temperature (red line), b) wind speed (black), zonal wind (blue) and meridional wind (red)

atmospheric part of the ISO modifies the SST and the ocean mixed layer, and how the SST variations feedback on the atmosphere is poorly understood. It is important to note that although the SST over the region remained above 28°C at all times, deep convection did not occur continuously.

Another important feature of the ISO is the strong change, and often a reversal of direction, in surface winds. Figure 7b shows very weak westerlies and easterlies surface winds associated with the suppressed phase of the ISO, and strong westerlies related to the active phase of convection (Table 1). These low-level westerlies, referred to as westerly wind bursts (Lukas and Lindstrom 1991), were especially strong during late December reaching maximum values of 14 ms^{-}1 at the surface. This westerly phase has been attributed to the dynamic response of the atmosphere to the quasi-stationary heating near the date line induced by the ISOs (e.g. Sui and Lau 1992). The IMET buoy located off the equator showed changes in the surface meridional wind, with strong northerlies during the large-scale convective event. These meridional winds are probably associated with the Rossby wave component of the total response to equatorial heating (e.g., Gill 1980).

Associated with the ISO are large amplitude perturbations in surface net heat flux

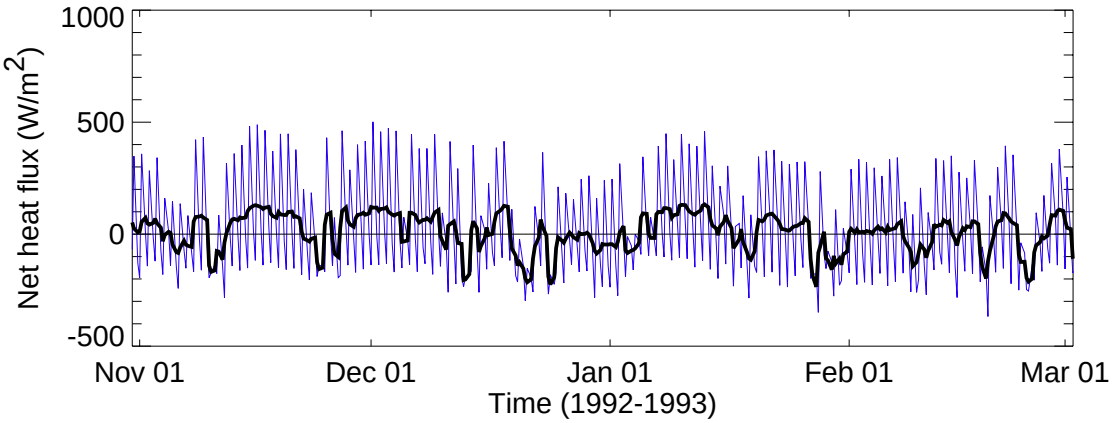

Figure 8: Net heat flux at the surface (blue; positive values indicate warming of the ocean) and 24hr moving average (black) from IMET data.

that play an important role in modifying both the atmosphere and ocean. Figure 8 shows the surface net heat flux computed using IMET data. The net heat flux, Qnet, was computed as the sum of Qsw, the net shortwave radiation, Qlw, the net longwave radiation, Qlat, and Qsen, the latent and sensible turbulent heat fluxes, and Qrain, the sensible flux by rainfall, respectively. Using data from the IMET buoy (Weller and Anderson 1996), Table 1 describes the heat flux components during the different phases of the ISO, with positive values indicating a warming of the ocean. During the undisturbed periods, strong solar radiation and weak winds (low latent heat flux) produce a net heating of the ocean. During disturbed phases, the strong winds and reduced insolation contribute to a net cooling of the ocean. The average value of surface net heat flux during the marked suppressed phase from January 5 to January 15 1993 was +83 Wm^2. In contrast, during the prior convective phase (December 20 to December 30 1992) the net heat flux was -65 Wm^2. These variations are comparable in sign and magnitude to those found for ISOs in other regions of the Indo-Pacific warm pool (Webster et al. 2002). During the suppressed (convective) phase, the average contribution to the warming (cooling), relative to the IOP mean, of the net shortwave radiation and the latent heat flux are about +17 (-50) and +57

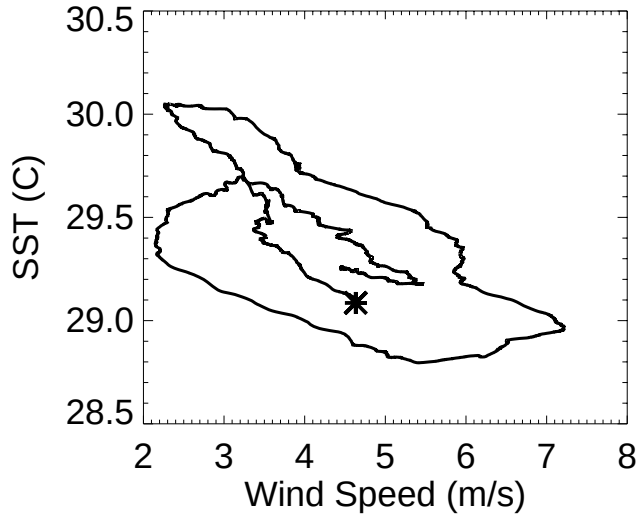

Figure 9: Evolution of SST in wind speed-SST space from November 11 1992 (asterisk) to February 13 1993. IMET time series were smoothed by moving averaging to remove periods shorter less than 12 days.

(-15) Wm^2 respectively. The intraseasonal evolution of SST relative to the strength of the surface winds, which summarizes the sequence of processes described above, can be seen in Figure 9.

2.1.3 Evolution of cloud fields

In order to study the dynamics of different cloud types during ISO events, and their potential impact on the ocean and the atmosphere, a cloud classification scheme developed by Liu et al. (1995) is used (Figure 10). The scheme combines satellite infrared and microwave data. Infrared data are used to determine cloud top temperature, and microwave data are used to determine an index that includes both microwave scattering and emission. The microwave index (f) represents the strength of the microwave signal from a cloudy pixel, and it is a good indicator for rainfall rate and dense ice (Liu et al. 1995). Here, cloud top temperature from GMS-4 and microwave index computed using Special Sensor Microwave/Imager (SSM/I) during TOGA COARE IOP are used. In order to use the classification scheme it is also necessary to separate cloudy from clear-sky pixels. The cloudy/clear pixel information was obtained from

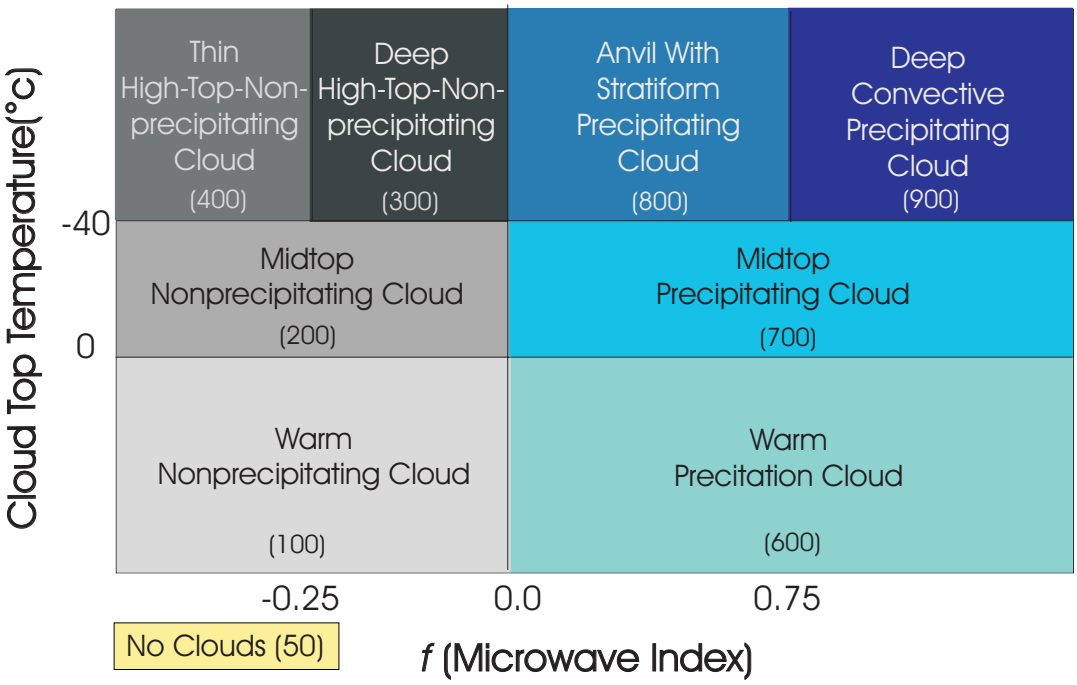

Figure 10: Schematic diagram of Liu et al (1995) cloud classification scheme using microwave index and cloud top temperature.

the International Satellite Cloud Climatology Project (ISCCP; Rossow and Garder 1993).

While the classification scheme generally works well for most of the clouds in the IFA region, different sources of uncertainty are present in the determination of the cloud characteristics presented in the paper. Liu et al. (1995) noted that in general, the classification show good agreement with radar observations for large cloud systems, being able to distinguish between precipitating and non-precipitating clouds. However, the scheme has shown difficulties in resolving the small isolated clouds due to the relatively coarse resolution of the SSM/I data. Also, the determination of threshold values for f and its dependence on dense ice amounts, which is difficult to measure, introduces uncertainty in the separation among high precipitating clouds.

Using the Liu et al. (1995) scheme, clouds were classified into eight different

classes: Warm nonprecipitating cloud, warm precipitating cloud, midtop nonprecipitating cloud, midtop precipitating cloud, thin high-top nonprecipitating cloud, deep high-top nonprecipitating cloud, anvil with stratiform precipitating cloud, and deep convective precipitating cloud. Here the term "midtop" refers to clouds with tops in the middle troposphere. Figure 10 summarizes the cloud top temperature and microwave index ranges characteristic of each cloud type.

On average, within the IFA during the IOP, 20.8% of the pixels were classified as clear and just 14.1% of the pixels were associated with precipitating clouds. Warm nonprecipitating cloud dominated with 30.7% of the pixels, while warm precipitating cloud represented only 0.7% of the pixels. Midtop nonprecipitating clouds occupy 29.9% while midtop precipitating clouds represent 5.8% of the pixels. Among the high clouds, thin high-top nonprecipitating cloud occupying just 0.5% of the pixels, deep high-top nonprecipitating cloud 4%, anvil with stratiform precipitating cloud 6.7%, and deep convective precipitating cloud 0.9%. While it is important to know the average distribution of cloud types for radiation budget studies, the population of different cloud types presents strong variability over several time scales. Analysis of such variability helps to understand the role of clouds in the ocean-atmosphere interaction associated with ISO events. Figure 11 shows daily time series of cloud type over the IFA during the IOP. All types of clouds possess substantial day-to-day variability. Variance in the intraseasonal band represents a major part of the cloud variability.

We now consider the cloud populations during suppressed and convective periods and the transition period from suppressed to convective (Table 2). The amount of cloud-free pixels clearly changes from the suppressed phase (52%) to the convective phase (8%). During the suppressed phase, cloud-free pixels comprise about 60% of all pixels, while during the last two weeks of December, a large-scale deep convective stage, cloud-free pixels were only about 8% of the total pixels. Precipitating clouds

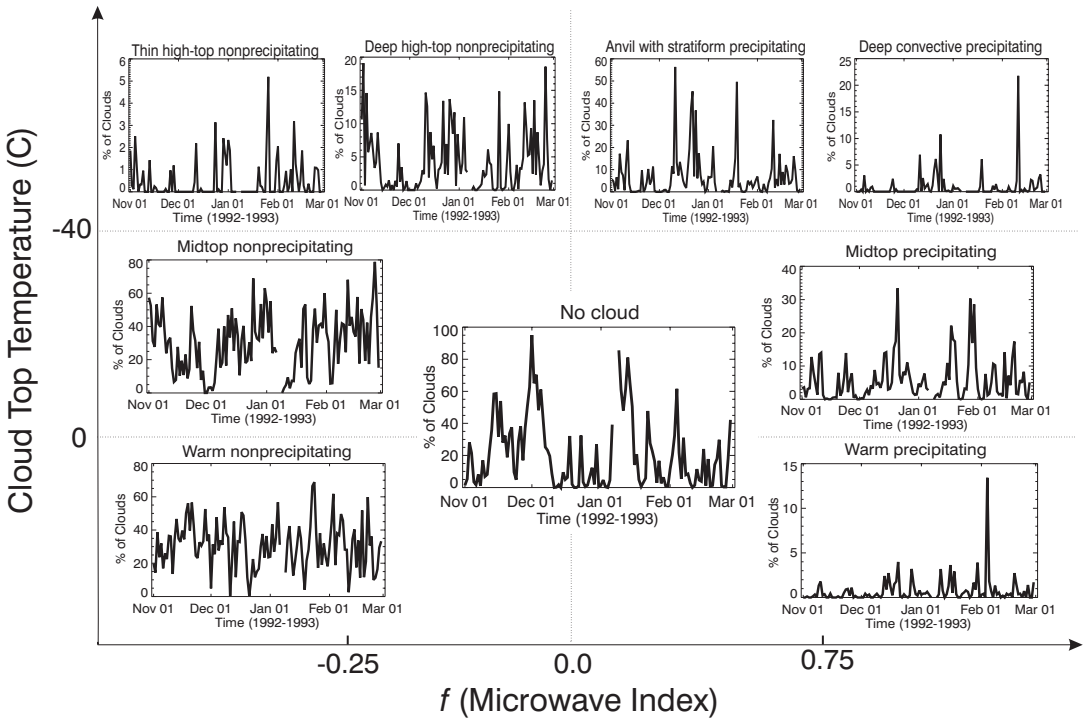

Figure 11: Time series of percentage of each cloud type from Liu et al (1995) cloud classification scheme over the IFA during the IOP.

increase from 4% during the suppressed phase, to 16% during the transitional phase and to 30% during the convective phase. This increase over the life time of an ISO is due mainly to high-top convective clouds. Warm non-precipitating clouds, the dominant cloud type throughout the IOP, are a maximum during the suppressed and transitional period (31 and 33%, respectively), dropping off by almost a factor of two during the convective period (20%). Mid-top non-precipitating clouds, on the other hand, increase by more than a factor of two between the suppressed (12%) and transitional periods (28%).

2.2 Transition phases during TOGA COARE

A detailed examination of the changes in the ocean-atmosphere system during the transition from the suppressed to the active convection stage of the ISO is now undertaken. As said before, although an exact definition of a transition is elusive because

Table 2: Percentage of Cloud Types within the IFA during the IOP, and during suppressed, transition and active phases.

Cloud type	Phases			
	IOP	**Suppressed**	**Transition**	**Active**
1. Warm non-precipitating	31	31	33	20
2. Warm precipitating	1	0.2	1	1
3. Midtop non-precipitating	30	12	28	35
4. Midtop precipitating	6	2	5	10
5. Thin high-top non-precipitating	0.4	0.1	0.2	1
6. Deep high-top non-precipitating	4	1	4	7
7, Anvil with stratiform precipitating	7	2	9	17
8. Deep convective precipitating	1	0.1	1	3
Clear sky	21	52	18	8
Total precipitating clouds	14	4	16	30
Total non-precipitating	62	43	61	56
Total warm	32	31	34	21
Total midtop	36	14	33	45
Total high	13	3	15	28

of the large degree of intermittency in the atmosphere, the intraseasonal signal within the OLR fields are used as a proxy to define the timing of the transition stage during the TOGA COARE IOP. Two such transitions during the IOP were isolated as periods enclosed between a maximum and a subsequent minimum in the intraseasonal OLR time series. These events occurred during the first two weeks of December 1992 and during the second and third week of January 1993.

The dominant feature of the transition is the organized low-level atmospheric moistening. Figure 12 shows details of the moisture build-up within the IFA during both transition stages with moistening gradually extending to the upper troposphere prior to the deep convective event. During the second transition period the moisture appears to build-up or to accumulate more quickly, possibly due to the temporal proximity and effects of the first ISO event. Various studies have suggested that the upward transport of water from the boundary layer into the free troposphere might

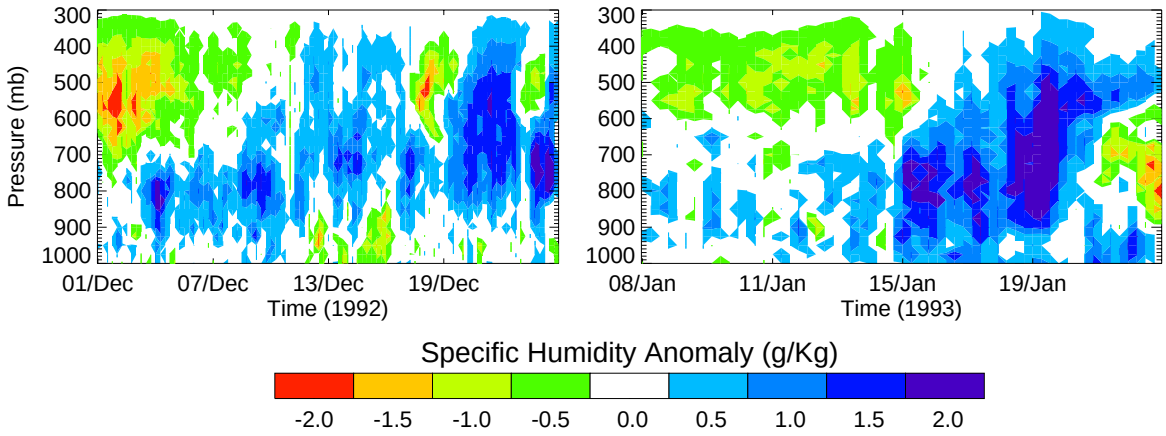

Figure 12: Same as Figure 4a but for both transition periods observed during the IOP.

precondition the atmosphere for deep convection (Hendon and Salby 1994; Maloney and Hartmann 1998; Kemball-Cook and Stephens et al. 2004). The observed low-level moistening noted here is associated with anomalously warm SST during the suppressed and transitional period and increasing low-level winds throughout the transitional period, both of which enhance evaporation (Table 1). However, without a suitable large-scale circulation pattern, the instability of the vertical will rapidly be rectified and large values of convective available potential energy (CAPE) necessary to fuel the extended convective stage will not materialize. During the transition period, the SST reaches a maximum due to the lack of cloud cover and weak surface winds, and then slowly decreases as a result of increasing low-level winds promoting enhanced turbulent latent heat flux (Figure 13).

In order to study the large-scale vertical structure of the low-level moistening, sounding data from the LSA data was used (Figure 1). Figure 14 shows the vertical distribution of specific humidity anomalies at 0° 146°E, as well as longitude-pressure sections along the equator. Although there is day-to-day variability in specific humidity, Figure 14a shows, in the same way as Figure 4, organized low-level moistening of the atmosphere prior to the deep convection.

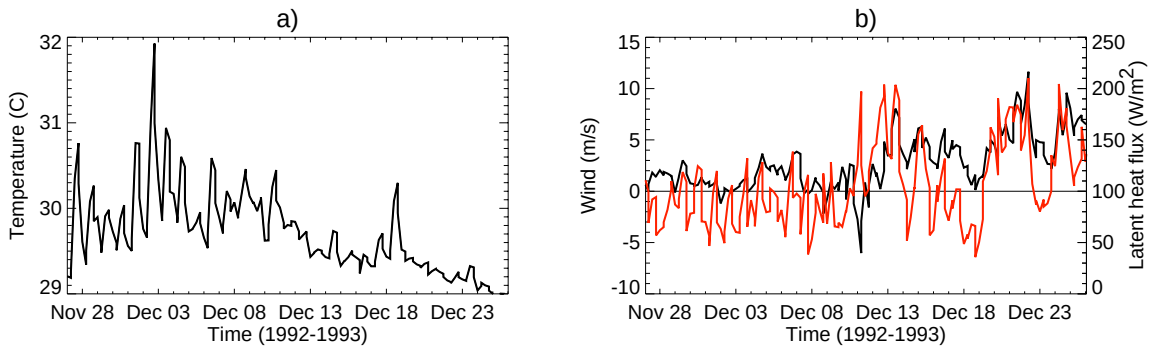

Figure 13: Time series of a) hourly SST, b) zonal wind speed (black), and turbulent latent heat flux (red) during the first transition period. All data were collected by IMET buoy (Weller and Anderson 1996).

Longitude-pressure sections along the equator at key stages of the first ISO reveal the large-scale nature of the atmospheric moistening. Figure 14b corresponds to a transition stage from suppressed to active convection, and clearly shows the presence of low-level (below 700 hPa) moistening of the atmosphere, while the upper troposphere appears dryer than normal. Atmospheric subsidence above 800 hPa, represented by black continuous contours, appears as a key factor during the transition as it inhibits deep moistening of the atmosphere. The combination of enhanced evaporation due to stronger low level winds and warmer SST with large scale subsidence results in the organized moisture build-up. On the other hand, during the deep convective phase, positive anomalies of moisture extend throughout the tropopause accompanied by ascending air (Figure 14c). During periods of suppressed convection and strong subsidence (Figure 14d), the entire atmospheric column appears anomalously dry. Similar features are observed for the second transitional period (see Figure 15a-d).

The processes occurring during the transition phase help destabilize the atmosphere and are associated with increasing values of the convective available potential energy (CAPE). On the other hand, processes associated with the active phase lead

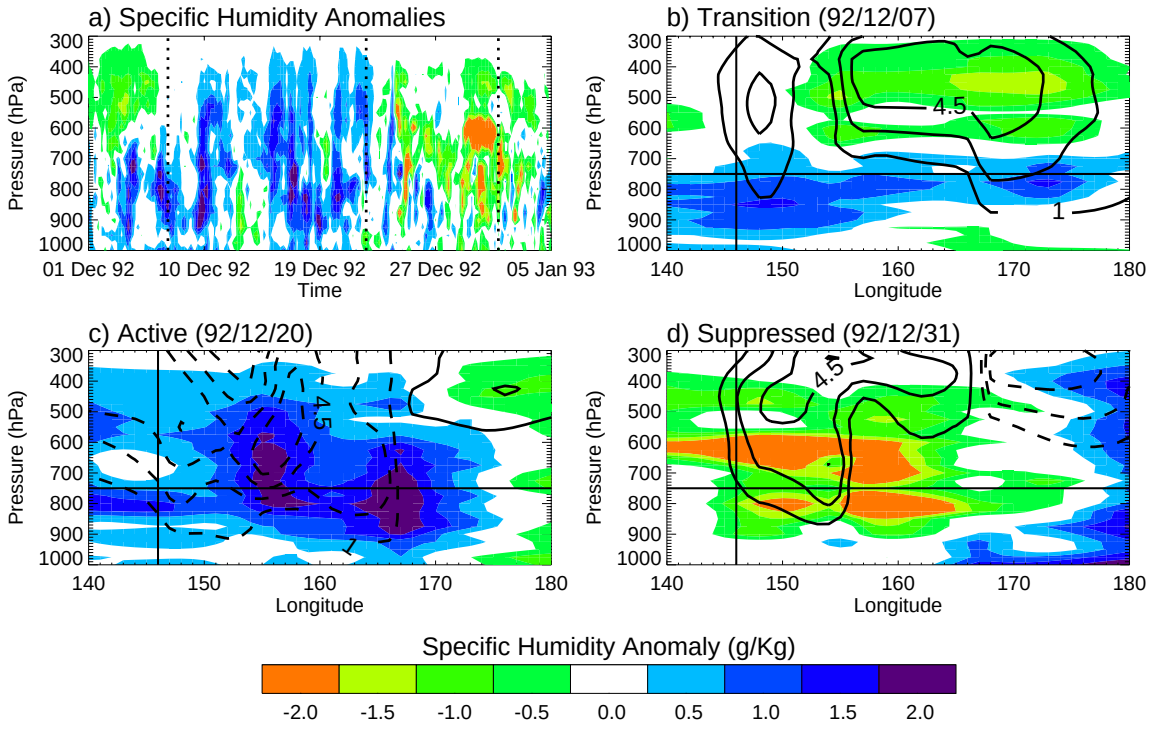

Figure 14: a) Vertical distribution of specific humidity anomalies over 0°, 146°E during the IOP. Anomalies are computed for each level relative to the IOP mean value. b) to d) Specific humidity anomalies along the equator from 140°E to 180° for transition, active and suppressed conditions (Vertical dotted lines in panel a). Black contours represent vertical velocity (hPahr-1). Solid contours indicate air subsidence and dashed contours indicate convection.

to an increase of atmospheric stability and a correspondent decrease of CAPE. Figure 16 shows the build-up of CAPE during the suppressed period and the first half of the unstable transition stage and the rapid reduction of CAPE during the convective phase of the ISO. During the transition, deep convection is inhibited by subsidence. This phenomenon favors the organization of large-scale low level moistening, preconditioning the atmosphere for the following deep convective event.

So far, the presence of the moistening of the atmosphere preceding the occurrence of two active events of the ISO during IOP period has been shown. This raises an interesting question: is the low-level moistening a robust feature of most ISO events? In order to answer this question the fist step was to analyze data collected during the

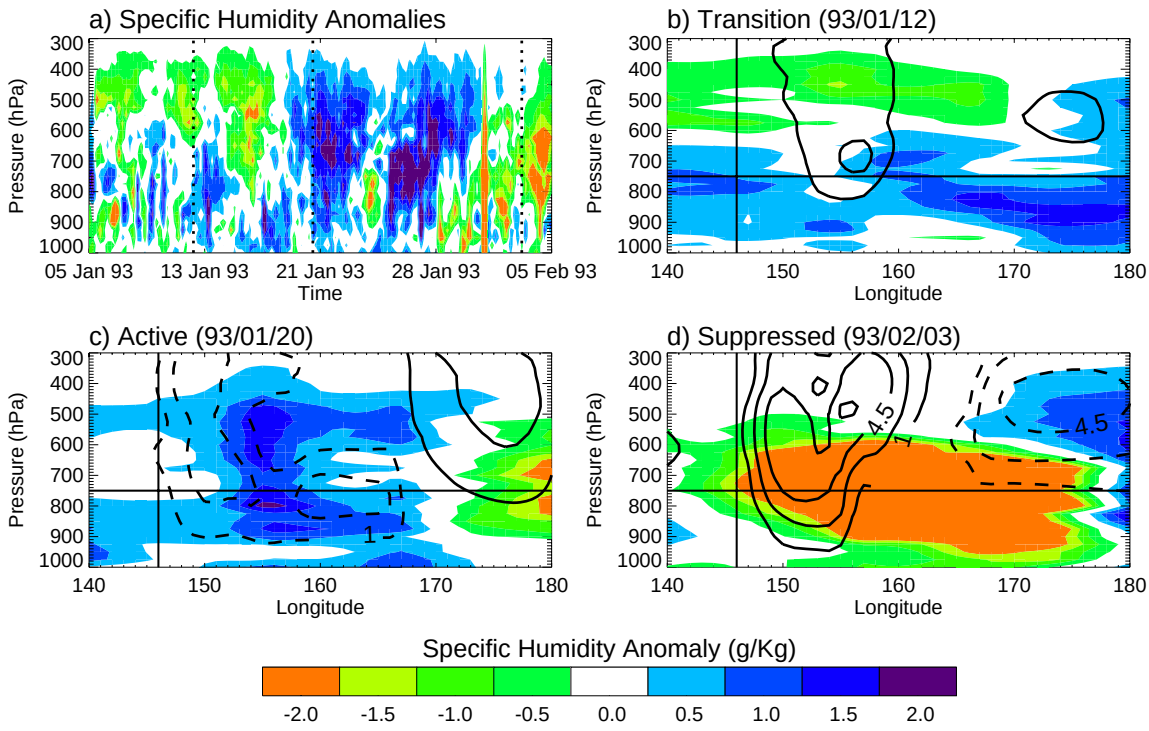

Figure 15: Same as Figure 14 but for the second ISO during the IOP.

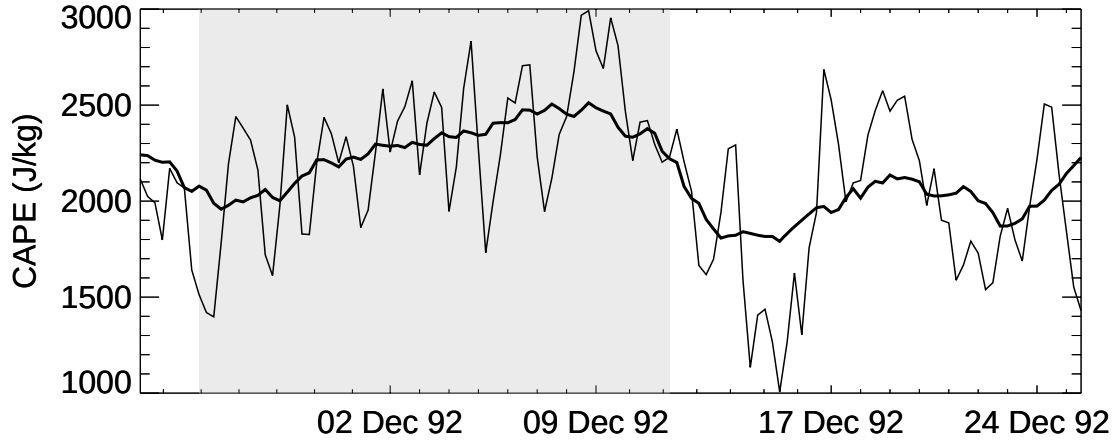

Figure 16: 12-hour CAPE estimates from soundings over the IFA for the first transition period during the IOP. The shadowed area highlights the slow building up of CAPE during the suppressed and transition phases of the first ISO during the IOP.

Joint Air-Sea Monsoon INteraction Experiment (JASMINE) which took place in the summer of 1999 and recorded an intraseasonal event that resemble the behavior of the

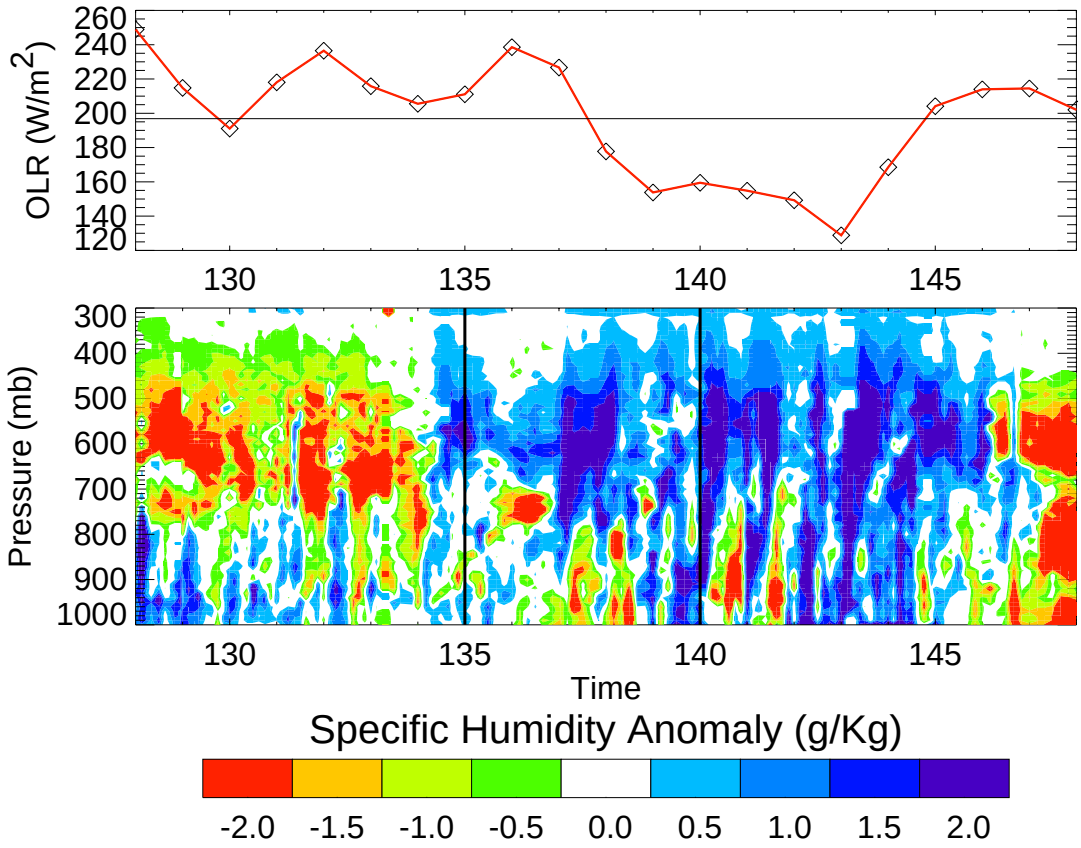

Figure 17: Time series of OLR in the Bay of Bengal (top) and Anomalies of specific humidity in the troposphere (bottom) from data collected during the Joint Air-Sea Monsoon interaction Experiment (JASMINE) in the summer of 1999.

mean ISO in the region (Webster et al. 2002). Figure 17 presents the time series of OLR in the Bay of Bengal showing the transition from suppressed to active convection as well as the anomalies of specific humidity in the troposphere. A similar low level moistening prior to the deep convection as the one observed during TOGA COARE IOP occurs. The second step was to perform a composite analysis of intraseasonal anomalies of specific humidity. 38 Winter ISO events selected based on a relevant index of ISO activity by Hoyos (2006) were used. This composite technique allows analysis of the most salient features of the evolution of the average ISO activity

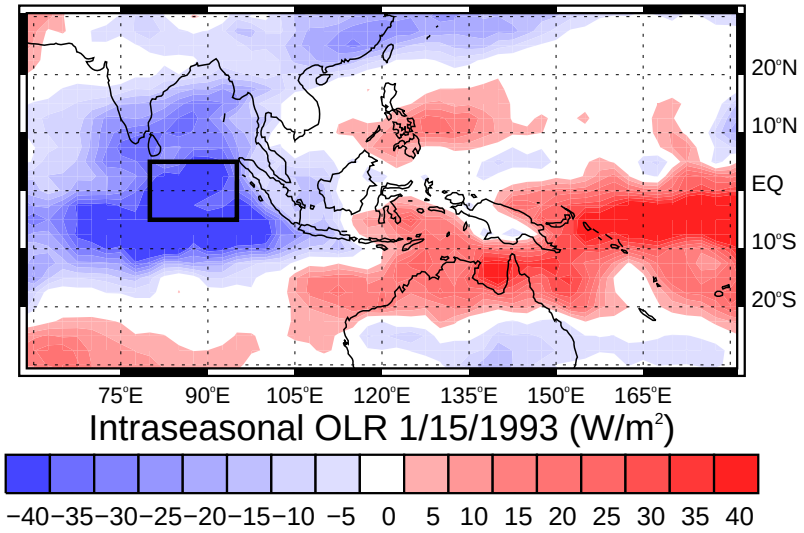

Figure 18: Day 0 of the composite analysis based on the 38 winter ISO events corresponds to the maximum of convection over the central Indian Ocean (outlined region).

including the low moistening, if present in the long term mean and in an extended region.

In this composite analysis Day 0 corresponds to the start of the convective event over the central Indian Ocean (region shown in Figure 18). Once the dates of the ISO winter events are established, an analysis of the evolution of the specific humidity field from the NCEP-NCAR reanalysis from 10°S to 10°N and along the equator is performed. Figure 19 clearly shows how the large-scale low-level moistening starts to develop to the east of the maximum convection at Day 0. As the moistening increases and the atmosphere is preconditioned, the convection center moves and the low level moistening continue to developed towards the east of the convection anomaly during the following days. At the same time, the convective anomaly is replaced by a dry anomaly that eventually penetrates the whole column.

It is possible to evaluate the temporal evolution of the selected events if an average from day -10 to 20 is computed for the entire warm pool region. Figure 20 shows the

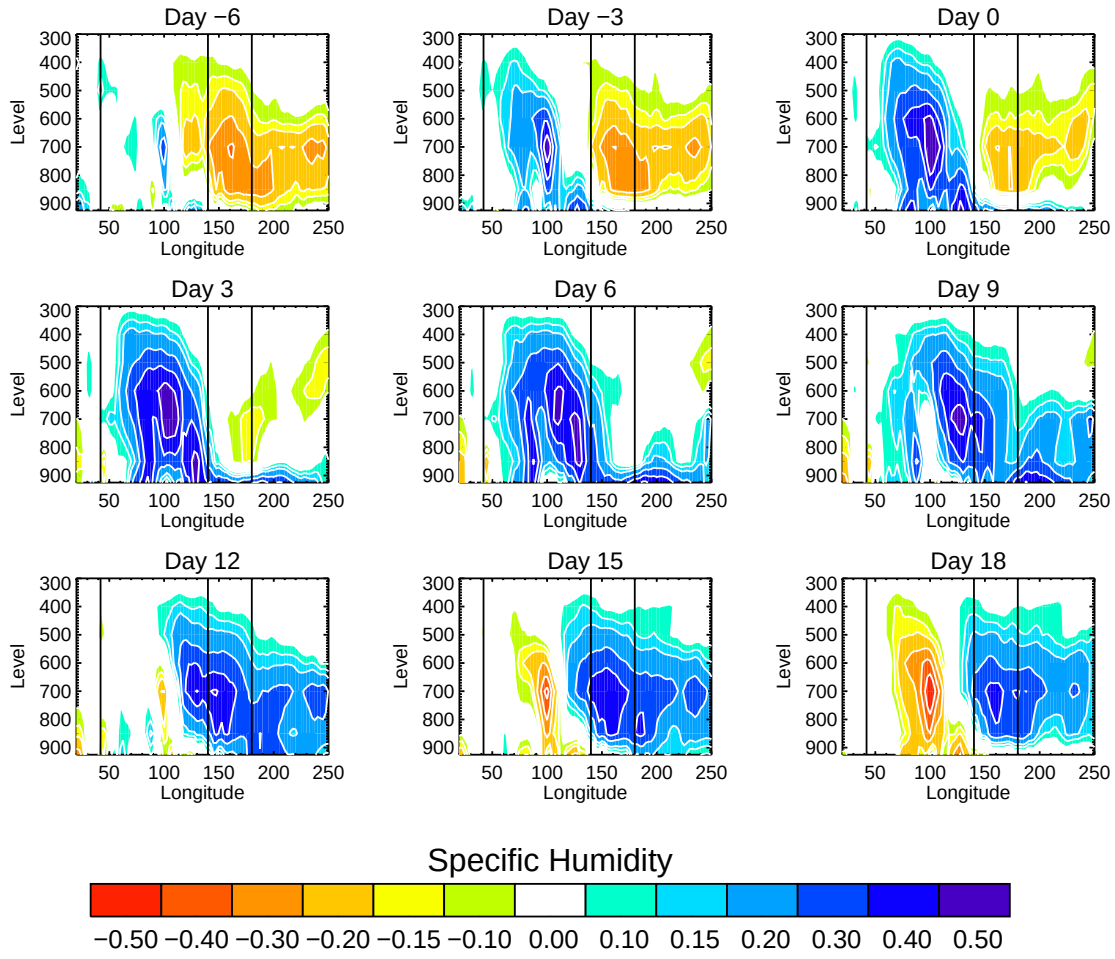

Figure 19: Evolution of the specific humidity field for 38 winter ISO events from the NCEP-NCAR reanalysis from 10°S to 10°N and along the equator.

composite temporal evolution for the 38 winter ISO events. The low level moistening is present from day 0 with moistening gradually extending to the upper troposphere prior to the deep convective event during the following days. During summer (31 events) the same behavior of the humidity is observed (Figure 21). Both specific humidity composites indicate that the low level moistening is a robust feature that is important for the development of ISO events in both seasons.

Atmospheric subsidence, as mentioned previously, appears as a key factor during the transition as it inhibits deep moistening of the atmosphere. In the composite structure of ISO, the subsidence also appears as an important feature: Figure 22

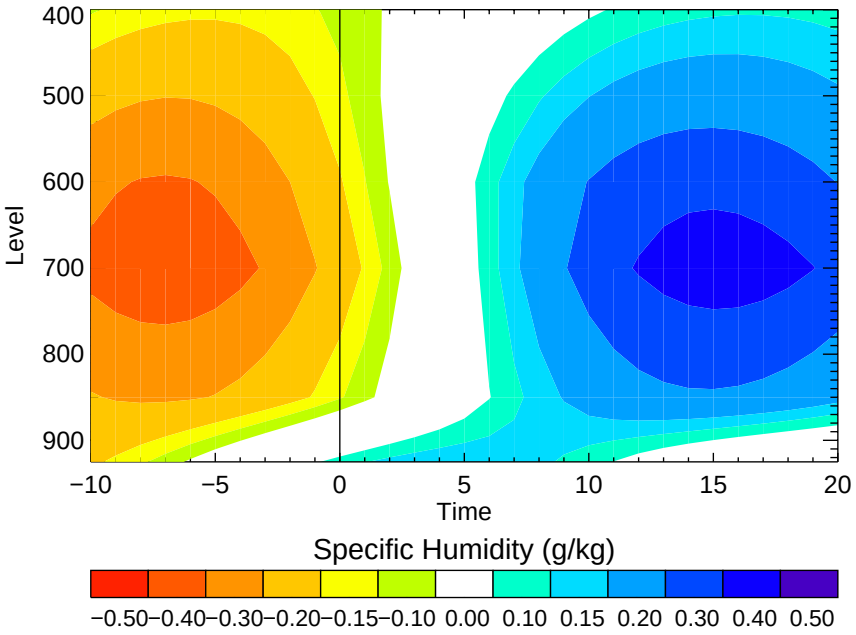

Figure 20: Temporal evolution of the average from day -10 to 20 over the entire warm pool region for the 38 winter ISO events.

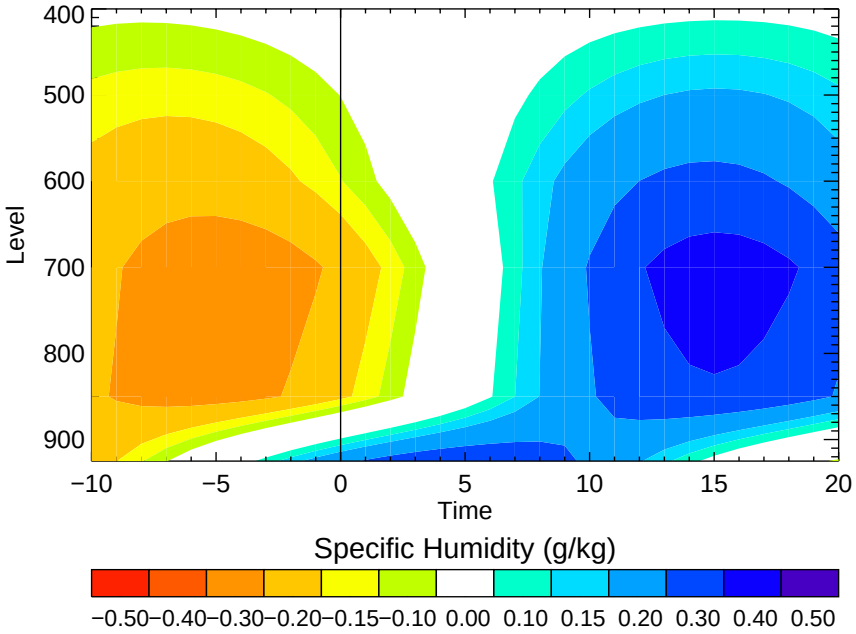

Figure 21: Same as Figure 19 but for 31 summer events.

shows the zonal mass stream functions computed for the 38 winter ISO events. At Day 0, intraseasonal anomalous subsidence over the warm pool, which corresponds

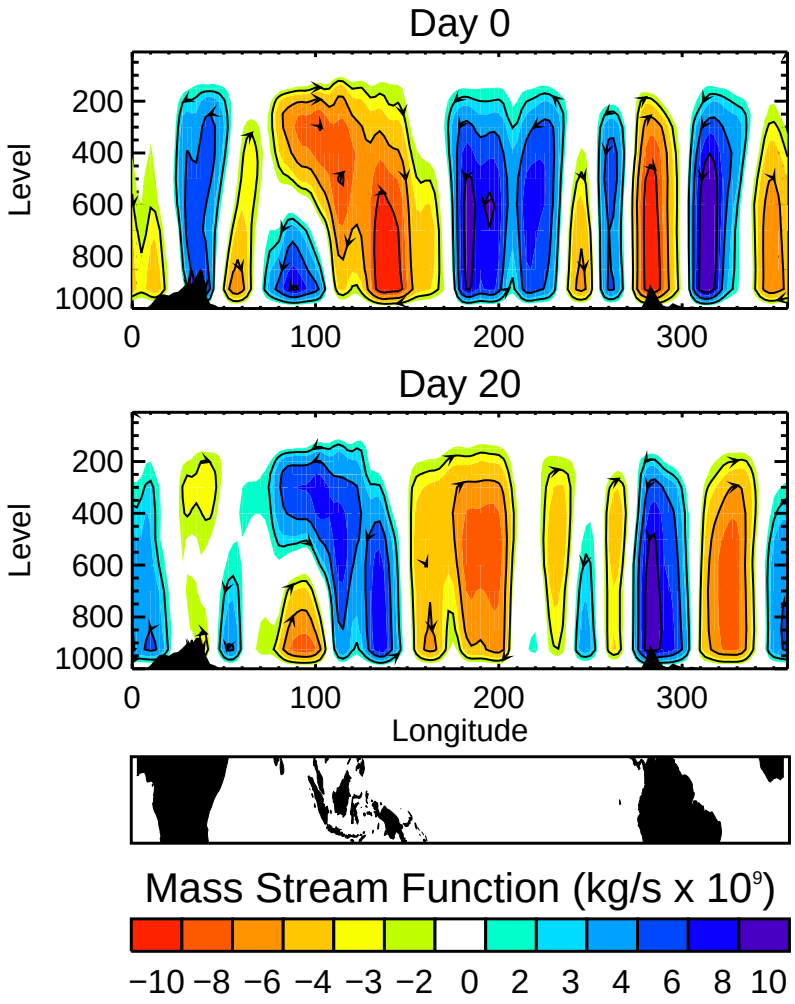

Figure 22: Zonal mass stream function calculated for the 38 winter ISO events and using NCEP-NCAR Reanalysis winds following the definitions in Peixoto and Oort (1992) and Hartmann (1994).

to the descending branch of the anomalous circulation set by the convective event in the Indian Ocean, traps the moistening on the lower levels. The mass stream functions were estimated using NCEP-NCAR Reanalysis winds following the definitions in Peixoto and Oort (1992) and Hartmann (1994).

In general, moistening of the atmosphere leads to cloud formation. Figure 23 shows time series of the population of cloud-free pixels, midtop nonprecipitating clouds, and the total of high-top precipitating clouds during both transition phases during TOGA COARE IOP. The reduction of cloud-free pixels is evident in both transition stages,

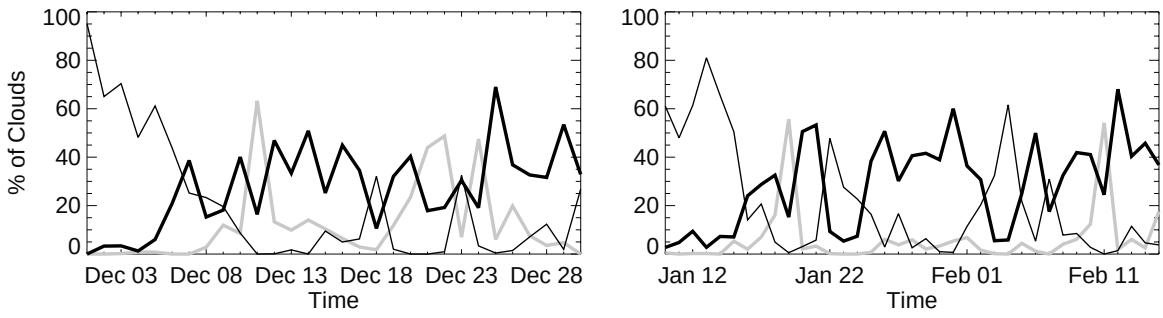

Figure 23: Percentage of cloud-free pixels (black thin line), midtop nonprecipitating clouds (black thin line), and total high-top precipitating clouds (grey line) for both transition periods during the ISO.

as well as the slow increase in midtop nonprecipitating clouds (Table 2). Lin and Johnson (1996) speculated that the low-level moistening may be a consequence of vigorous boundary-layer mixing and shallow nonprecipitating cumulus clouds during these high-wind periods. In contrast, our results (Figure 23) indicate that warm (shallow) nonprecipitating clouds tend to be present at all times, and their variability is not associated, at least directly, with the ISO. Due to the behavior of midtop nonprecipitating clouds, it is fair to conclude that only midtop nonprecipitating clouds appear as a direct result of the low-level moistening of the atmosphere. In a later paper, Johnson and Lin (1997) found that the shallow cumulus regimes are not only prominent during the westerly wind bursts but also during suppressed light-wind periods. The later results of Johnson and Lin (1997) appear to be consistent with the results presented in this study. On the other hand, the rapid increase of mid-top non-precipitating clouds between the suppressed (12%), transitional (28%) and convective phases (35%) indicate a close association with the ISO.

ISO events modify not only the atmospheric structure but also the oceanic mixed layer. Data measured on board the R/V Kexue #1 and the IMET buoy provides a good description of the oceanic mixed layer variability. R/V Kexue #1 was located at 4°S to 156°E and was anchored on station for three different periods: November 10 to December 12 1992, December 19 1992 to January 23 1993 and February 1 to February

20 1992. Conductivity-temperature-depth (CTD) measurements show a slow warming of the surface layers of the ocean associated with the weak surface winds and lack of cloud cover, evident during early December 1992. Maximum temperatures occur during the transition, before low-level winds are intense enough to induce evaporative cooling and mixing (Figure 24a). During late December 1992, the ocean rapidly cools in response to increasing cloud cover and stronger low-level winds. Cooling is also present below 50 m, associated with upwelling of cold water. Salinity changes near the surface are principally induced by precipitation and upwelling of saltier water (Figure 24b). During the transition phase, enhanced evaporation introduced a slight increase in near-surface salinity. The magnitude of such an increment (+0.05 PSU) is smaller compared to the freshening resulting from precipitation (-0.18 PSU) during the disturbed period. During the suppressed phase, the upper 100 m of the ocean has strong negative temperature anomalies and positive salinity anomalies.

In summary, it has been shown here that processes associated with the life cycle of an ISO event are complex and involve both the ocean and the atmosphere. The associated convective activity can be separated into different phases: suppressed, transition and convective phases. There is a well-defined transition stage between suppressed and deep convection, where low-level winds become stronger, low-level moistening and CAPE build-up, formation of midtop nonprecipitating clouds takes place, and warmer SSTs favored by clear skies and weak low-level winds are present. During the transition, deep convection is inhibited by subsidence. This phenomenon favors the organization of large-scale low level moistening, preconditioning the atmosphere for the following deep convection event.

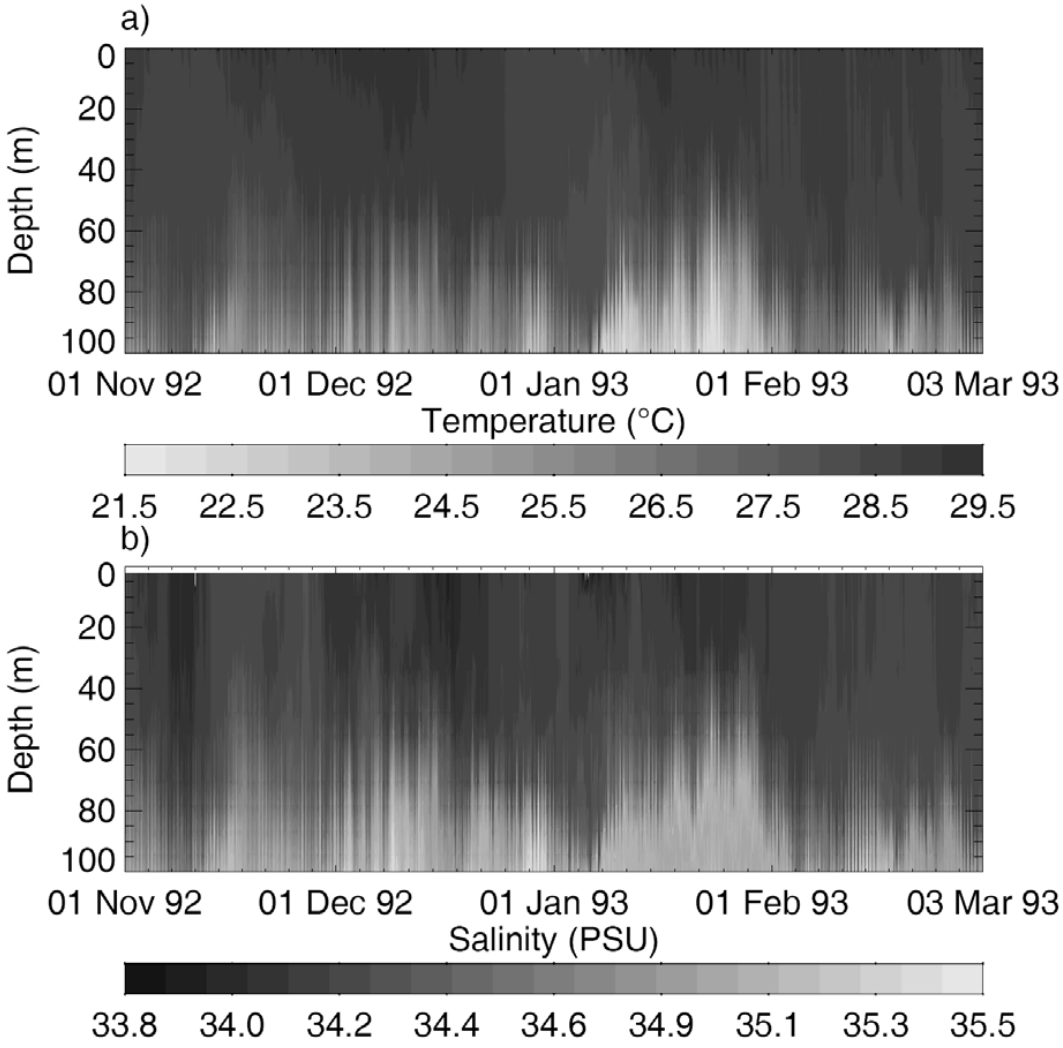

Figure 24: Evolution of subsurface temperature at IMET buoy, and b) Same as a) but for salinity

CHAPTER III

NUMERICAL MODELING OF THE INTRASEASONAL VARIABILITY

As mentioned in Chapter 1, many attempts to simulate and forecast the ISO using numerical models have met with difficulties reproducing it or obtaining realistic propagation speed in the case of the MJO. In this section we use the results of the analysis presented in Chapter 2 in the framework of a numerical experiment to improve our understanding of the problems that numerical models have in simulating and forecasting the ISO. In particular, the main goal of this chapter is to evaluate the skill of a numerical model in simulating the processes that occur during the transition from suppressed to active convection which we consider, based on the data analysis presented in Chapter 2, as key for skillful extended forecasts in the Indo-West Pacific region. In the analysis, we evaluate the regional and local vertical structure of ISO-related anomalies from the numerical forecasts compared to those in ERA-40 data in different stages of the convective activity (suppressed, transition, and active). The ISO exhibits a rich vertical structure, with low-level moisture convergence and upper tropospheric divergence anomalies that lead to moistening of the boundary layer and the development of shallow convection followed by a gradual and then more rapid lofting of moisture into the middle troposphere at the onset of deep convection. However, previous studies on the simulation and forecasting skill of the ISO have been restricted to the analysis of 2-dimensional fields in the horizontal plane (e.g. Slingo et al 1996, Lin et at 2005). The evaluation of the vertical structure will advance our understanding of why climate and forecast models tend to fail in simulating the ISO.

The MJO/ISO has a marked seasonality evident in the differences in amplitude,

frequency, and propagation features between boreal summer and winter (e.g. Zhang 2005). However, as shown in Chapter 2, the low level moistening during the transition phase is a robust feature of the local ISO during both seasons. For this reason, this analysis explore ISO numerical simulations during the TOGA COARE case, which took place during winter, as well of important ISO events during the summers of 2002 and 2004. This is important because most studies only address the predictability and prediction of the winter ISO.

The numerical experiments are part of a series of extended forecasting simulations conducted jointly between GeorgiaTech and the ECMWF and organized by Dr. Peter Webster. The experiments emerged as a major recommendation from the ECMWF/CLIVAR Intraseasonal Variability Workshop (http://www.ecmwf.int/newsevents/meetings/workshops/2003/Intra-seasonal_variability/) to evaluate the ability of the ECMWF model to reproduce the observations in different phases of the ISO for well documented events. As part of the experiment, a series of 30-day forecasting integrations (extended forecasts runs) were completed for selected ISO cases both during boreal summer and winter, starting every day during the duration of the lifecycle of each of the identified events ($\sim$20 days before and after the maximum convection in the West Pacific Warm Pool or Central Indian Ocean depending on the case). The forecast integrations include a control forecast and four ensemble members. This experiment constitutes a unique dataset to study the evolution of forecast skill relative to different phases of the ISO. The serial integrations experiment allows discerning why, where and when the ECMWF model loses skill forecasting intraseasonal activity. Using an operational forecast model to evaluate the dependence of the forecast skill on the convective phase, rather than following the more traditional climate model approach, allows a direct comparison of the forecast with an observed event, rather than climate ISO statistics typically used to assess ISO simulations (e.g. Slingo et al. 1996, Lin et al. 2005), providing a better assessment of the skill of the model.

We analyze experimental model forecasts using the fully-coupled European Centre for Medium-Range Weather Forecasts (ECMWF) model from the monthly forecasting framework (Vitart 2004). The atmospheric component of the coupled model is the ECMWF atmospheric model Integrated Forecast System (IFS). The model used in this study has a resolution about 1.9 x 1.9 degrees (TL95) with 40 levels in the vertical. The oceanic component is the Hamburg Ocean Primitive Equation (HOPE) from the Max Plank institute and it has a zonal resolution of 1.4 degrees and 29 vertical levels (Wolff et al. 1997). The coupling of the components is through the interface Ocean Atmosphere Sea Ice Soil (OASIS) platform developed at the *Centre Europen de Recherche et Formation Avance en Calcul Scientifique* (CERFACS; Terray et al. 1995). Initial conditions for the atmospheric and land surface were obtained from the ECMWF operational atmospheric analysis/reanalysis system (ERA40; Simmons and Gibson, 2000). The ECMWF oceanic data assimilation system used to produce the initial conditions of the ECMWF seasonal forecasting system was used to generate initial conditions for the oceanic component.

3.1 Analysis of the TOGA-COARE Case

Since ERA-40 data was used as the source for initial conditions of the atmosphere in the numerical experiment, it is essential to determine weather or not this product reasonably represents the different stages of convection and, in particular, the low-level moistening seen in the soundings. Figure 25 and Figure 26 show a summary of the first TOGA-COARE ISO as represented by ERA-40. In Figure 25, the vertical structure around the equator (4°S-4°N) of the 5-day moving average specific humidity, temperature and wind speed anomalies relative to the mean during the TOGA-COARE period is shown for three different dates during suppressed (11/26/1992), transition (12/9/1992), and active (12/26/1992) conditions over the warm pool. Figure 25

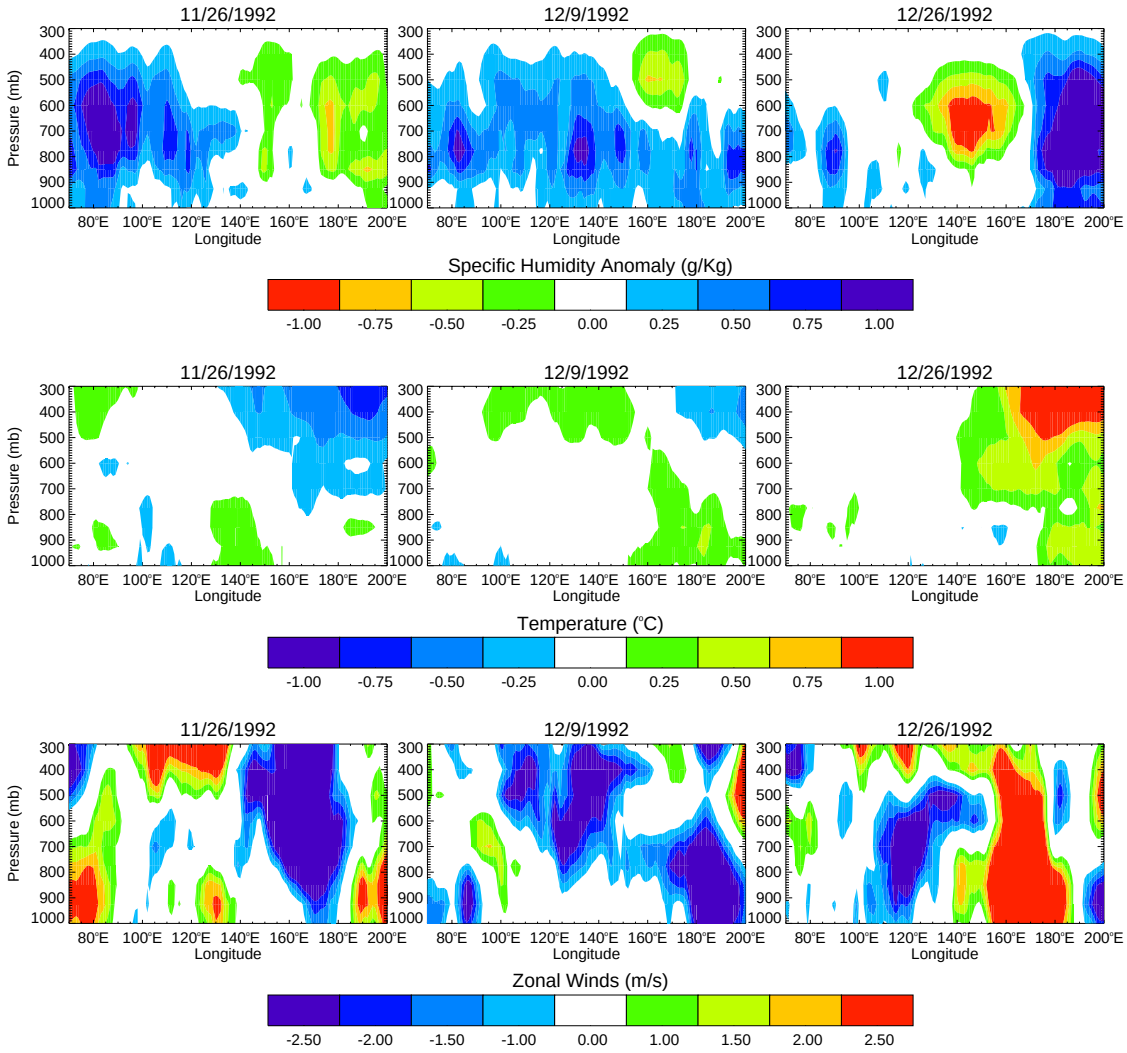

Figure 25: Vertical structure around the equator (4°S-4°N) and over the Indian Ocean-West Pacific Warm Pool of the 5-day moving average specific humidity (top), temperature (middle) and wind speed (bottom) anomalies relative to the mean during the TOGA-COARE period for three different conditions: suppressed (11/26/1992), transition (12/9/1992), and active (12/26/1992).

clearly shows the negative (positive) humidity anomalies during the suppressed (active) phase over the warm pool together with anomalies with different sign over the Indian Ocean. The regional low-level moistening over the warm pool is also evident in the ERA-40 data during the transition phase, when convection over the Indian Ocean is slowing down. ISO-related changes in wind speed and temperature in the atmosphere in ERA-40 are also consistent with those found in the data, with a warming

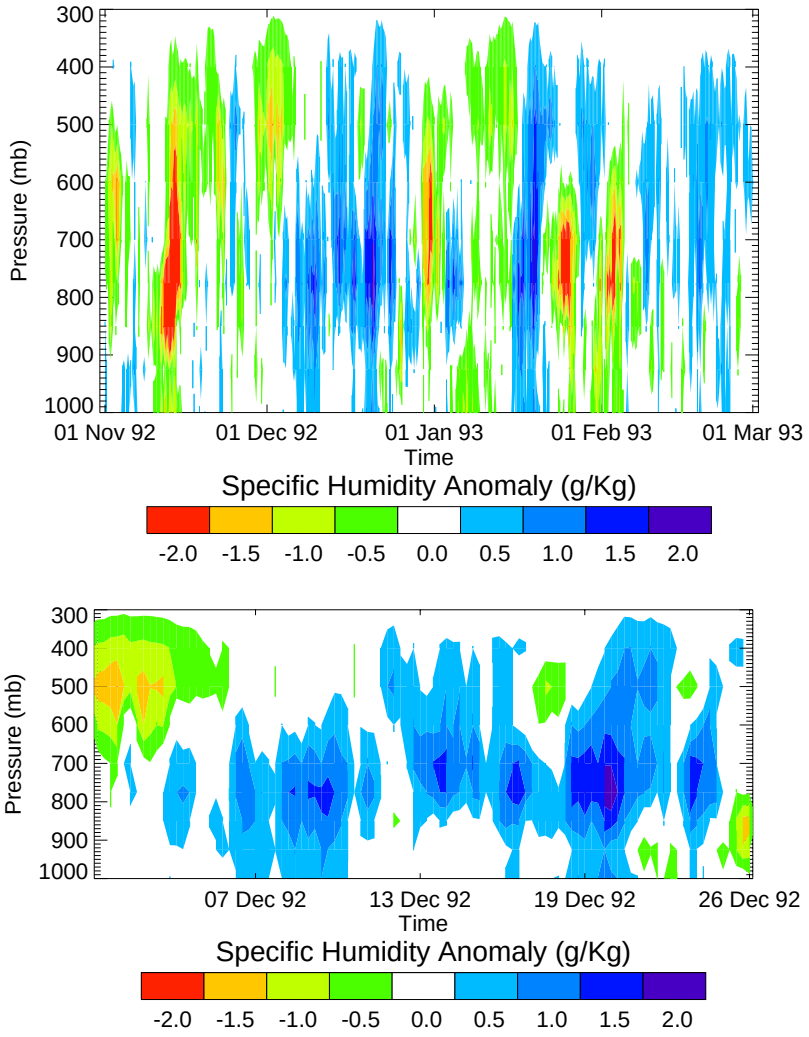

Figure 26: Time-pressure diagram of specific humidity anomalies over IFA from ERA-40 computed for each level relative to the mean value during the IOP (top) and detail of the first transition period (bottom).

of the atmosphere and reversal of the winds during the transition and active phases. Figure 26 shows the evolution of the moistening over IFA from ERA-40 (similar to Figure 4a) and a detail of the transition during the first ISO event (similar Figure 12a). The humidity profiles, even with the lower resolution in ERA-40, are similar to those obtained with the IFA soundings during TOGA COARE IOP. Even the magnitude and variability of the latent heat flux in ERA-40 compares well, considering the resolution, with observations from the IMET buoy (see Figure 27).

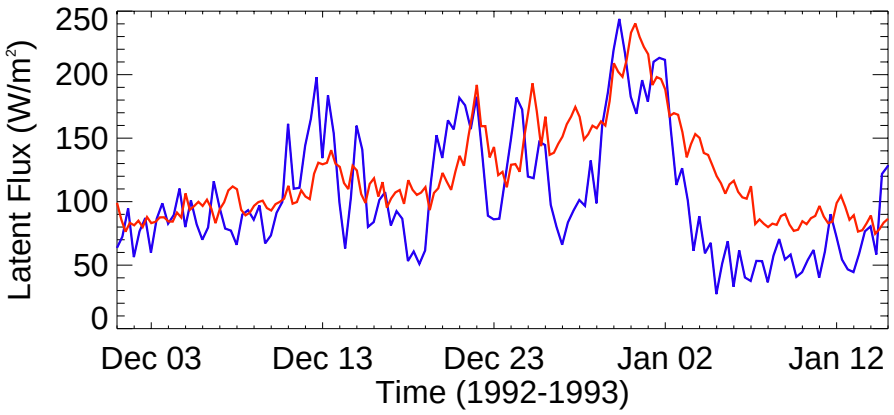

Figure 27: Time series of 8-hourly latent heat flux for the first ISO event during the IOP for data collected by the IMET buoy (black) and for ERA40 (red).

3.1.1 Forecast Skill of the Regional Vertical Structure of ISO-related Circulation Anomalies

To evaluate the skill of the ECMWF coupled model in forecasting the vertical structure of the ISO/MJO, in this section we concentrate on the analysis of the zonal vertical structure of the ISO event around the equator and in the Indo-West Pacific region. Anomalies of zonal winds and specific humidity were selected as the variables most representative of the vertical structure of the ISO since both summarize the zonal circulation and convective anomalies that occur during an ISO event. To study the forecast skill of the tropospheric vertical structure associated with the ISO in the Indo-West Pacific region we analyzed the pattern correlation and the standardized pattern root-mean-squared (RMS) error of 5-day moving average anomalies of temporal snapshots of longitude-height diagrams of latitudinally averaged zonal winds and specific humidity in the 10°S-10°N latitude band relative to the mean during the TOGA COARE IOP. The magnitudes of both the correlations and RMS between model forecasts and ERA-40 data are estimated. The longitudes considered are between 60°E and 170°W and the heights from 1000 to 100hPa. Since we want to concentrate on the skill of the extended forecast which is related to the relatively low-frequency envelope of ISO-related convection, the objective of using the 5-day

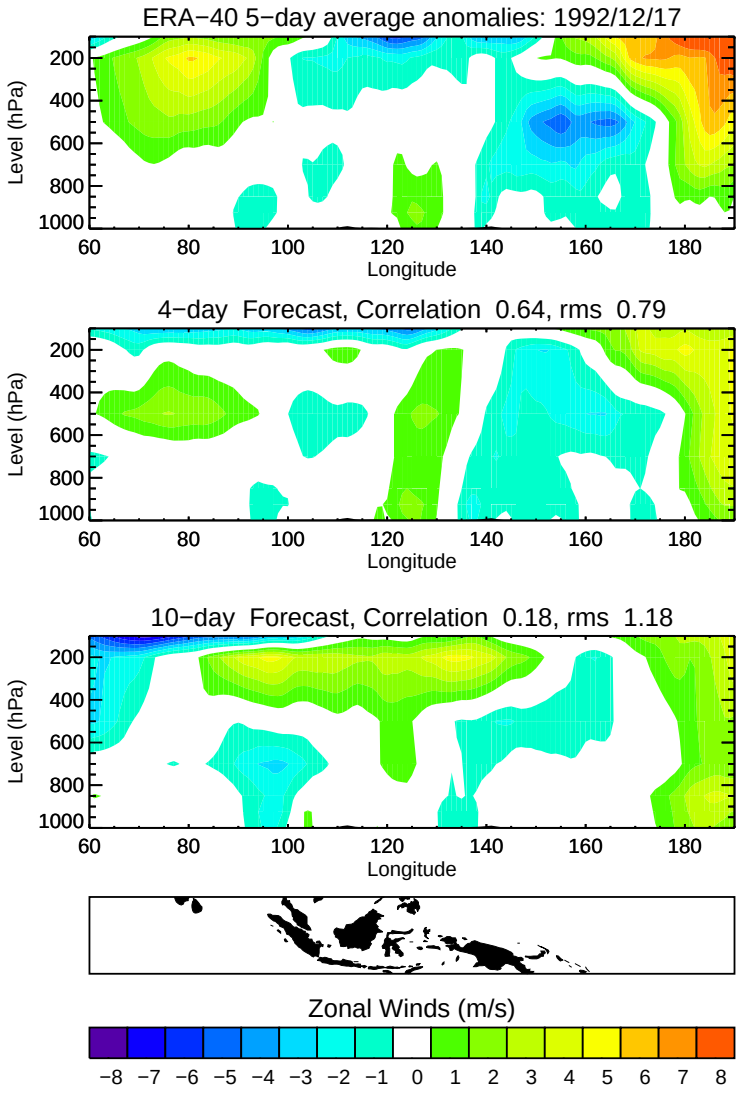

Figure 28: 5-day averaged anomalies of zonal winds around December 17 1999 for ERA-40 (top), 4-day control forecast starting December 13 (middle), and 10-day control forecast starting December 7 (bottom).

moving average is to filter out high-frequency variability that could potentially mask the skill of the extended forecast. This is done because the reasonable goal of numerical models is to be able to forecast the long-lived envelope of convection but not necessarily the rapidly changing structure within.

Figure 28 shows a representative example of the analysis for 5-day averaged

anomalies of zonal winds around December 17 1999. The top panel shows the ERA-40 anomalies and the middle and bottom panels show the 4-day control forecast (i.e. starting December 13) and the 10-day control forecast (i.e. starting December 7) of the 5-day averaged anomalies around December 17, respectively. The pattern correlation and standardized RMS were estimated between the ERA-40 data and both forecasts. The standardized RMS is estimated as the mean square root of the squared differences between ERA-40 and forecast divided by the standard deviation of the ERA-40. When the standardized RMS is greater than 1, the error in the forecast is greater than the variability of the data. Both values, which are reported in each panel of Figure 28, provide information about the skill of the forecasts. As expected, the 10-day forecast for December 17 1999 (Correlation: 0.18, RMS: 1.18) is less skillful (lower correlation and higher RMS) than the 4-day forecast (Correlation: 0.64, RMS: 0.79). In both cases, however, the amplitude of the forecasted 5-day averaged anomalies is considerably lower than in the ERA-40. A similar diagram as the one in Figure 28 is presented in Figure 29 for specific humidity. The skill of the zonal wind and the specific humidity forecasts for the same lead time is considerably different, being lower the one for specific humidity. While the 4-day forecast specific humidity pattern seems to correlate well with observations (0.66), the standardized RMS is already higher than 1 (1.10) for this short lead time. The diagrams indicate that the model forecasts a drier atmosphere compared to ERA-40. This is particularly clear in the 10-day forecasts (0.25, 1.37), where most of the domain shows negative specific humidity anomalies.

The previous case was presented as an example of the estimation of forecast skill for a single date and for two different forecast lead times. From the serial experiment we have forecasts ranging from 1-day to 30-day lead times, starting from 62 different consecutive days (from December 1 1992 to January 31 1993), allowing us to study the behavior of the forecast skill relative to the initial conditions and for different forecast

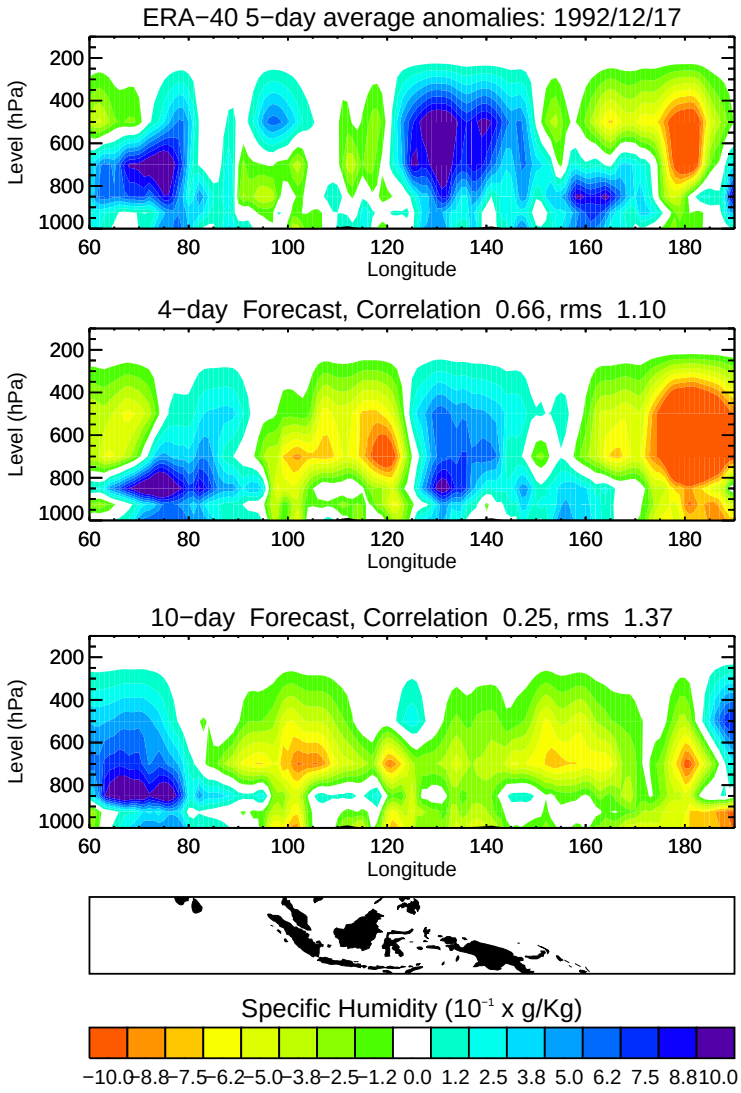

Figure 29: Same as Figure 28 but for specific humidity.

lead times. Figure 30 and Figure 31 show a forecast lead time - start of the forecast diagram of correlation and standardized RMS for zonal winds and specific humidity, respectively. The figures also show the average correlation and RMS for each forecast lead time. The common feature between both figures is the high variability in the forecast skill (both in correlation and RMS) with different initial conditions (start of the forecasts). In other words, the skill of the model strongly depends on the region of the complex non-linear attractor of the system where the state of the atmosphere

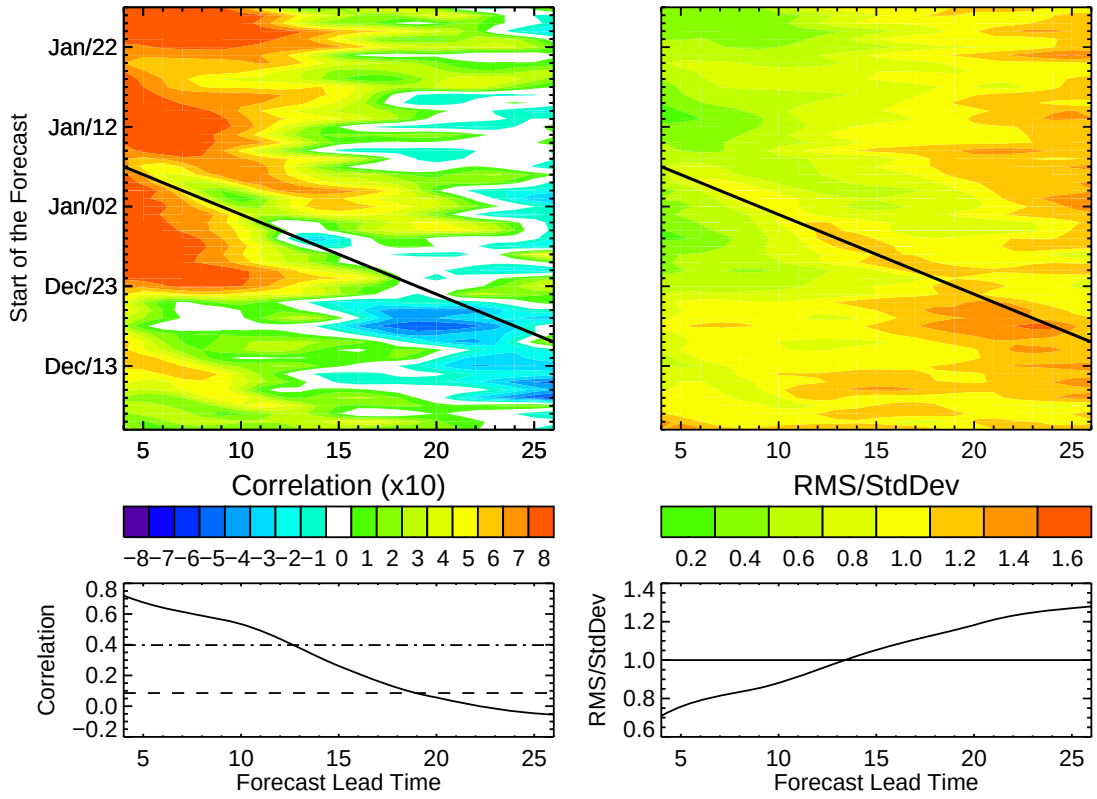

Figure 30: Distribution of the correlation (top-left) and standardized RMS (top-right) as a function of forecast lead time and start of the forecast for vertical anomalies of zonal winds in the Indo-West Pacific region for the TOGA-COARE case. Black line corresponds to the forecast of January 11 1993 from different lead times. Average correlation (bottom-left) and RMS (bottom-right) for each forecast lead time are also shown.

is at the beginning of each run. In addition, the diagonal patterns observed in Figure 30 and Figure 31, which are always around a specific date, indicate that there are states of the system for which the skill of the forecast is always low. Those states coincide with convective events. As an example, the diagonal black lines in Figure 30 and Figure 31 correspond to the forecast of January 11 1993 from different lead times. This line is associated with low values of correlation and high values of RMS in both zonal winds and specific humidity, suggesting that irrespective of the start of the forecast the regional skill of the model is low when trying to forecast around January 11 1993. The conditions around this particular date are of a transitional and active

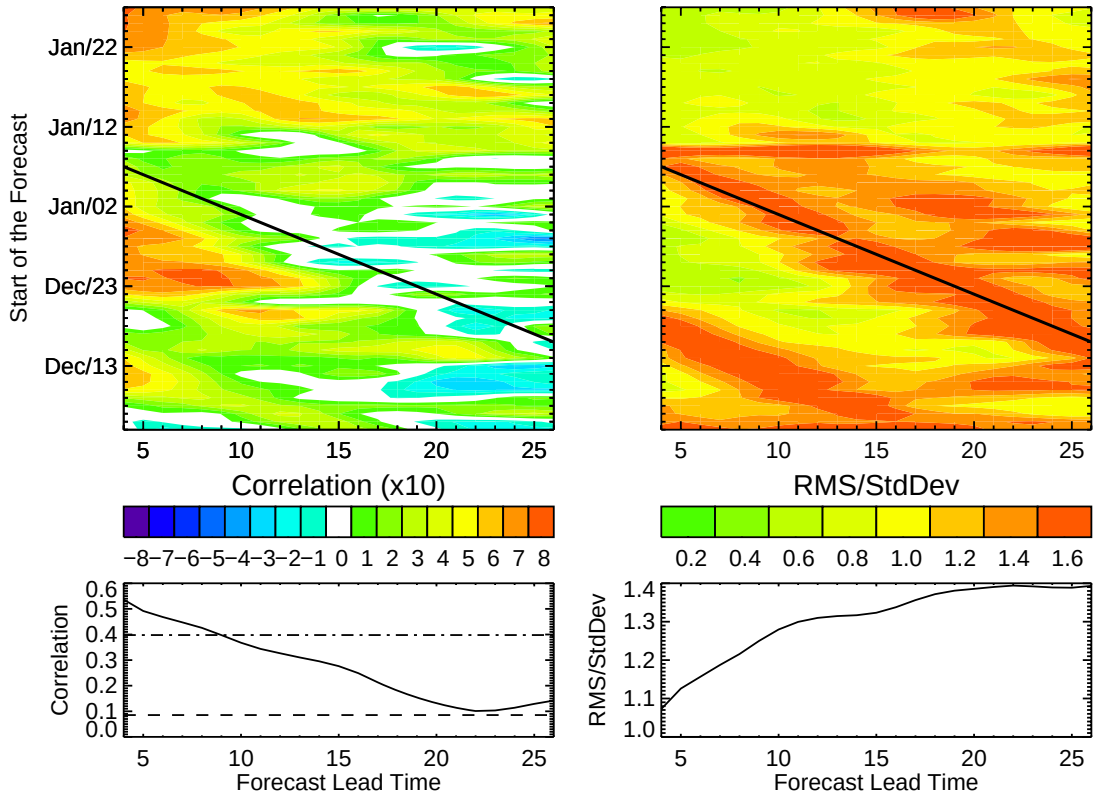

Figure 31: Same as Figure 30 but for specific humidity.

nature. Figure 32 shows the 10-day forecast of specific humidity for dates January 11 1993 to January 13 1993. ERA-40 anomalies (top) show the growth of the convective event from the Indian Ocean. In general, the three control forecasts (bottom) suggest a dryer atmosphere than ERA-40 data. As can be seen in Figure 32, the model forecasted a positive specific humidity anomaly in the right location (∼70°E) but not deep enough, missing the convective event. While there is low skill in the 10-day specific humidity forecast, in particular around convective events, zonal wind forecasts for 5-day average anomalies are still useful at the same lead time. Figure 33 shows the ERA-40 data and 10-day control forecasts of zonal winds and specific humidity for January 16 1993, which corresponds to a more mature convective stage of the event presented in Figure 32. In this case, the skill of the zonal wind forecast is relatively good (correlation 0.78, RMS 0.71). The pattern of the forecasted zonal

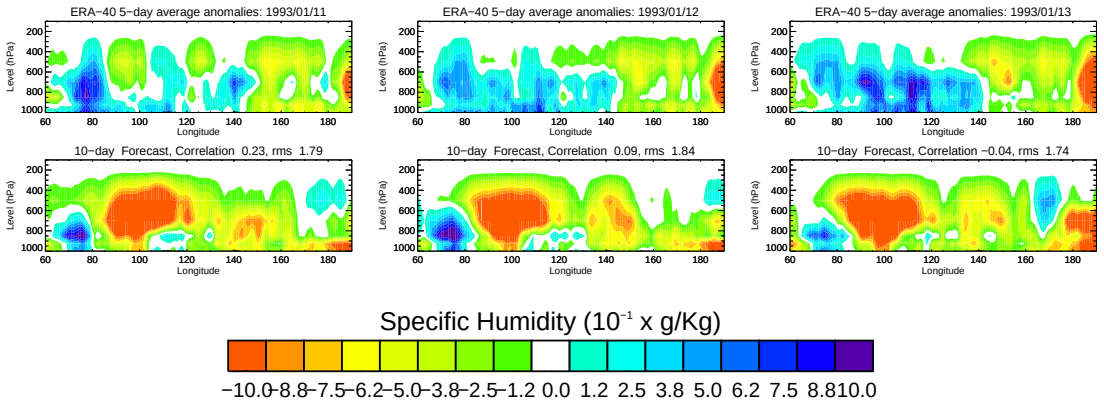

Figure 32: 10-day forecasts of specific humidity for dates January 11 1993 to January 13 1993. Anomalies from ERA-40 data (top) and model control forecasts (bottom) are shown.

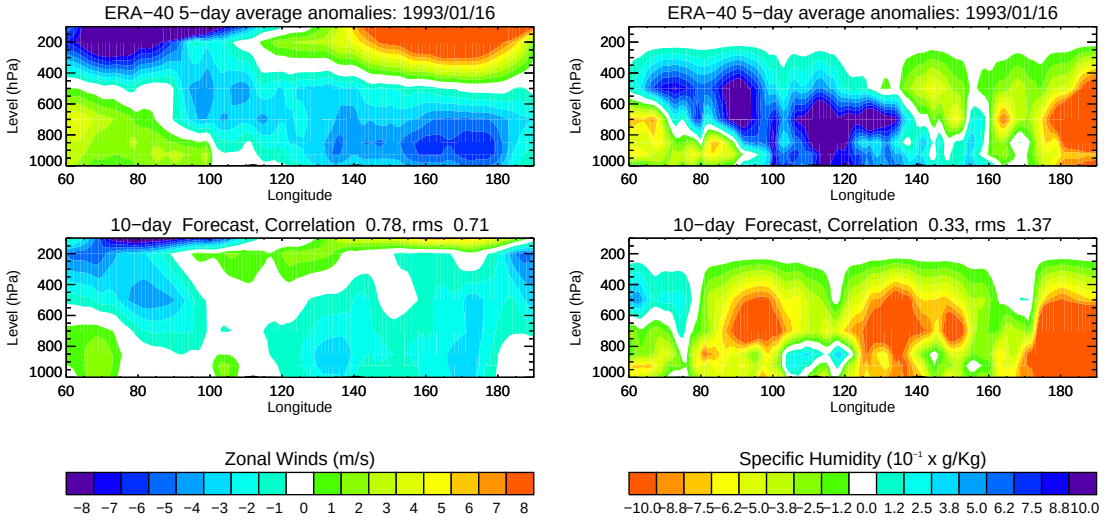

Figure 33: ERA-40 anomalies (top) and 10-day control forecast (bottom) of zonal winds (left) and specific humidity (right) for January 16 1993.

wind anomalies coincides well with ERA-40 in shape but not in magnitude (weak anomalies). On the other hand, there is no skill in the specific humidity forecast for the same date and lead time (correlation 0.33, RMS 1.37).

The features explained in the previous paragraph are present during the entire forecasting experiment during TOGA COARE. As can be seen in the bottom panels of Figure 30 and Figure 31, the overall forecast skill of the vertical structure of 5-day

average zonal wind anomalies is considerably higher than that for specific humidity anomalies. In both cases the average correlation (RMS) decreases (increases) with forecast lead, as expected. If we define skillful forecasts as those where the standardized RMS is less than 1 (i.e. where the error in the forecast is less that the variability in the vertical structure in the selected region), in general, the forecasts for 5-day average anomalies of zonal winds in the equatorial Indian Ocean-West Pacific region, which in this case correspond mainly to regional circulation anomalies associated with the ISO, are skillful up to about 13 days. Using the same skill definition, the forecasts of specific humidity, which is associated with the moist convective anomalies during the ISO, have no skill whatsoever. It is important to note that this is a rather conservative definition of skill since at the point where the standardized RMS is equal to 1, the forecasts are not good for practical applications. The overall zonal wind forecasts (specific humidity) correlation is below the 99% statistical significance threshold (dash-dotted line) after a forecast lead time of 13 (9) days. In general, analysis of the regional vertical structure of the forecasts indicate that the consequences of lack of skill are weak circulation anomalies produced by the model compared to those in ERA-40, and that the model tends to simulate a dryer atmosphere compared to the same data set. Both of these features are coherent since without the release of latent heating associated with deep convective events (positive anomalies of specific humidity) the circulation tends to be weaker and shallower. Figure 34 shows, in black, the temperature profile from 1000 to 500mb for a region in the Equatorial Indian Ocean (10°S-10°N; 70-90°E) for December 22 1992 from ERA-40 and, in colors, the forecasts for the same date from different lead times (5, 10, 15, 20 and 25 days). The left panel shows the absolute values and the right one shows the 5-day average anomalies. It is important to note that this figure summarizes the general behavior of the temperature profiles during the entire period of the experiment. The profiles show that the forecasts are about 1 degree cooler than ERA-40 near the surface and about 0.5

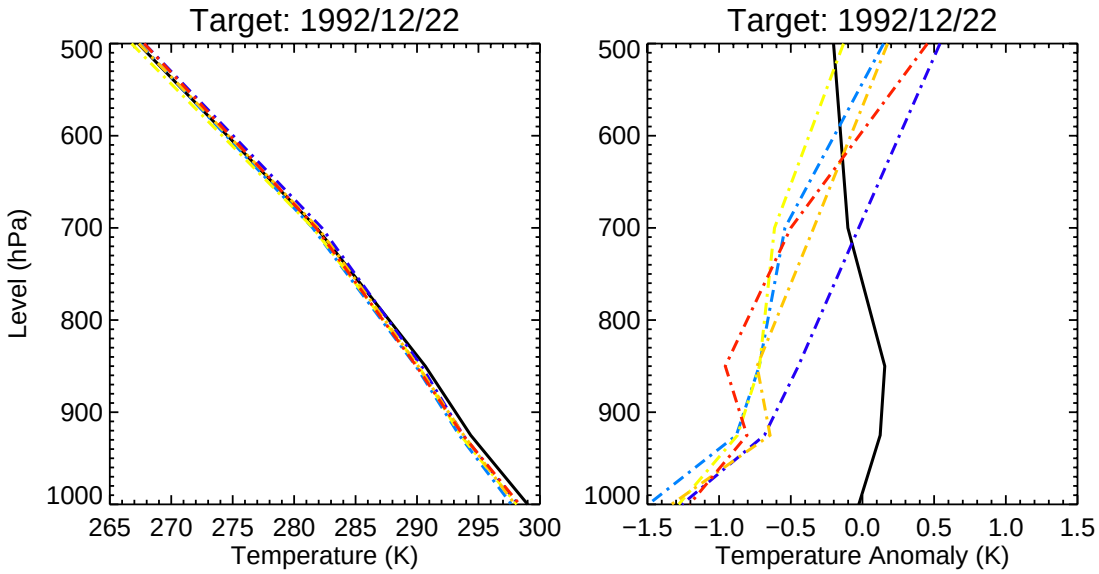

Figure 34: Temperature profile for a region in the Equatorial Indian Ocean (10°S-10°N; 70-90°E) for December 22 1992 from ERA-40 (black) and forecasts from different lead times 5, 10, 15, 20 and 25 days (from dark blue to red). Left panel shows the absolute values. Right panel corresponds to the 5-day average anomalies.

degree warmer around 500mb. This feature, together with the drier atmosphere in the forecasts result in a relatively more stable atmosphere compared to ERA-40 data, limiting the reproduction of deep convective events associated with the ISO.

The previous analysis was based exclusively on the control forecast. Analysis of the 4 ensemble members shows similar results. Figure 35 shows the vertical structure (from 1000 to 200mb) of 5-day average anomalies ERA-40 and 10-day forecasts of zonal winds for the same date as in Figure 33 (January 16 1993), including control forecasts and 4 ensemble members. All the ensembles show similar behavior with a reasonably good structure but weaker anomalies than in the ERA-40. The behavior of the correlation and standardized RMS is very similar for all ensemble members. Figure 36 shows both magnitudes for 10-day forecast lead time, for different starting dates. The black line corresponds to the control forecast and the color lines to each of the 4 ensemble members. While there is variability of the forecast skill among different ensemble members, the general behavior is similar, with low skill associated

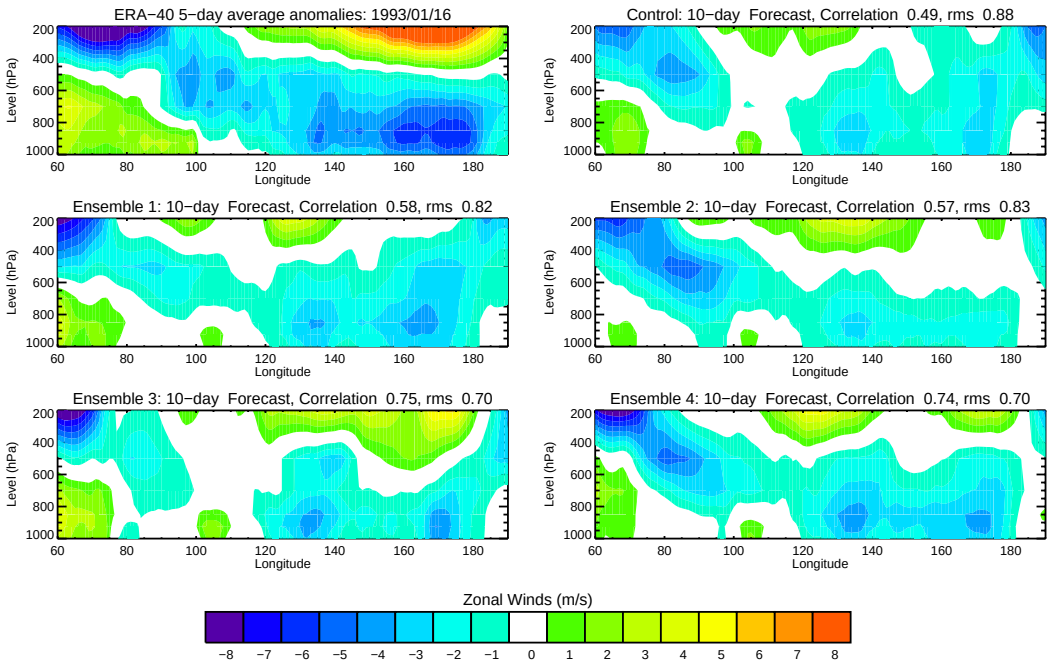

Figure 35: Vertical structure of 5-day average anomalies of zonal winds from ERA-40 for January 16 1993 and 10-day forecasts control forecasts and 4 ensemble members.

to convective activity. The average correlation and standardized RMS estimated from the vertical structure of the anomalies from 1000 to 200mb are presented in Figure 37 for the control run and all ensemble members, showing a similar overall forecast skill for all of them. Results among the ensembles are also similar for specific humidity.

3.1.2 ECMWF Forecast during the Transition Phase: Local vertical structure

The period selected for the analysis of the skill of the local vertical structure from the model output corresponds to the transition phase of both ISO events observed during the TOGA COARE IOP. The experimental design allows investigating the prediction of the ISO with initialization before, during and after the maximum intensity of the oscillation.

Figure 38a shows a time-pressure diagram of specific humidity anomalies from ERA-40 from December 5 to December 30 1992 in the IFA region. Anomalies are computed for each level relative to the mean ERA-40 values from November 1 1992

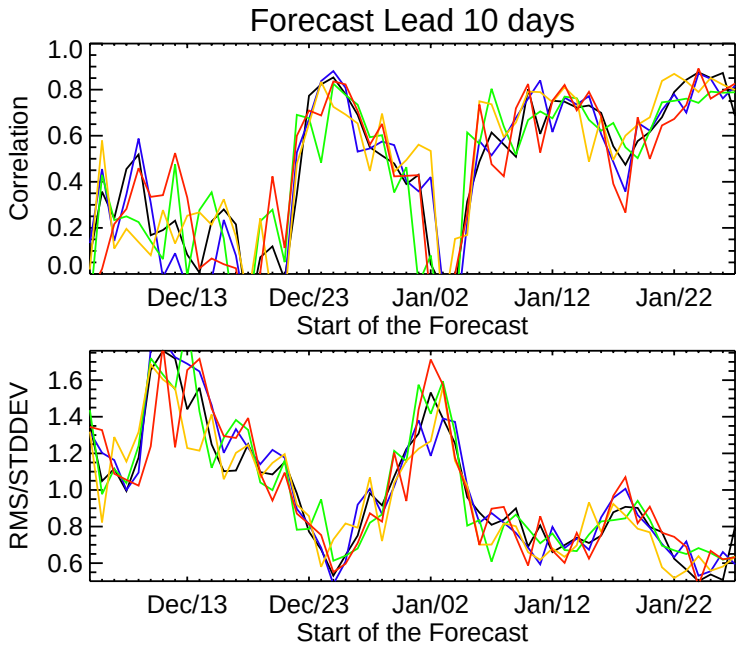

Figure 36: Correlation (top) and standardized RMS (bottom) for 10-day forecast lead time, for different starting dates. The black line corresponds to the control forecast and the color lines to each of the 4 ensemble members.

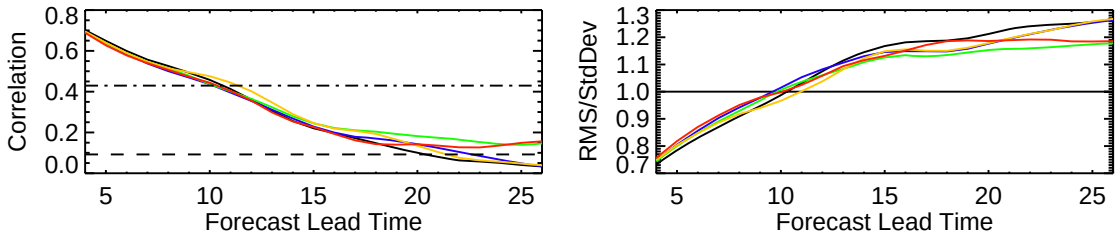

Figure 37: Average correlation and standardized RMS estimated from the vertical structure of the anomalies from 1000 to 200mb for the control run and all ensemble members.

to February 28 1993 in the same way that the anomalies were determined in Chapter 2. In this case we don't use the 5-day averaging used in the previous section. Figure 38a shows the specific humidity anomalies as seen in the ERA-40 data.

Since the general results from both transition periods are similar, only simulations for the first event are discussed here. Results of two integrations, one starting December 5 (Figure 38) just before the observed low-level moisture build up, and the other

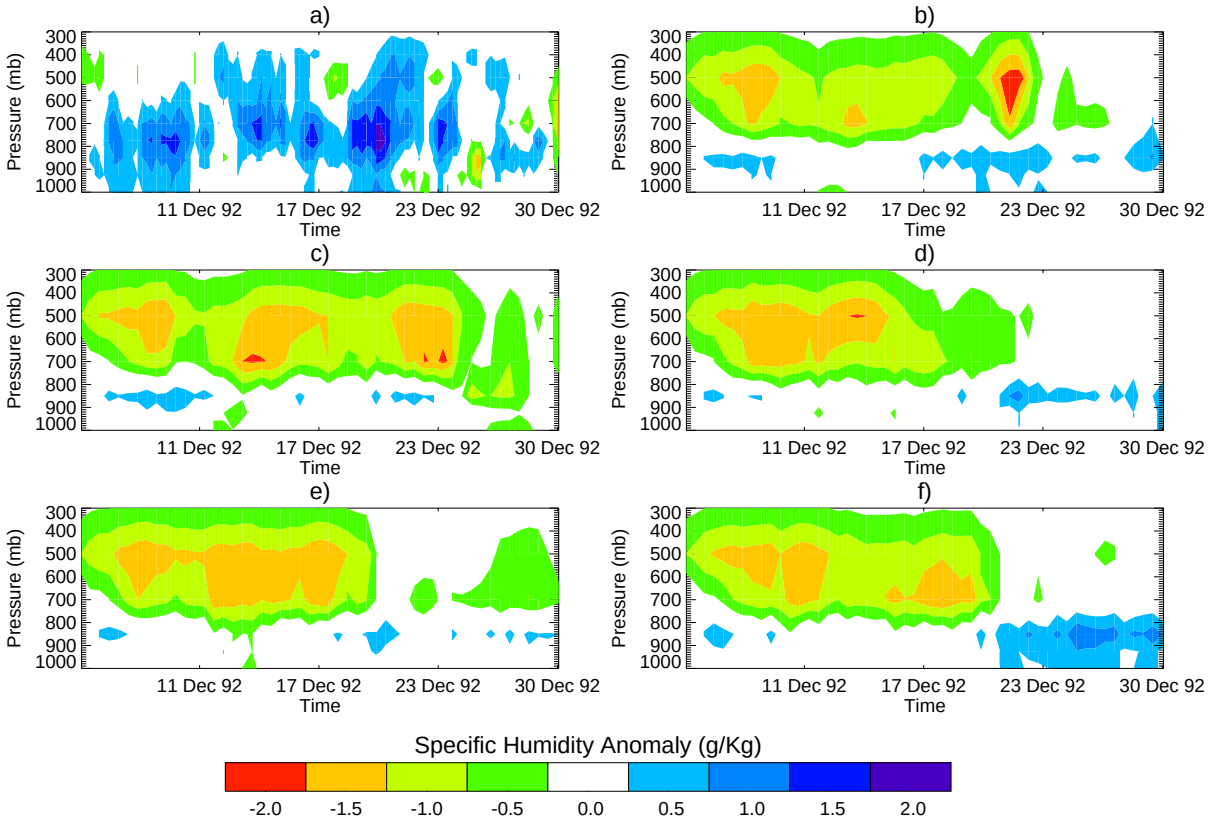

Figure 38: Time-pressure diagram of specific humidity anomalies over IFA from: a) ERA-40; b) the control run initialized December 5 1992; c) to f) each ensemble member.

starting December 15 (Figure 39) after the low level moisture has been observed to occur (and was included in initialization), summarize the general skill of the model in simulating the low-level moistening during the transition period.

Figure 38b to Figure 38f show specific humidity anomalies relative to the mean ERA-40 values during IOP for the control forecast and the four ensemble members. None of the simulations, including all ensemble members, reproduce the general character of the IOP observations or the ERA-40 data set. While moistening and deep convection are absent in all of the runs, an anomalously dry upper troposphere is formed by each simulation in each of the ensembles. This dryness appears to develop from the negative anomalies of specific humidity present in the initial conditions at December 5 around 500 hPa. Model results of the December 15 run including the

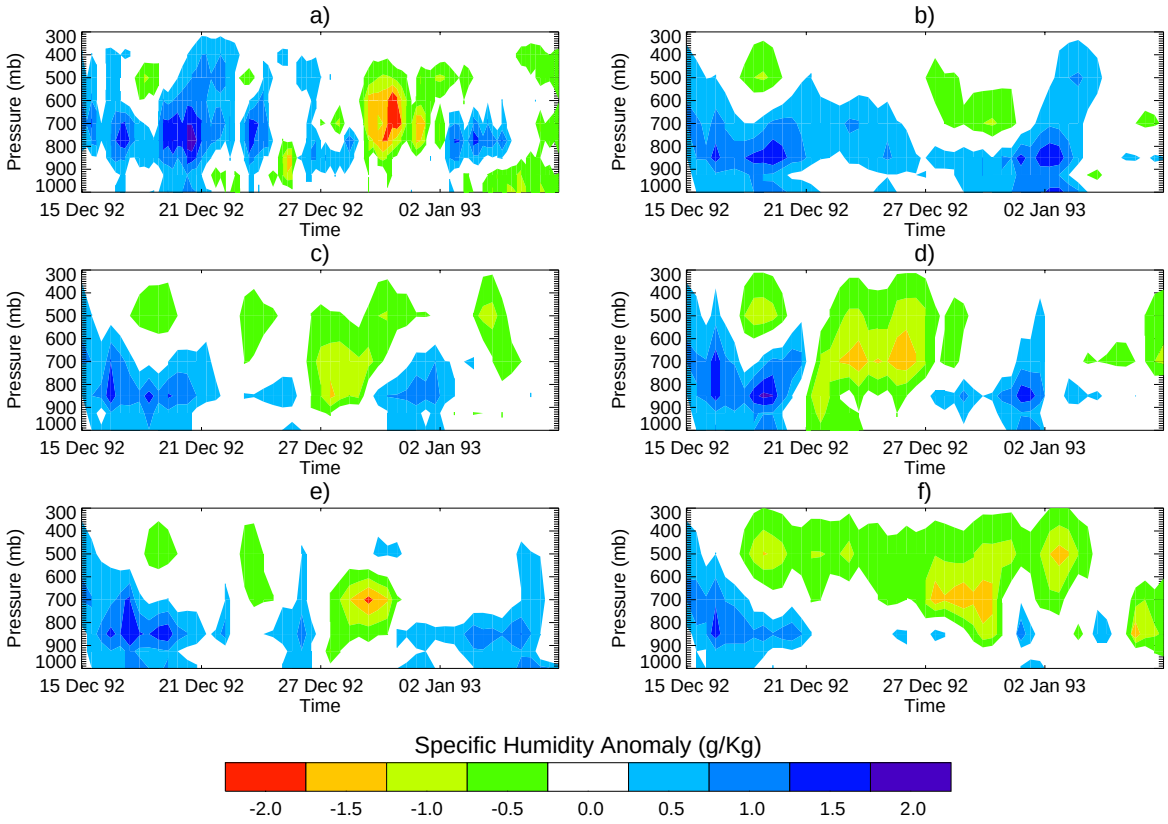

Figure 39: Same as Figure 38, but initialized December 15 1992.

four ensemble members (Figure 39) show improvement for the first 5-7 days of the forecast in all ensemble members. In this case, with the atmosphere initialized to be already moist, the model was able to sustain the anomaly although deep convection did not form.

In summary, all runs from December 1 to December 20 show similar results: the model was not able to develop moistening when it was not already present in the initial conditions and maintained an overly dry upper troposphere. However, when the initial conditions contained positive anomalies of specific humidity, forecasts were improved considerably at least for the first week of integrations. In other words, the model was not able to forecast the moistening of the middle troposphere through the transition stage. Since observations indicate that the low-level moistening during the transition is an integral and important part of the ISO, this failing is potentially one

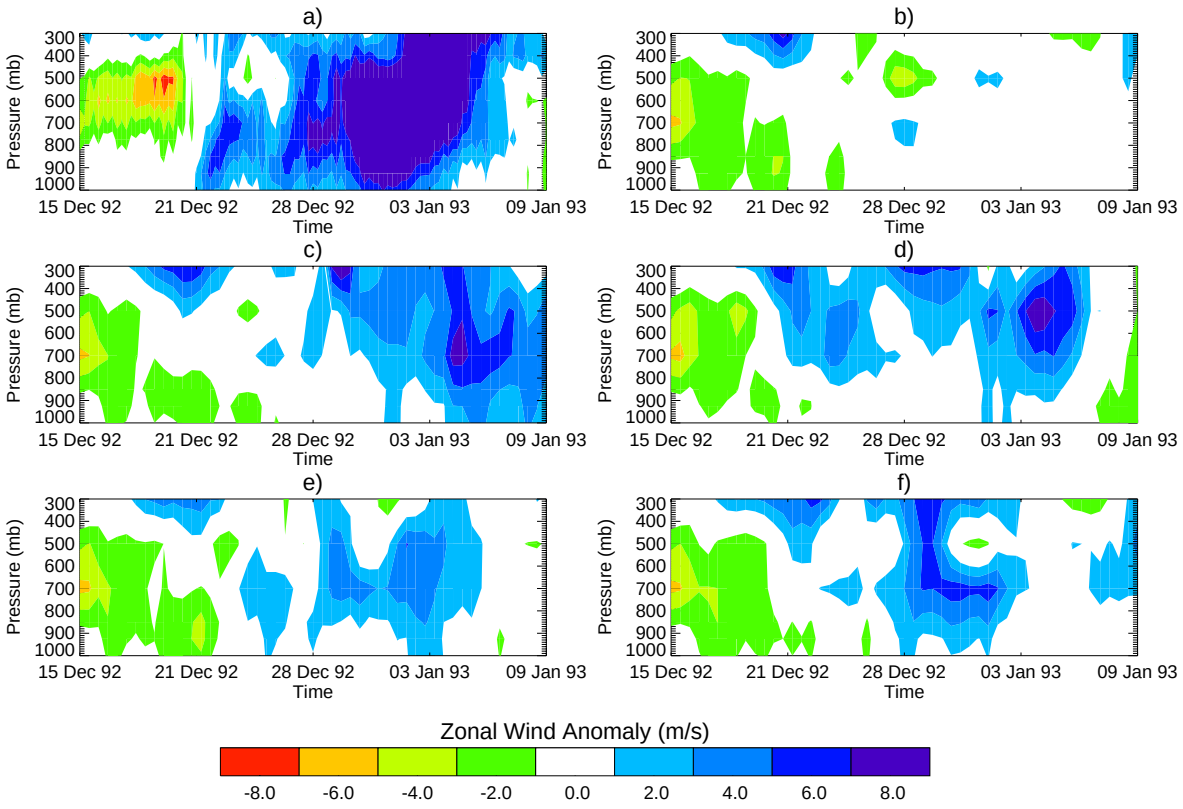

Figure 40: Time-pressure diagram of zonal wind anomalies over IFA from: a) ERA-40; b) the control run initialized December 5 1992; c) to f) each ensemble member.

of the obstacles hindering extended forecasts of intraseasonal activity using numerical models.

Figure 40 and Figure 41 show the zonal wind anomalies for the IFA region relative to the mean ERA-40 values during IOP for the reanalysis, the control forecast and the four ensemble members, starting December 5 and December 15 respectively. The results of these two runs also summarize the general findings of the forecasts during both transition periods during IOP. Regardless of the ISO phase, the skill of the model forecast of zonal winds, and in general all dynamical fields, appears to be higher than the skill for thermodynamic fields like temperature and specific humidity This coincides with the results obtained in the previous section. Even though model skill increases for zonal winds, capturing reasonably well the reversal of the winds

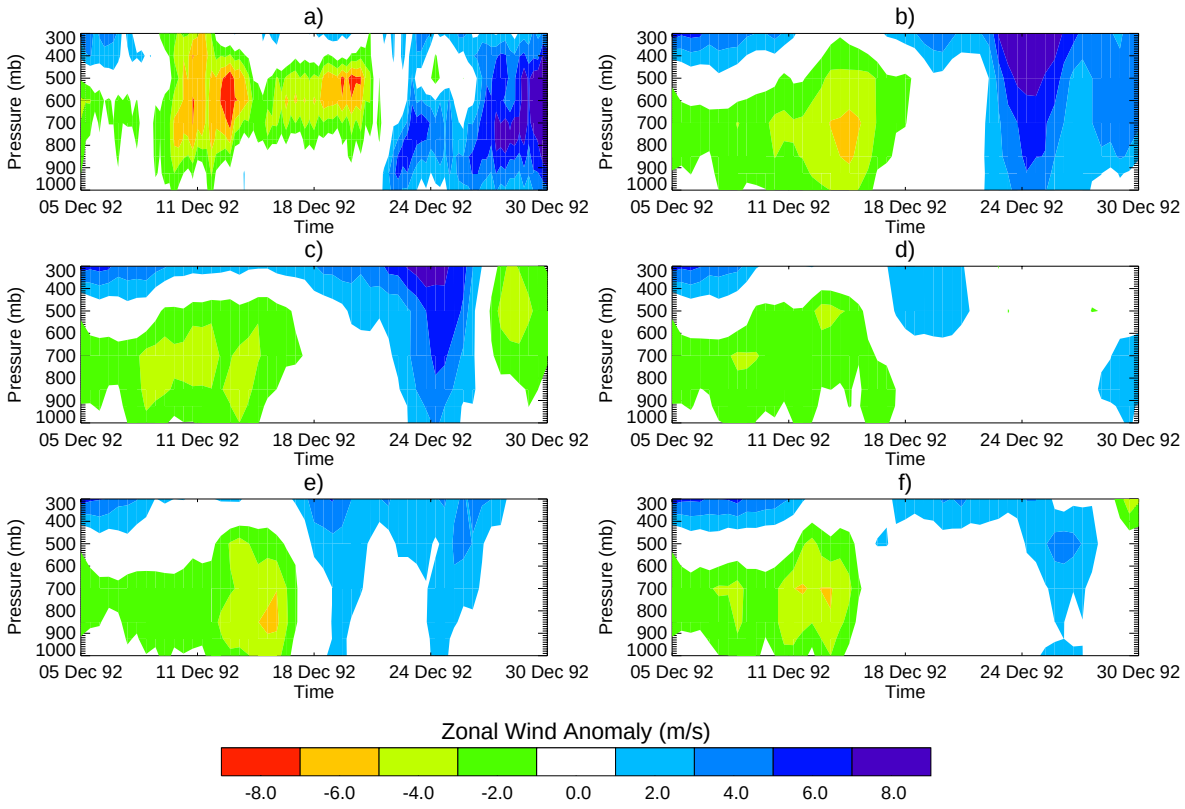

Figure 41: Same as Figure 40, but initialized December 15 1992.

associated with the ISO event, the magnitude of the forecast winds is only a third of that observed during the IOP (Table 1) and in the ERA40 data set (Figure 40a and Figure 41a). As shown in Figure 40 and Figure 41, the underestimation of the wind magnitude is greatest in the runs where the low-level moistening is not present in the initial conditions.

When results from the model for variables like surface latent heat flux and top of the atmosphere thermal radiation (Figure 42) are compared with observed and reanalysis data, important differences are evident, once again, for the runs starting December 5. In the case of the latent heat fluxes, differences over 20 Wm^2 are seen (Figure 42a) for all the ensemble members even during the first days of the integration, resulting in less water vapor input into the lower troposphere. For the run starting December 15 the model results for surface latent heat flux are very close

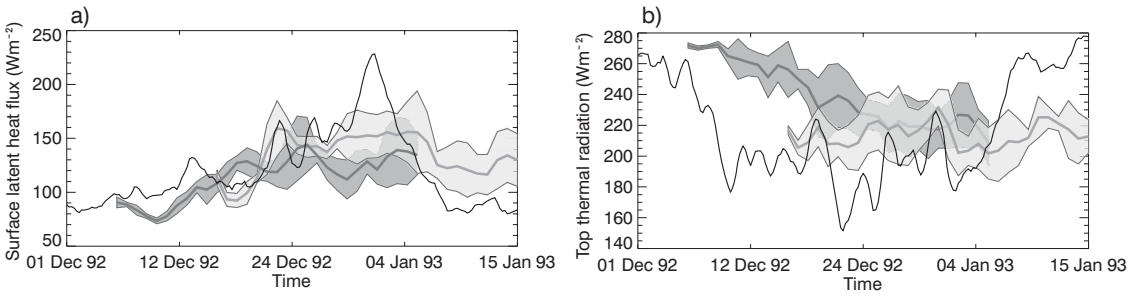

Figure 42: Forecasts of a) Surface latent heat flux (Wm^2) and b) Top thermal radiation (Wm^2) starting December 5 (dark-gray line) and December 15 (light-grey line) 1992. The shadowed area represents the spread of the five ensemble members (plus and minus one standard deviation). The black line corresponds to the ERA40 values.

to the observations especially for the first eight days of the integration. For the top of the atmosphere thermal radiation (OLR Figure 42b), both integrations show poor skill. In particular, the December 5 run shows discrepancies over 100 Wm^2 during the first week of the integration.

As a final diagnostic, CAPE was estimated from the ERA-40 and model results in order to identify potential differences with the values obtained using the observations. Figure 43 shows how both the amplitude and the variability of ERA-40 and the model are much smaller than the ones presented in Figure 16. CAPE results once again provide evidence of model problems in accurately representing important convection related variables.

3.2 Analysis of the 2002 and 2004 summer ISO cases

In this section we concentrate on the analysis of two different ISO cases that took place during the boreal summers of 2002 and 2004, comparing the results with those obtained for the TOGA COARE case. As it was mentioned before, the character of the winter and summer ISO is different. The main difference is the northward propagation of convective anomalies over the Indian Ocean during summer, which is not present during winter. For this reason we include the analysis of zonally average

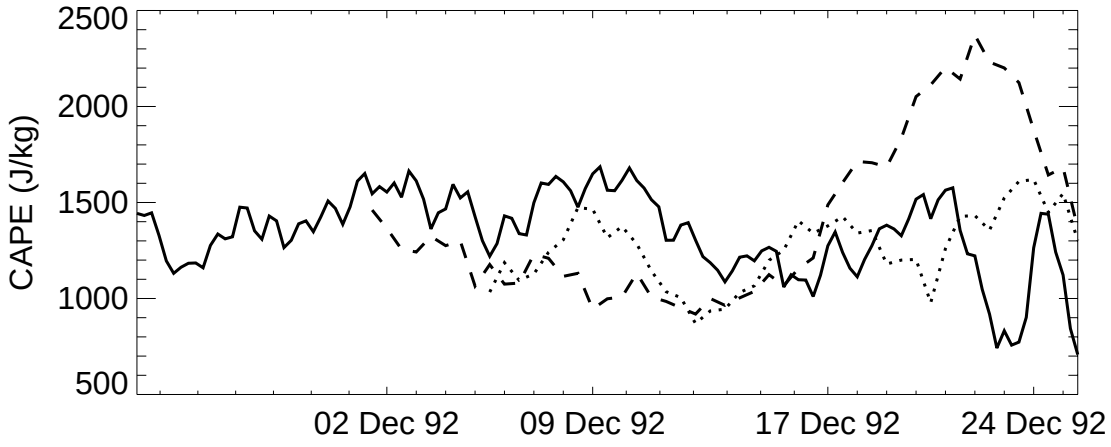

Figure 43: 12-hour CAPE estimates for ERA40 (solid line), the control run initialized December 1 1992 (dashed line) and December 5 1992 (dotted line).

meridional wind anomalies in the longitudinal band between 70 and 90°E as well as the specific humidity anomalies in the same band.

Figure 44 and Figure 45 show the distribution of the correlation and standardized RMS as a function of forecast lead time and start of the forecast for vertical anomalies of zonal winds in the Indo-West Pacific region (similar to Figure 30) for the 2002 and 2004 cases, respectively. The general results are similar between both cases and the TOGA CARE case previously analyzed: the forecast amplitude of the 5-day average zonal circulation anomalies is smaller than those in ERA-40; and the skill of the forecast decreases for convective episodes regardless of the starting date of the forecast (diagonal pattern in the Figure 44 and Figure 45). There is a significant difference, however, with the results obtained for the winter case. The time scale of skillful forecasts (where standardized RMS¡1) during summer is between 5-7 days while in winter it is at least double. While the analysis is not comprehensive as it only includes three serial experiments, it suggests that the skill of the forecast is greater for winter ISO cases than for summer events. This result is most likely due to the fact that the circulation structure of the summer ISO is more complex as it has not only an eastward propagating branch but also a northward propagating one. Since

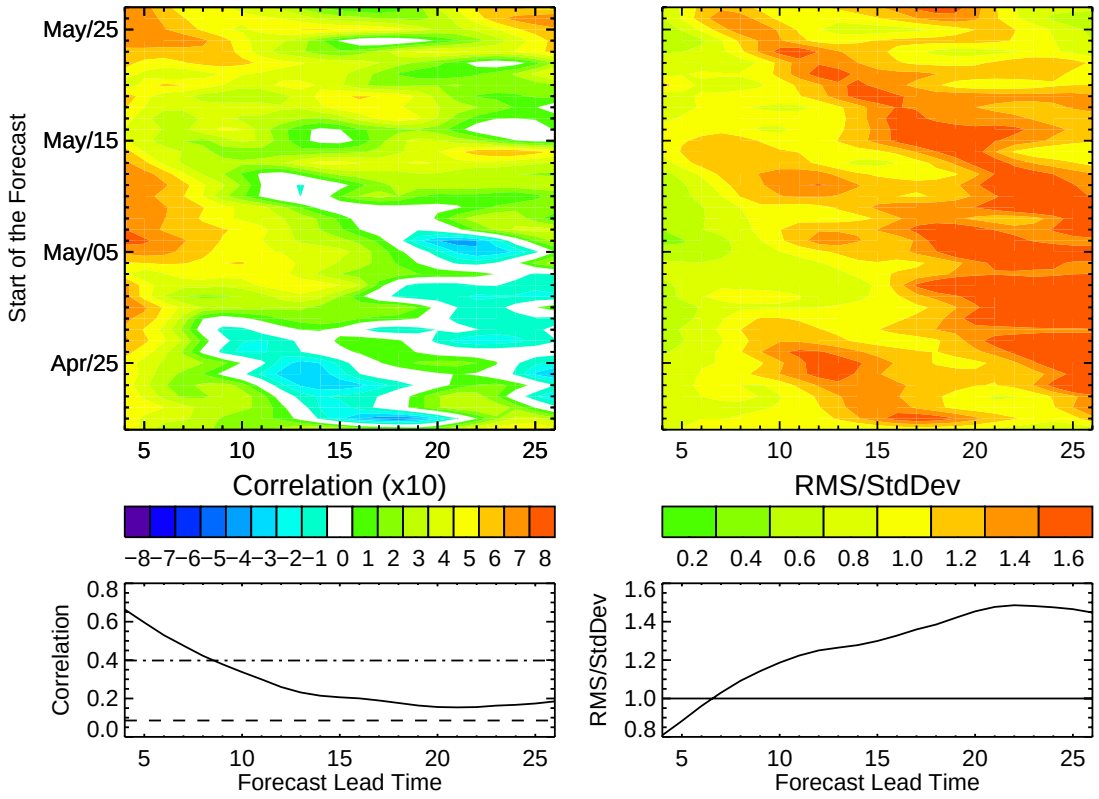

Figure 44: Same as Figure 30 but for the 2002 summer case

the results for both summer cases are similar, from this point onwards only results for the 2004 case will be presented. Analysis of the vertical structure of meridional wind anomalies also shows an average time scale of skillful forecasts around 7 days (Figure 46).

Analysis of the vertical structure of specific humidity anomalies presents an interesting feature different from the results during winter. While the zonal vertical structure around the equator shows very similar results to those during winter (Figure not shown): significantly lower forecast skill for specific humidity than for zonal (and meridional) wind with the model predicting a drier atmosphere than the ERA-40 data, the results for the meridional vertical structure of specific humidity are, at first glance, counter intuitive (Figure 47). Both the increasing correlation and the decaying RMS for forecast lead times greater than 8 days would suggest that the

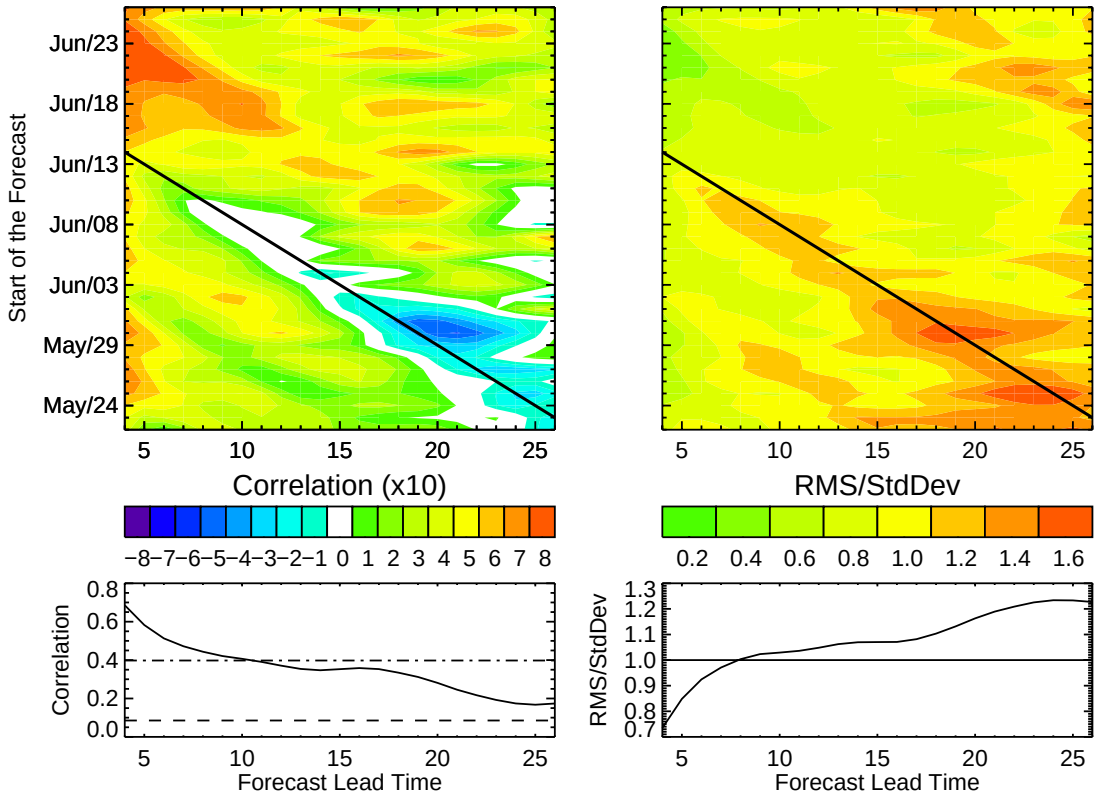

Figure 45: Same as Figure 30 but for the 2004 summer case

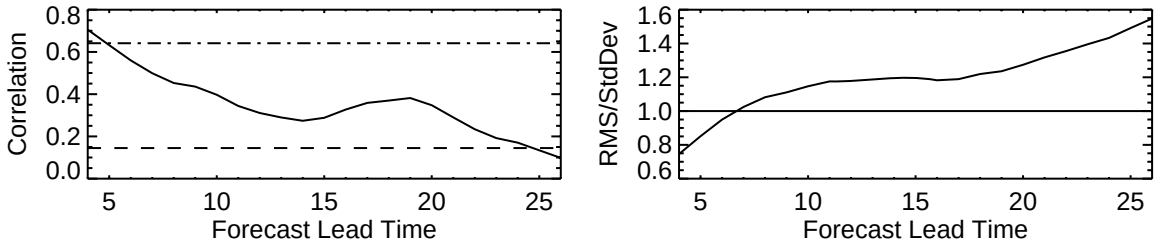

Figure 46: Average correlation (left) and RMS (right) for meridional wind anomalies and for each forecast lead time.

forecasts become more skillful as the forecast window increases. Since this is not likely, understanding what is causing this result points to a critical aspect of the model. Figure 48 shows the 5-day average specific humidity anomalies for 4 different dates from ERA-40 and for 10-day forecasts of the same dates. The four ERA-40 panels (Figure 48a, b, e, and f) show the evolution of a typical summer ISO event:

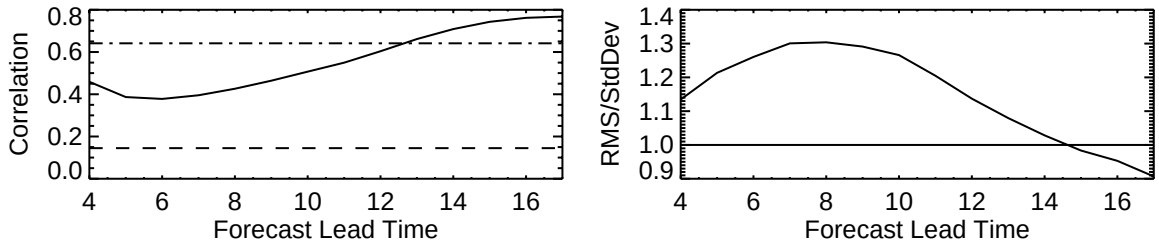

Figure 47: Same as Figure 46 but for meridional specific humidity.

In Figure 48a, the anomalies show the start of an active phase around the equator and predominantly suppressed conditions over the continent. During the transition stage (Figure 48b) convection starts over the continent. In Figure 48e, and Figure 48f convective anomalies have already move northward completely and suppressed conditions dominate the equator. The diagrams also show evidence of the weaker convective branch that propagates southward. The skill of the 10-day forecast is higher when convection is occurring over India. However, we argue that this result is purely coincidental and an indirect consequence of ISO-related simulation problems in the model. Active and suppressed convection over the continent during summer are controlled by the propagation of positive and negative intraseasonal anomalies that originate over the equatorial Indian Ocean. Since the model is not able to skillfully forecast the generation of specific humidity anomalies in the Indian Ocean around the equator as shown in the analysis of zonal vertical structure, convective anomalies would not propagate from the equator. This means that other mechanisms different than ISO are modulating the rainfall over the South-East Asian continent in the model: what is shown in the 10-day forecasts in Figure 48 is evidence of the annual character of the monsoon and not of intraseasonal variability. In other words, the model forecasts are reproducing reasonably well the structure of the monsoon with significant rainfall north of 15°N. Since the model does not reproduce the suppressed and active sequence, the result is a permanent active-like phase in the forecast over

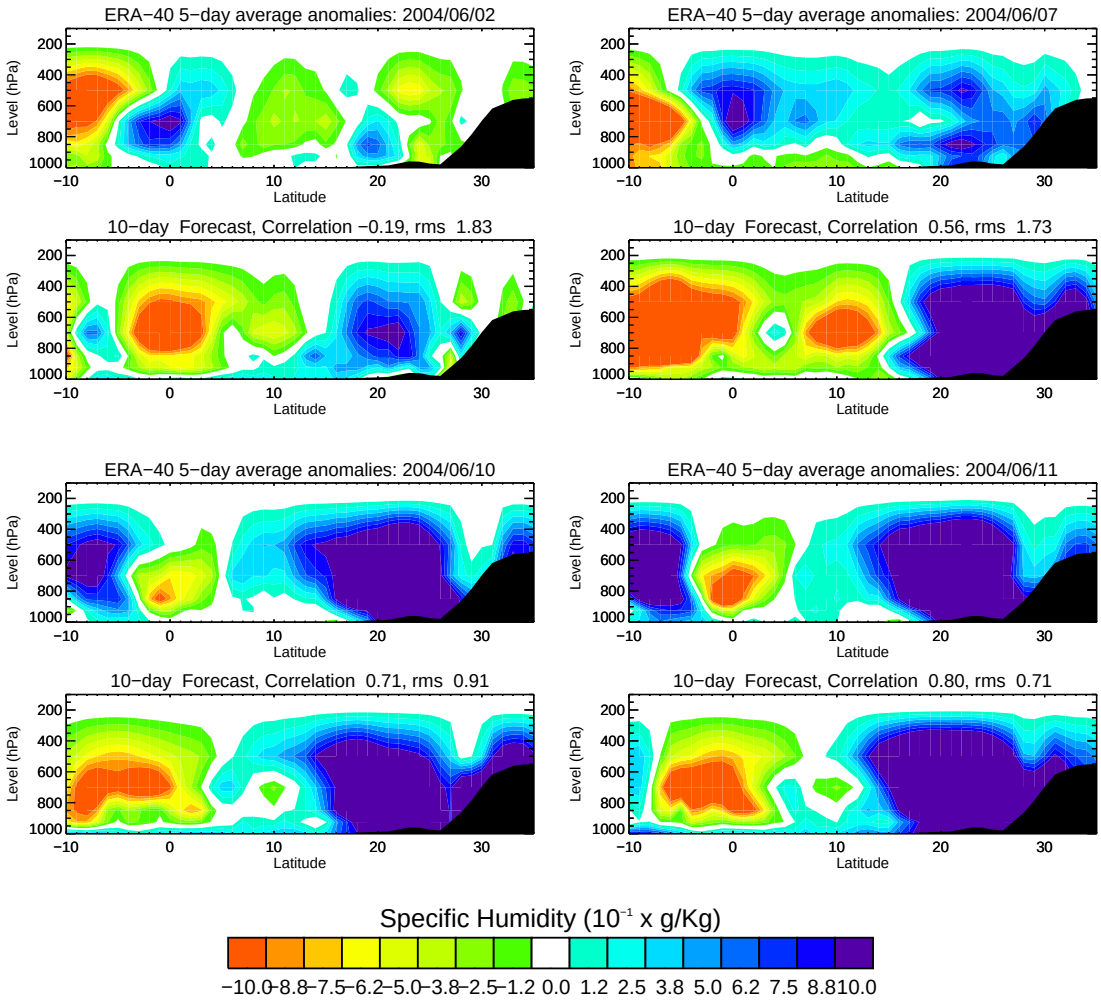

Figure 48: 5-day average specific humidity anomalies for four different dates from ERA-40 (a, b, e, f) and for 10-day forecasts (c, d, g, h).

India. Since the model is always forecasting an active-like phase of the monsoon, it will match the observations when actual active conditions are present over India, artificially increasing the skill in some phases.

To study the skill of the local vertical structure of specific humidity and its dependence of the convective phase, a similar analysis as the one presented in section 3.1.2 is performed for the 2004 summer. In this case the analysis is for a region in the center of the Bay of Bengal, where low level moistening is also evident prior to the deep convective event. Figure 49a and Figure 50a show the specific humidity

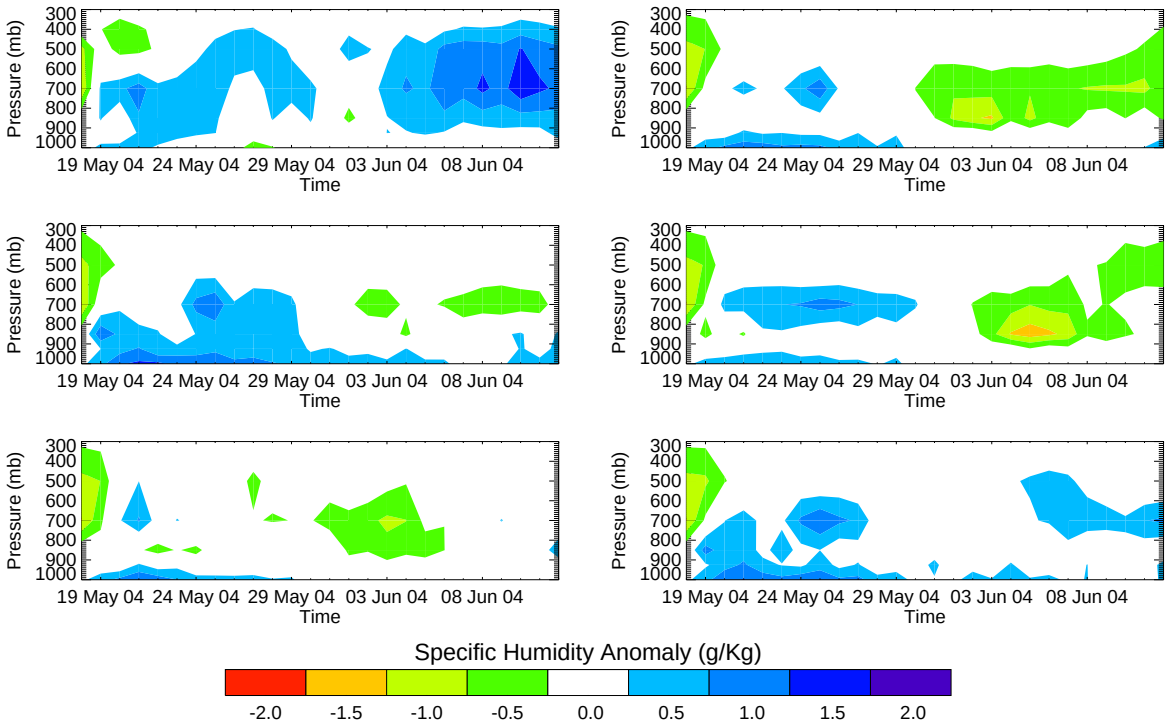

Figure 49: Same as Figure 38, but initialized May 18 2004 and for the Bay of Bengal.

anomalies of ERA-40 starting May 18 2004 and May 24 2004, prior to and during the low level moistening preceding the deep convective event. Figure 49b to Figure 49f and Figure 50b to Figure 50f show the control and the 4 ensemble forecasts for both cases. As it was obtained for the TOGA-COARE case, the skill of the forecast considerably improves when the low level moistening is already present in the initial conditions.

In general the analysis of both local and regional vertical structure associated with ISO for both summer and winter cases suggests five main conclusions: (i) the forecast skill of circulation anomalies is higher than the skill of moist convective anomalies;(ii) while the structure of the circulation anomalies present a similar pattern than the observations but with weaker amplitude, the model forecasts of specific humidity suggest a tendency to generate a dry atmosphere; (iii) forecasts tend to generate a more stable atmosphere;(iv) the skill of the forecasts of ISO-related anomalies for

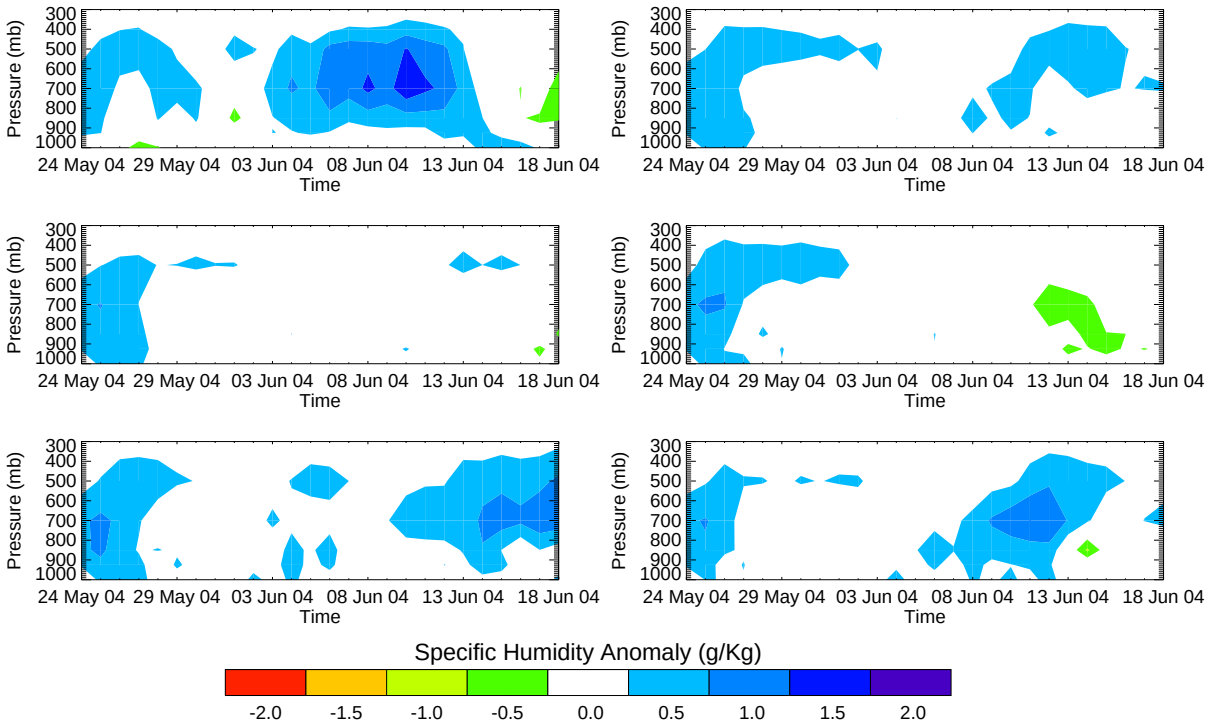

Figure 50: Same as Figure 38, but initialized May 24 2004 and for the Bay of Bengal.

summer is lower than that for winter; and (v) the forecast skill of the local ISO-related convective activity increases when low-level moistening is included in the initial conditions.

CHAPTER IV

TRANSITION FROM SUPPRESSED TO ACTIVE CONVECTION USING A COUPLED SINGLE COLUMN MODEL

In Chapter 2, a diagnostic analysis was presented of the variability of the atmosphere-ocean system during the transition stages between suppressed and active convection in the intraseasonal time scale. Results of the evaluation of a numerical model presented in Chapter 3 showed the lack of skill of the model to forecast deep convective events, and in particular, that lack of skill to represent the low-level moistening observed during the transition phase, hindering the prediction of the following convective event. A good representation of the transition is likely to be important to model and forecast the active phases of the ISO. In this chapter we present a numerical experiment aimed to further understand the causes for lack of skill in numerical models as well as to evaluate the importance of local thermodynamic coupling of the atmosphere and the ocean in the representation of the transition stage and the subsequent deep convection.

As mentioned in Chapter 1, in general, the tropical atmospheric circulation is very sensitive to small SST changes in the tropical western Pacific Ocean warm pool region (e.g., Palmer and Mansfield 1984) while at the same time SST and the ocean mixed layer structure in the warm pool are very sensitive to changes in the surface heat, momentum, and freshwater fluxes driven by the atmosphere (Clayson and Chen 2002). In this region one-dimensional processes are regarded to dominate the upper-ocean heat budget due to the small horizontal temperature gradients and weak surface currents (Shinoda and Hendon 1998, 2001; Waliser et al. 1999). Horizontal advection, although sometimes locally large (e.g. Feng et al. 2000), plays a minimal role in

governing the broad scale SST anomalies produced by the ISO in the heart of the warm pool. Shinoda and Hendon (1998) showed that intraseasonal SST variations in the western Pacific and Indian Ocean warm pool were well simulated using a one-dimensional mixed layer model. In other words, SST variations in the warm pool associated with the ISO appear to be primarily driven by surface heat flux variations.

A coupled Single Column Model (SCM) forced with the observed 3-D wind structure was used in this study. A SCM represents essentially the column physics of a GCM, considered in isolation from the rest of the GCM (Randall et al. 1996). The combination of detailed physics and a computationally economical framework makes SCMs a useful tool for organized strategies to explore different hypotheses in a variety of scenarios. SCMs allow isolation of the local thermodynamic processes, which is useful to study the local interactions between the atmosphere and the ocean. SCMs can also be used to confront models with different sources of data, and evaluate the ability of physical parameterizations to reproduce observations. Also, they can be used to produce synthetic data sets in a sensitivity framework to improve understanding of a variety of processes. Because an SCM lacks the horizontal feedbacks that occur in complete three-dimensional models, the governing equations are coupled only through the parameterized physics. In a practical sense this means that the thermodynamic and momentum components of the governing equations are generally independent of each other.

4.1 Model Description

The Single-column Community Climate Model (SCCM) is the atmospheric component of the couple system and corresponds to the single column version of the National Center for Atmospheric Research (NCAR) Community Climate Model 3.6 (CCM3.6; Hack and Pedretti 2000). The SCCM is a one-dimensional time-dependent model for which the local time rate of change of large-scale state variables like temperature,

moisture, momentum, cloud water, among others, depend on specified horizontal flux divergences, a specified vertical motion field, subgrid-scale sources, sinks and eddy transports. The subgrid-scale contributions are determined by the model parameterizations of the relevant physical processes, which are identical to those used in the full-scale Climate Community Model (CCM3).

The deep convection scheme used in SCCM was developed by Zhang and McFarlane (1995). In this scheme, Moist convection occurs only when there is convective available potential energy (CAPE) for which parcel ascent from the sub-cloud layer acts to destroy the CAPE at an exponential rate using a specified adjustment time scale. The model also accounts for the convective forcing associated with shallow and middle-level convection using a scheme based on budget equations for the dry static energy and total water. The cloud fraction in CCM3 is based on the Slingo (1987) algorithm as modified by Hack et al. (1993). This algorithm calculates convective cloud amount as a function of convective overturning. The atmospheric boundary layer parameterization uses the non-local scheme described by Holtslag and Boville (1993). This scheme determines an eddy-diffusivity profile based on a diagnosed boundary layer height and a turbulent velocity scale. It also includes non-local vertical transport effects for heat and moisture, and a direct coupling to the parameterization of deep and shallow convection.

The ocean component of the coupled SCM is the one-dimensional ocean mixed layer model described by Kantha and Clayson (1994, 2004). This model is a modification of the Mellor-Yamada model (Mellor and Yamada 1982) and uses a second-moment turbulence closure. This means that the conservation equations for turbulence Reynolds stresses, heat fluxes, and scalar variances are solved by parameterizing the unknown third-moment turbulence quantities, pressure-strain rate and pressure-scalar gradient covariance terms.

The basic equations for the mean and turbulence quantities in the ocean mixed

layer model describe a rotating, incompressible, stratified turbulent flow under the Boussinesq approximation. Essentially the equations solved in the model are the conservation of mass, momentum and scalar mean quantities, conservation relation for the second moments, the turbulence quantities, the Reynolds stresses, the turbulent heat fluxes, and the temperature variance. The model includes improved parameterizations of the pressure covariance terms developed based on large eddy simulations. The model includes the skin surface temperature parameterization developed by Wick (1995), and Schlüssel et al. (1997) to include the effects of precipitation and the diurnal thermocline variation. Parameterizations for Langmuir circulation and wave breaking effects were also included by Kantha and Clayson (1994).

This ocean mixed layer model has been evaluated over many timescales and in many locations, including data from the TOGA COARE pilot cruise (Kantha and Clayson 1994) and the IOP (Webster et al. 1996). Comparisons of the model turbulence characteristics including dissipation have been validated against data from the R/V Moana Wave during the IOP (Clayson and Kantha 1999).

The ocean-atmosphere interaction in the model occurs through the transfer of heat, moisture, and momentum across the atmosphere-ocean interface. These fluxes are determined by the state of the atmosphere and ocean boundary layers near the interface. These boundary layers are then strongly modified by the surface fluxes. The temperature of the ocean skin, which plays the role of interface between atmospheric and oceanic boundary layers, is a key factor in the exchange of heat and moisture between them. This skin temperature is explicitly calculated within the coupled model (using the Wick 1995 parameterization).

In the coupled model, the atmospheric component provides the near-surface horizontal wind speeds, air mixing ratio, air temperature, precipitation rate, and downwelling shortwave and longwave radiation to the ocean at each time step. These values, combined with the skin surface temperature previously determined by the

ocean model, are used as inputs to a turbulent flux model (Clayson et al. 1996). The modeled turbulent fluxes drive then the evolution of the ocean mixed layer. In response to the surface fluxes, the ocean model determines a new profile of temperature, salinity, and horizontal velocity. The newly determined SST is used to provide the atmosphere model with an updated surface moisture and latent heat, sensible heat, and upwelling longwave radiation fluxes (Clayson and Cheng 2002).

It is important to note that the simplifications that make SCMs computationally efficient also create sources of error that, if not handled appropriately, might compromise results obtained from such models. In general, atmospheric temperature fluctuations result from the interaction between diabatic and adiabatic tendencies. Diabatic tendencies in SCMs are calculated using detailed physics parameterizations, while adiabatic tendencies (i.e., advection by the large-scale flow) are either neglected, fully specified or calculated from a combination of specified and predicted terms (Randall and Cripe 1999), resulting in a decoupling of both tendencies. Such decoupling in the SCM framework, might introduce large errors with damaging consequences for SCM diagnosis, since the physics modules in the SCM could generate clouds, radiative fluxes, and precipitation from unrealistic thermal structures (Bergman and Sardeshmukh 2004). To avoid the effect of the decoupling, a strategy is to analyze the short-term behavior (8-15 days) of the SCM. In this manner, the analysis is performed before an unrealistic state can develop, eliminating the need to correct the imbalance between adiabatic and diabatic tendencies. Since the length of the transition phase is about 10-15 days, this approach is valid in the present study.

4.2 Results

The specific goal of this section is to evaluate the capability of the coupled single column model in simulating the local thermodynamical coupling during the transition

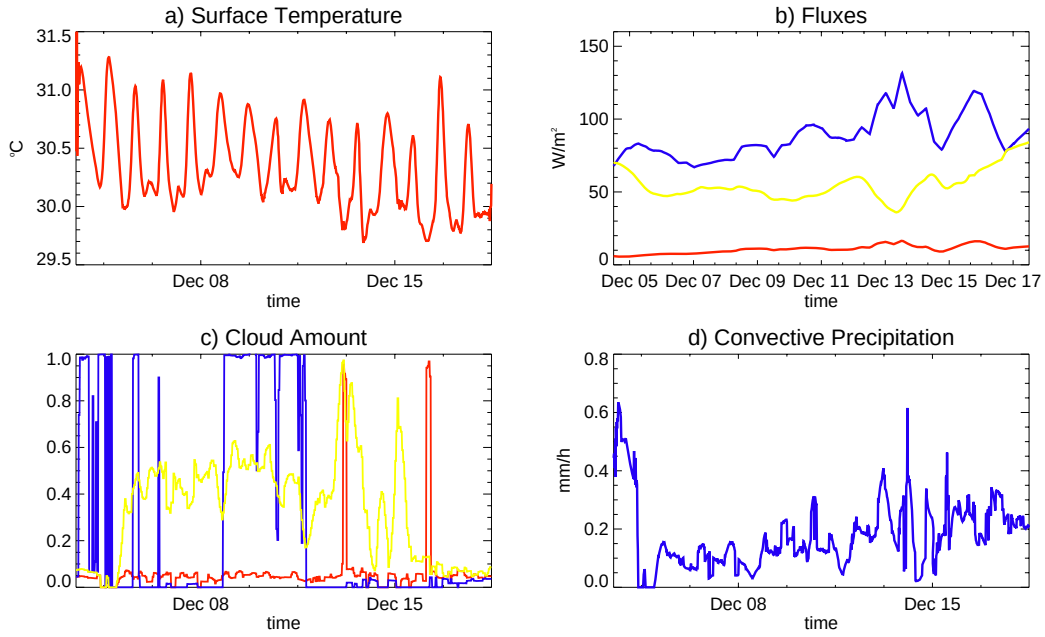

Figure 51: Model simulation corresponding to the first transition period during TOGA-COARE initialized December 03 1992 and using the original SSCM surface flux scheme (LV). The panels show a) SST; b) latent heat (blue) and sensible heat (red) fluxes, and net longwave radiation (yellow); c) high (blue), mid-level (red) and low (yellow) cloud fraction; and d) convective precipitation.

from suppressed to active convection with deep convective activity for extended periods of time. TOGA-COARE IFA data was used for the initial conditions as well as for the advective tendencies. Since the objective of this section is to study the evolution of local thermodynamics within the atmospheric column, moisture and temperature advection are not included unless specified in the text. In the simulations, three different schemes for the estimation of surface turbulent fluxes were evaluated: (i) the scheme included in the SSCM, originally written by Large and Vertenstein (here after LV scheme; www.ccsm.ucar.edu/models/ccsm3.0), based on a bulk formulation, (ii) the COARE bulk flux version 2.5b (Fairall et al. 1996), and (iii) the Clayson et al. (1996) flux scheme.

Results for the 15-day simulation using the coupled SCM corresponding to the first transition period during TOGA-COARE are presented in Figure 51 to Figure 53,

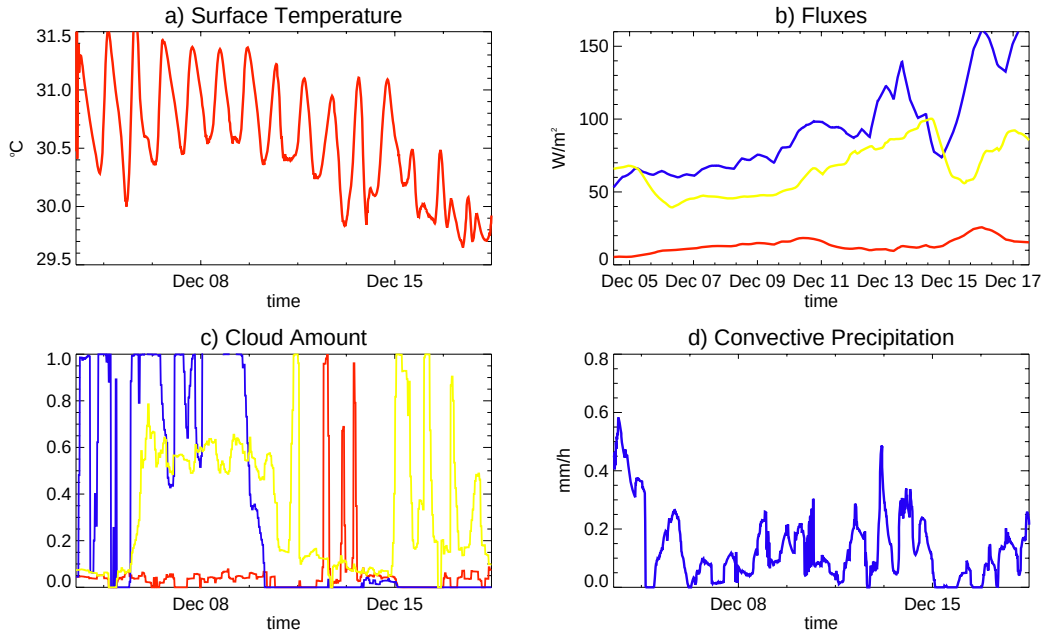

Figure 52: Same as Figure 4.1 but using COARE surface flux scheme.

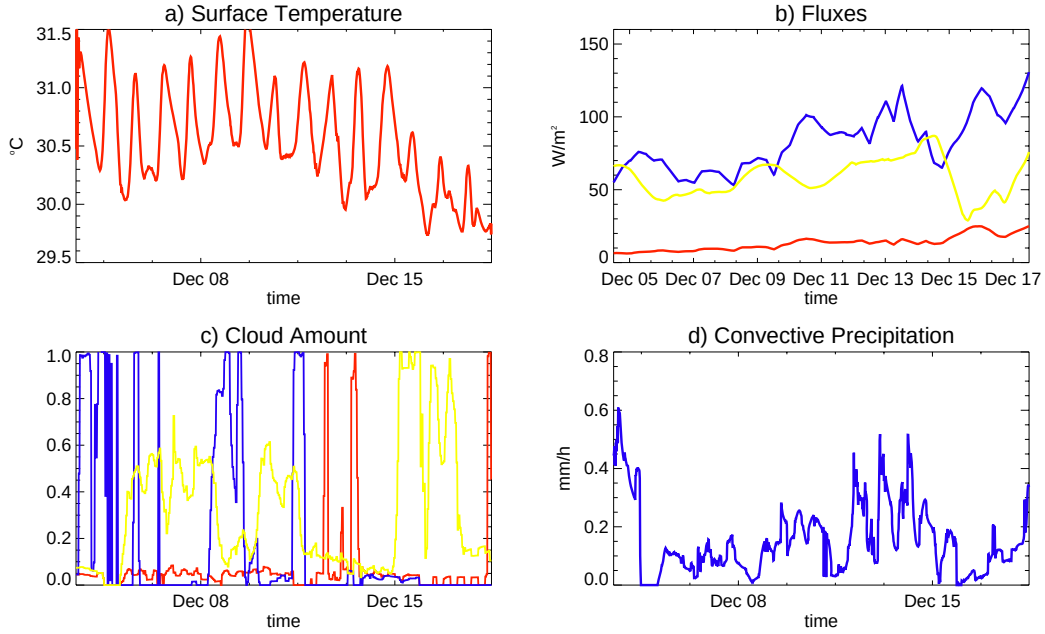

Figure 53: Same as Figure 4.1 but using Clayson et al. (1996) surface flux scheme.

showing the simulated SST, latent and sensible heat fluxes, net longwave radiation, high, mid-level and low cloud fraction, and convective precipitation for the three different flux schemes. The initial conditions correspond to December 03 1992. In

general, the model simulates reasonably well the observed decrease of SST during the end of the transition phase and the deep convection (see Figure 13a) using each of the three schemes (Figure 51a, Figure 52a and Figure 53a). The LV scheme reproduced better the observed linear shape of the SST decrease. However, simulations with each of the three schemes have similar problems. The magnitude of the simulated SST is about 0.5 degrees higher than in the observations and the amplitude of the diurnal cycle is also higher. One of the reasons for this difference, at least during the transition stage, appears to be the underestimation of the latent heat flux. While the different schemes estimate well during the transition the increasing trend in latent heat flux associated with the enhanced surface wind speed included in the 3-D forcing (Figure 51b, Figure 52b and Figure 53b), the simulated magnitude shows a significant underestimation of about 40-50 Wm^2 (compare to Figure Figure 13b).

Observations show that the diurnal cycle of SST is considerably smaller during the convective stage than during the suppressed phase mostly due to the radiative effects of the cloudiness, which reduce the net solar radiation at the surface. However, results of the simulations do not reproduce appropriately the reduction of the amplitude of the diurnal cycle. Figure 51c, Figure 52c and Figure 53c shows the significant differences between the simulated cloudiness and the estimations based on satellites retrievals (Figure 11 and Figure 23). One of the features shown in the simulations is the elevated high-frequency variability of cloudiness compared to the slow changes seen in the observations. In particular, the slow increase of mid-top non-precipitating clouds associated with the low-level moistening is not adequately simulated by the model. Since the variability of clouds is not well simulated, the evolution of the amplitude of the diurnal cycle of SST during the ISO life-cycle is poorly represented. Figure 51c, Figure 52c and Figure 53c show no coherent relationship between the fraction of any type of cloud and the convective rainfall (Figure 51d, Figure 52d and Figure 53d) and amplitude of the diurnal cycle of SST, suggesting a poor coupling

between the cloud parameterization and the radiative parameterization. The cloud fraction (total and at different levels) simulated by the model is also very sensitive to changes in surface flux. Figure 51c, Figure 52c and Figure 53c show substantial variations among the three different simulations using different surface flux schemes, not only in magnitude but also in the timing of the clouds at different levels within the first TOGA COARE transition. Such sensitivity to the estimation of the fluxes, which might or might not represent the actual sensitivity in nature, appears as one of the reasons why this type of model and others using similar parameterizations (e.g. CCSM3.0) have poor skill in the simulation of extended convective processes.

Convective rainfall also varies among the three simulations but not as strongly as the cloud fractions and SST. The major difference between the model and observations is in the temporal distribution of the rainfall. Observations during TOGA-COARE show that rainfall is clustered during the duration of the active phase, and no rainfall or small scattered events occur during the transition and suppressed phases. The model, however, simulates convective rainfall at every time step, at comparatively low rates. This error, induced by the nature of the convective parameterizations, does not allow the model to simulate the extended deep convective events observed in nature.

Figure 54 illustrates the vertical structure of the specific humidity using the LV flux scheme during the first transition event compared to the observations, showing the absolute values of specific humidity (Figure 54a and Figure 52b) as well as the anomalies relative to their own mean during the 15-day integration period (Figure 54c and Figure 54d). The first important feature is the significant underestimation of moisture in the simulation. Figure 55 presents the difference between observed and simulated specific humidity showing in detail the marked negative humidity bias in the simulations. While differences are expected between observations and simulation given that these are not forecasts, there is no a priori reasons to have a large

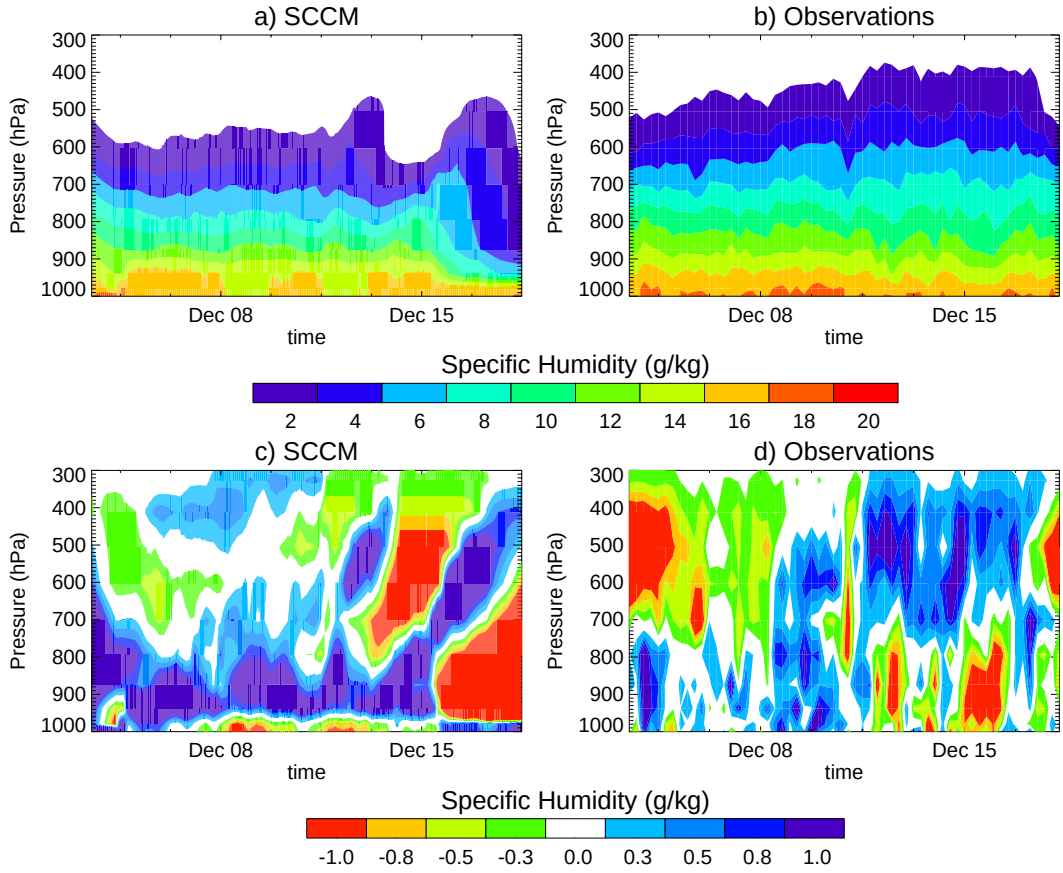

Figure 54: Evolution of the vertical structure of the specific humidity during the first transition event for a) absolute values of simulations using the LV flux scheme b) absolute values of observations, c) modeled anomalies; and d) observation anomalies.

negative bias in humidity. The previous analysis suggests that there are two major reasons for the negative bias in the moisture: (i) The underestimation of latent heat flux and (ii) the continuous convective rainfall in the simulation that does not allow the atmospheric moistening to take place. Simulations including the moisture and temperature advection show similar results with a negative bias of humidity.

The anomalies of specific humidity show interesting similarities and differences between simulations and observations (Figure 54c and Figure 54d). The first apparent feature is that anomalies in the simulation are considerably higher than in the observations, which is a combined result of the rapid response of the model to anomalies in SST and surface fluxes compared to the slow varying nature of the ISO

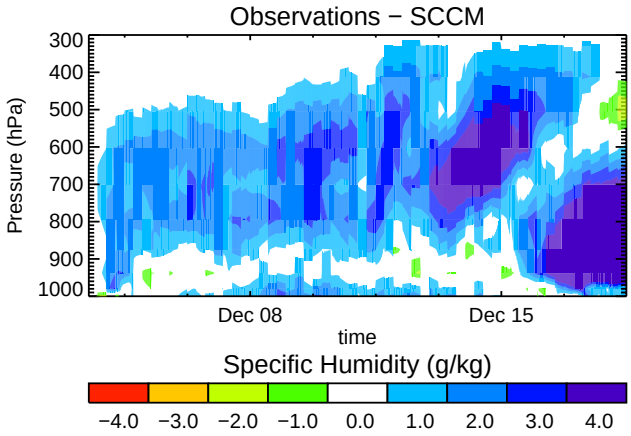

Figure 55: Difference between observed and simulated specific humidity values during the first transition period.

as suggested by observations. Considering the previously identified limitations of the model, this particular simulation appears to capture roughly some features of the low level moistening evident in the observations. The simulated atmosphere shows predominantly positive (negative) specific humidity anomalies in the low (high) tropospehere between December 3 and December 7 1992. This feature is also present in the observations. The moistening continues both in observations and the simulation between December 8 and December 132 1992. Deep convection also takes place during at the same time (around December 13). However, in spite of having the correct 3-D circulation forcing, moist convection in the model is not sustained as in the observations. After the onset of the convective event, the model atmosphere quickly dries out while the observations show positive anomalies of upper troposphere specific humidity throughout the entire active phase. After the first deep convective burst, the model quickly generates a second burst. In the context of this experiment, the second burst of convection during the active phase occurs owing to the rectification of the model given the forcing. In other words, the atmosphere is driven back to a convective state by the 3-D circulation used to force the model. However, in the context of a global climate or numerical forecasting model, the circulation and temperature anomalies

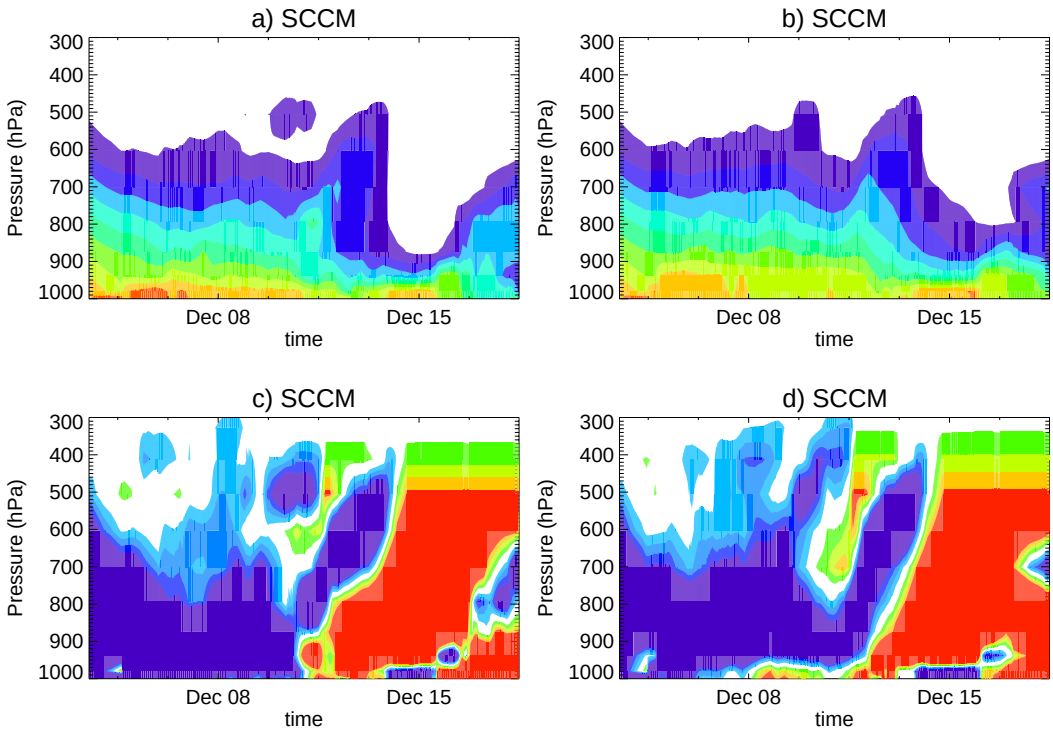

Figure 56: Same as Figure 4.4 but for the simulation using the COARE flux scheme (a and c) and the Clayson et al (1996) scheme (b and d).

introduced by this type of high frequency convective bursting could potentially limit considerably their skill to simulate and forecast the ISO. Convective bursts inhibit the build up of CAPE to sustain extended convective activity.

The vertical structure of the temperature profile in all the simulations is strongly tied to the evolution of specific humidity. This expected since temperature advection is not included and, as mentioned before, the equations for temperature and moisture are coupled through the physical parameterizations.

High sensitivity to the estimated surface fluxes is also observed in the vertical structure of the specific humidity. Figure 4.6 shows the absolute specific humidity (Figure 56a and Figure 56b) as well as the anomalies (Figure 56c and Figure 56d) of the same magnitude for the simulated first transition using the COARE flux scheme and the Clayson et al (1996) scheme. In these two cases the slow moistening of the

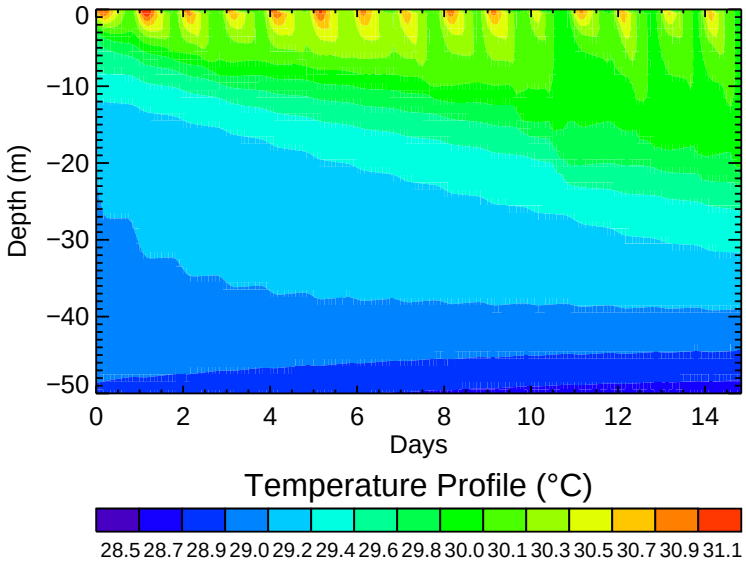

Figure 57: Temperature profile in the ocean for the simulation during the first transition period using the LV scheme. Oceanic advection is not included.

atmosphere is not as clear as when using the LV scheme. Also, after the first deep moist convection takes place the drying of the atmosphere is extended compared to using the LV scheme, and the atmosphere only starts to recover by the end of the simulation period. These differences observed in Figure 55 and Figure 56, which are completely due to changes in the estimation of surface fluxes, highlight once again the sensitivity of the coupled system to the local thermodynamical coupling as well as the degree of complexity involved in the simulation of the slow varying ISO anomalies.

Figure 57 shows the temperature profile in the ocean for the coupled simulation using the LV scheme. In this simulation no oceanic advection was included. However, simulations including advection derived from TOGA COARE data showed similar results. In contrast to the atmospheric component, the mixed layer model does a good job reproducing the deepening of the mixed layer from the transition to the active convection due to the enhanced surface winds as well as the cooling of the first 5 meters due to enhanced mixing and latent heat flux. Similarly as for SST, the absolute magnitudes differ from the observations due the underestimation of latent

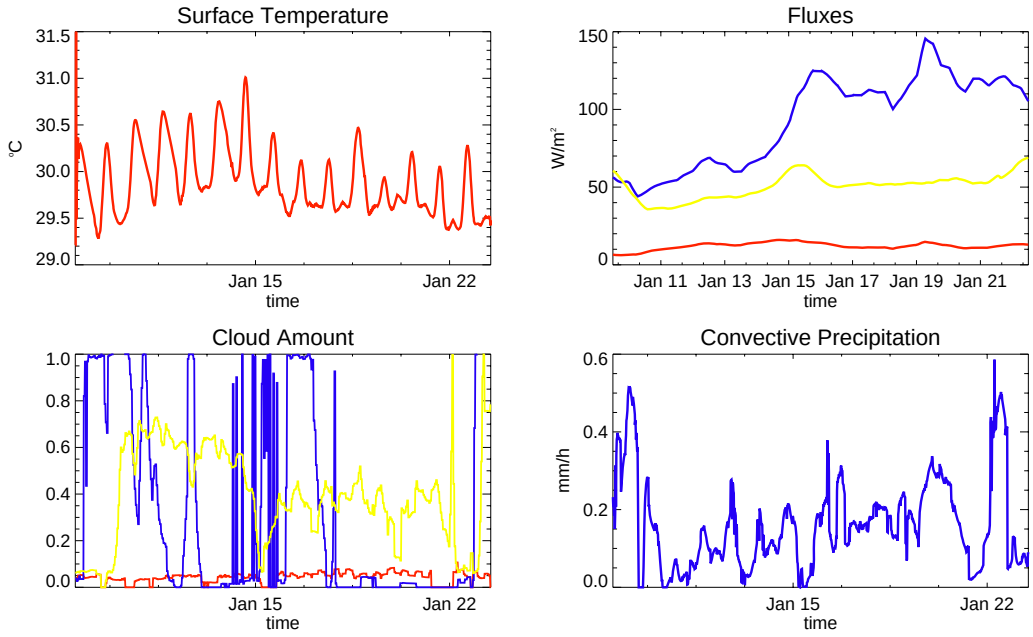

Figure 58: Same as Figure 4.1 but for the second transition period initialized January 8 1993.

heat flux. While there are differences between the resulting oceanic temperature profiles when using different schemes for surface fluxes, the variations results are not as drastic as in the atmosphere (Figure not shown). In all three cases the oceanic model reproduces well the deepening of the mixed layer, which is one of the most important oceanic features that occur during the transition and active phase.

Results for the second transition period are very similar to those obtained for the first period. For this case, the model is initialized January 8 1993. Figure 58 shows the SST, surface fluxes, cloudiness and convective rainfall for the simulation using the LV scheme. Contrary to the simulations for the first transition, the integrations for this case were started before reaching the maximum SST. The simulation represents the general behavior of the SST during the transition capturing well the maximum of SST and the following decrease before the peak of the convective phase. However, the latent heat flux is also underestimated as it was in the first simulation and convective rainfall is generated at almost all time steps. Figure 59 shows the vertical structure

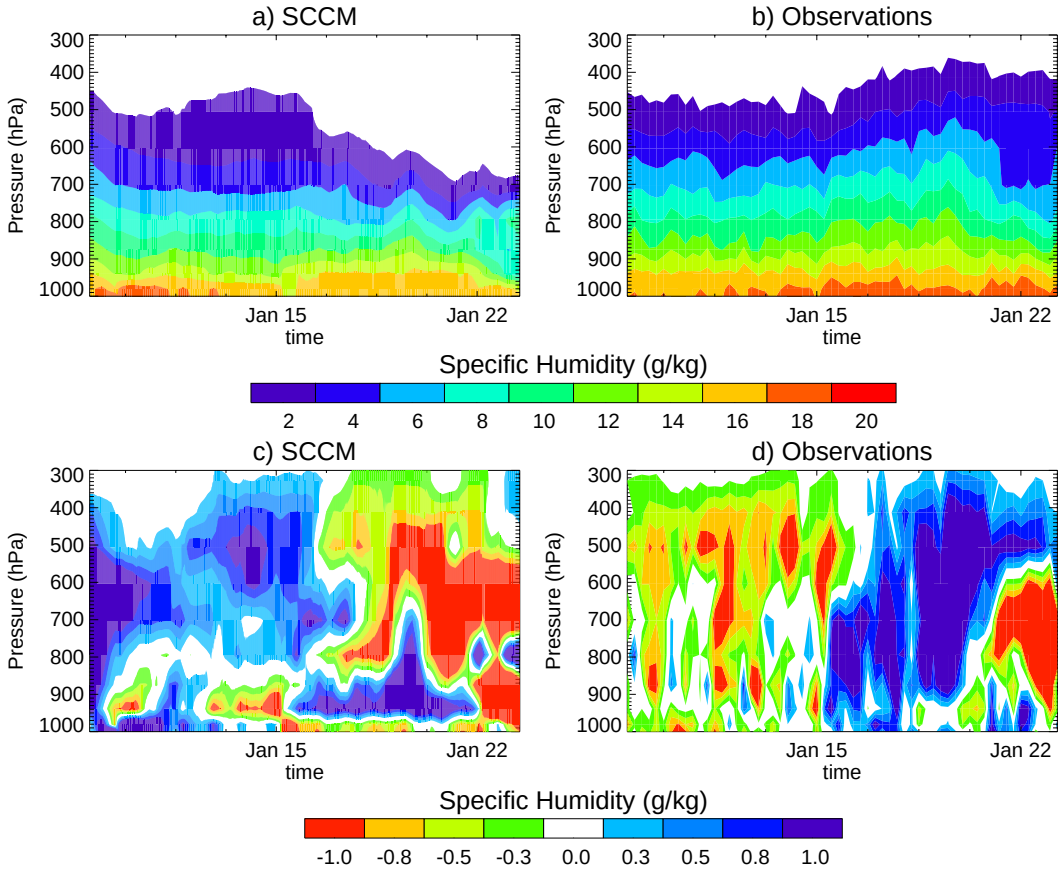

Figure 59: Same as Figure 4.4 but for the second transition event.

of specific humidity, both for absolute values and anomalies, during the simulation for the second transition. Similarly as for the first transition, the specific humidity is underestimated. In this case the low-level moistening is not well simulated, and convection is triggered too quickly compared too the observations, leaving a dry upper troposphere. A shallow moistening is simulated in place where deep convection is seen in the observations. Figure 60 shows the results of the simulation using the Clayson et al (1996) flux scheme. The main difference between both simulations of the second transition is that using the Clayson's scheme the low level moistening and the timing of deep convection are better represented. As in the first transition, two different convective burst instead of sustain deep convection are present in the simulation.

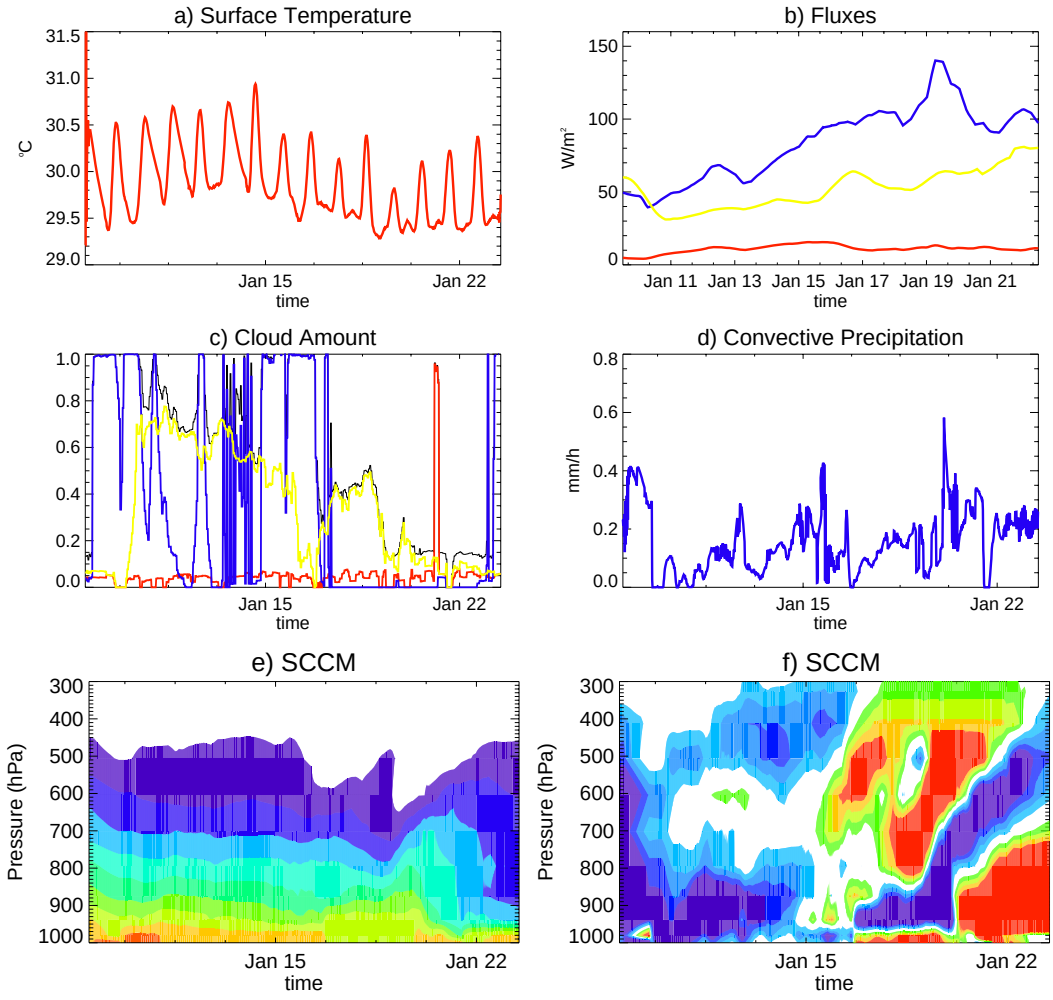

Figure 60: Model simulation corresponding to the second transition period during TOGA-COARE initialized January 8 1993 and using Clayson et al. (1996) surface flux scheme. The panels show a) SST; b) latent heat (blue) and sensible heat (red) fluxes, and net longwave radiation (yellow); c) high (blue), mid-level (red) and low (yellow) cloud fraction; d) convective precipitation e) absolute values of vertical structure of the specific humidity; and d) specific humidity anomalies.

Given the problems of the model with low-level moistening and moist deep convection, it is important to evaluate the impact of changes in magnitude of large-scale forcing surface winds and vertical velocity in the simulation of the transition stages. In this case the model is initialized January 12 1993 (second transition period). Figure 61 show results of the coupled single column model for runs using the observed

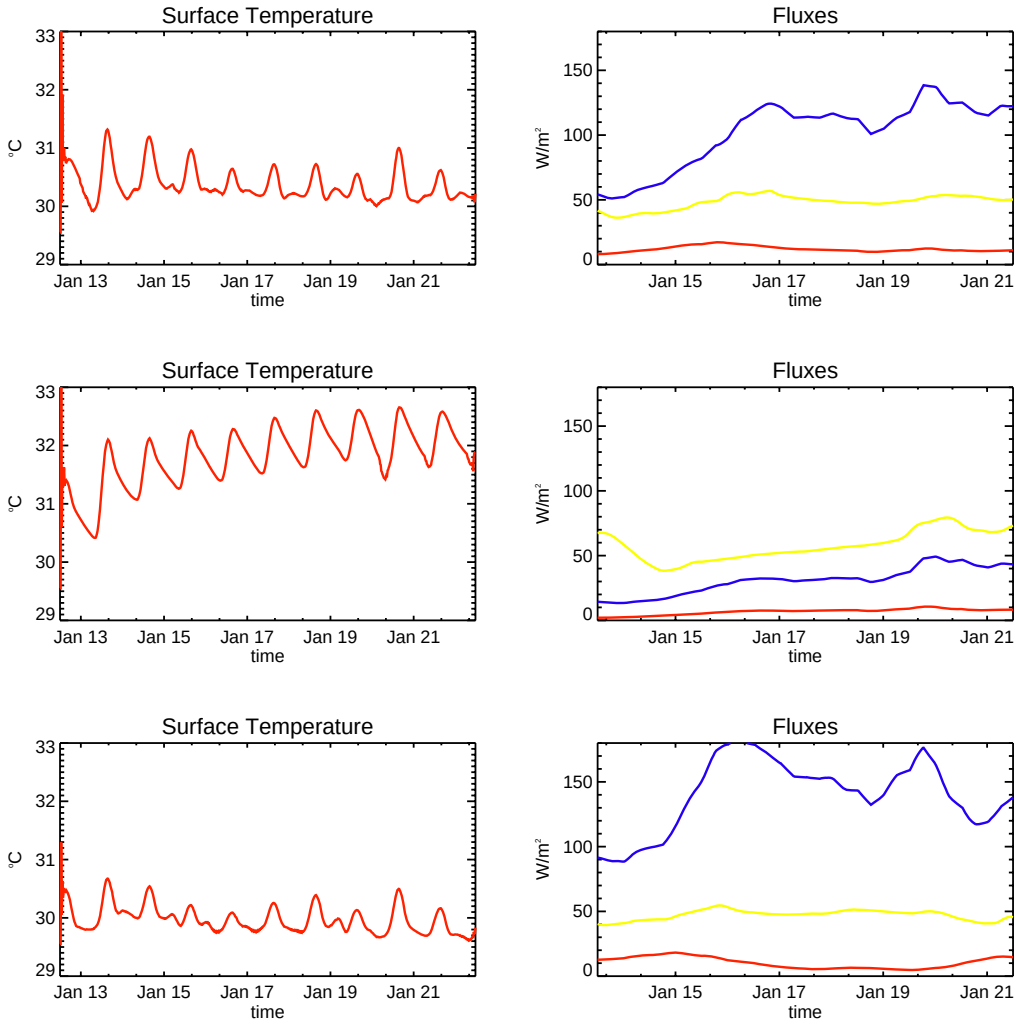

Figure 61: Simulation initialized January 12 1993 during the second transition period using observed surface winds (top panel), one fifth (middle panel) and twice the magnitude of the observed winds (bottom panel).

surface winds (top panel), as well as one fifth (middle panel) and twice the magnitude of the winds (bottom panel). The surface wind modifications are only for surface fluxes computations. The observed changes in latent heat flux and SST are significant. In particular, the evolution of SST for the reduced surface winds does not represent the transition from break to active phases. For doubled wind speed the simulated SST is similar to the observed variability. However, even when the surface

winds are doubled, the atmosphere is still drier than observed and low-level moistening and deep convection are not well simulated. The oceanic temperature profile changes considerably when surface fluxes are modified, with a much warmer (cooler) upper ocean for weaker (stronger) winds as a result of the changes in surface fluxes. An additional test was performed setting to zero the observed vertical velocity. When the observed subsidence is not considered in the simulations cloudiness and rainfall are overestimated compared to the reference run.

In summary, the results showing the sensitivity of the vertical structure of the atmosphere in the simulations to the estimation of the surface fluxes are further evidence of the importance of the local thermodynamical coupling in the evolution of the ISO. In general the coupled SCM handled poorly the slow atmospheric moistening and the extended convective periods due to two major issues: (i) the model appears to be over-convective (convective rainfall is present during the entire simulation period), not allowing the moistening of the atmosphere and the accumulation of convective potential energy, and (ii) the model's parameterization produces convective bursts that, in a GCM, would inhibit the development of long-lived convective events.

CHAPTER V

ROLE OF LOCAL COUPLING IN THE LIFE CYCLE OF THE INTRASEASONAL OSCILLATION

While intraseasonal oscillations (ISOs) are a very important element of the tropical and global climate, numerical models are not able to accurately and consistently simulate their complete life cycle. It was pointed out in previous chapters that one of the main problems of state-of-the-art models and simple atmospheric models to simulate ISO arises from the convective parameterization mainly due to the fact that most schemes tend to be "over-convective". In other words, the evidence suggests that models tend to quickly develop convection from local instabilities rather than slowly build up the energy (CAPE) needed to sustain the kind of extended convective events associated with the observed ISO. One of the consequences of the "over-convection" is that the amplitude of the ISO in the models quickly goes to zero as the integration time increases.

The diagnostic study of the atmospheric and oceanic variability over the Pacific warm pool presented in Chapter 2 suggests that the strong local coupling between the ocean and the atmosphere is essential in the generation of the oscillation with a time scale between 30 and 80 days in this region. Other observational and modeling studies also suggest that the intraseasonal mode originates as a result of air-sea coupling and that considering the coupled ocean-atmosphere processes tends to improve the simulation and predictability of the mode (e.g. Wang and Xie 1998, Waliser et al. 1999, Woolnough et al. 2000, Kemball-Cook et al. 2002, Fu et al. 2003, Inness and Slingo 2003, Fu and Wang 2004, Zheng et al. 2004, Stephens et al. 2004, Wang et al. 2005). However, lack of understanding of the role of local dynamical and

thermodynamical coupling in generating the ISO and the mechanisms controlling the time scale of the oscillation remains.

The strong coupling between the ocean and the atmosphere during the ISO appears to be dominated by the radiation and turbulent fluxes at the surface which are associated with feedbacks between the oceanic mixed layer and atmospheric boundary layer, cloudiness and changes in SST (see Chapter 2). SST is higher during the transition from suppressed to active convection due to the lack of clouds and weak surface winds during the undisturbed phase. Positive anomalies of SST induce a strengthening of the surface winds leading to enhanced evaporation and upper layer mixing. Deep convection follows the positive anomaly of SST. The clouds associated with the convective activity reduce the amount of sunlight reaching the surface, reducing the SST and ending the active phase of convection. Since the evolution of SST appears to play an important role in the lifecycle of the ISO it implies that the depth and dynamics of the ocean mixed layer, which is associated to the rate of change of SST, is also very important for the ISO evolution. In addition the warm pool region is unique in that a large excess of mean precipitation over evaporation and relatively low mean wind speed act to produce a shallow mean mixed layer ($\sim$30m) (e.g., Lukas and Lindstrom 1991). A shallow mixed layer implies that SST will be sensitive to relatively small surface heat flux variations.

From the diagnostic study in Chapter 2 it was found that during the transition phase these surface fluxes (and SST) are highly affected specially due to changes in surface winds and cloudiness. It is hypothesized here that local thermodynamic coupling between the atmosphere and the upper ocean in the tropical western Pacific warm pool controls the life cycle of the intraseasonal oscillation and in particular its time scale. One of the goals of this study is to reproduce the coupled ISO over long integration periods using a model that only includes local mechanisms. In the model we use a very simple atmospheric component without convective parameterization

and where feedbacks with the upper ocean are controlled only by changes in surface winds and cloudiness which together modulate the turbulent and radiation fluxes. It is important to investigate the role of the oceanic mixed layer depth in the behavior of the intraseasonal oscillation obtained with the model. In particular, one of our goals is to evaluate the role of the oceanic mixed layer in determining the time scale of the oscillation.

5.1 Experimental design

In order to study the role of local ocean-atmosphere coupling in generating intraseasonal variability, and the role of the oceanic mixed layer dynamics in determining the time-scale of the resulting oscillation, a semi-empirical one-dimensional coupled model is developed. One advantage of having a simple model is that it permits a full understanding of the main mechanisms that dominate the simulations. Also, we are able to control the modifications introduced in the system in the different sensitivity integrations and changes in the results are easily related and traced back to these modifications. In addition, another advantage of this type of model is that it is very efficient from a computational point of view, allowing long integrations and as many runs as required for its evaluation.

The semi-empirical model consists of a one-dimensional ocean mixed layer model that is driven by an empirically derived atmospheric model whereby surface meteorological and flux variables are related statistically to changes in SST. The ocean component, the same as the one used in Chapter 4, is the one-dimensional second-order closure ocean mixed layer model described by Kantha and Clayson (1994, 2004). The atmospheric component is an empirical scheme designed based on TOGA/COARE data, as well as daily data of NOAA OLR, surface fluxes from the International Satellite Cloud Climatology Project (ISCCP) and TMI SST.

The atmospheric model is designed to provide, at every time step, the required

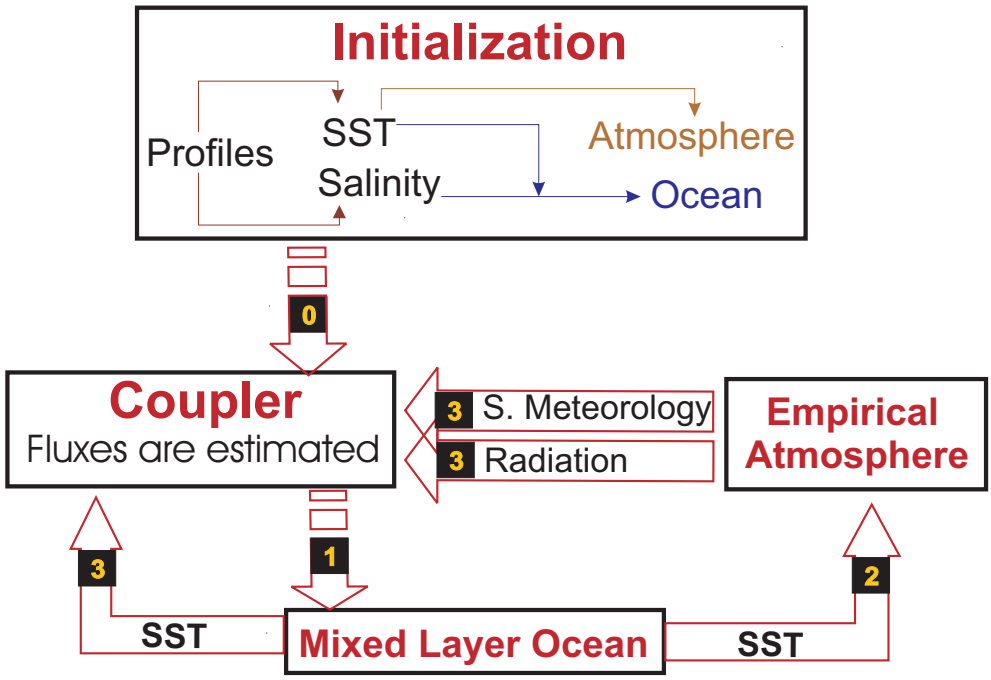

Figure 62: Schematic diagram of the initialization and one cycle of the semi-empirical model.

"input" variables to the ocean component in order to compute the fluxes needed for the ocean surface heat and moisture budget used to drive the ocean model. The approach is to build an empirical atmosphere that could be easily coupled with the oceanic mixed layer model and responds to local changes of SST. In order to do that, a set of empirical relationships were constructed between time series of local SST and different atmospheric variables that are needed by the ocean mixed layer model at every time step. The variables required to calculate the turbulent and radiation fluxes needed by the ocean model and are to be provided by the atmospheric model at every time step are: surface wind speed, specific humidity, air temperature, precipitation, surface pressure, downward long wave and solar radiation at the surface.

Figure 62 shows a schematic diagram of the model's implementation. In step 0, the model is initialized in a particular Julian day with predefined temperature and salinity profiles throughout the entire ocean depth. Using the initial value of SST,

the atmosphere is initialized using a set of empirical diagnostic equations. The radiation scheme is also initialized using SST and the estimated OLR using the diagnostic equations. At this stage, all the oceanic, atmospheric and radiation estimates are transmitted to the coupler. In step 1, turbulent fluxes are estimated using a bulk approximation scheme (Gill 1982). Surface radiation and turbulent fluxes as well as surface wind speed and precipitation rate are transmitted to the ocean model. Surface pressure, only used to estimate the saturation mixing ration in the surface, was assumed to be constant (1010 hPa). By doing this, if the maximum error in surface pressure is assumed to be less than 10 hPa, which is a large error in the tropics, the error in the estimation of the saturation mixing ratio is less that 1%. In step 2, a new set of temperature and salinity profiles are estimated using the second-order closure mixed layer ocean model and the updated SST is transmitted to the atmospheric component. In step 3, the empirical atmosphere is updated using the new SST computed by the ocean model. In addition, solar and long wave radiation at the surface are computed using SST and the updated OLR. The updated surface meteorology (surface winds, specific humidity, air temperature, precipitation), the radiation fluxes and the current SST are transmitted to the coupler. At this stage, steps 1 to 3 are repeated for every time step to obtain the entire simulation. The vertical resolution of the ocean model was set to 1m and the time step to 15 minutes. Sensitivity experiments were performed using different vertical resolutions and different time steps. Results and conclusions were not sensitive to the different temporal or spatial resolutions within a reasonable range.

As mentioned before (Chapter 4), horizontal advection, although sometimes locally large (e.g. Feng et al. 2000), plays a minimal role in governing the broad scale SST anomalies produced by the ISO in the heart of the Warm Pool. For this reason, as well as to conserve the simplicity of the coupled model, no advection was included in the ocean model.

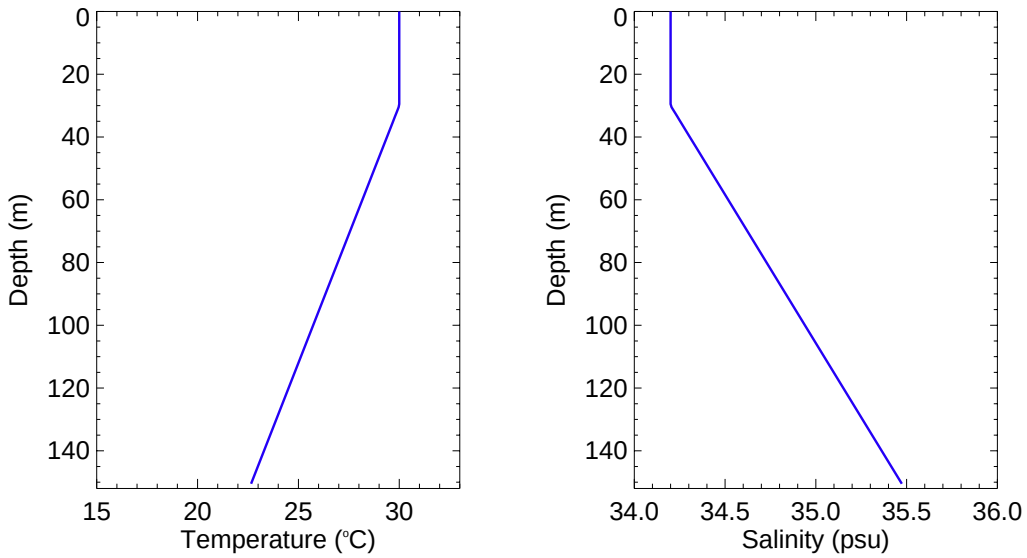

Figure 63: Typical SST and salinity profiles in the West Pacific used to initialize the model.

The model was integrated for 3500 days and the initial conditions correspond to a typical SST and salinity profiles in the West Pacific warm pool. Figure 63 shows both profiles for the first 150m which correspond to the total ocean depth in which the model is integrated (depth of the "active ocean").

5.2 Derivation of the Atmospheric Component

All the empirical relationships derived for the atmospheric component were constructed using unfiltered 3-hourly and daily data depending on the specific relationship. The use of unfiltered data guarantees that no preferred time scales of variability are imposed to the model's evolution. Any resultant oscillation in the simulations is then a product of the coupled mechanisms represented in the model and not a result of any kind of artificial forcing within the set of empirical relationships.

Empirical diagnostic equations were constructed for all the variables except for surface winds and cloudiness in which prognostic equations were used. Cloudiness in the model is directly represented by the magnitude of OLR. Empirical diagnostic equations are statistically constructed relationships that directly link the values of

SST with the values of a particular atmospheric variable, simultaneously (same time, same day). Empirical prognostic equations on the other hand are statistically derived relationships between SST and changes or tendencies of a particular atmospheric variable. The equations predict the values of the atmospheric variables for the next time step of the integration. By using prognostic equations there is a possibility for the existence of negative feedbacks in the system. This allows us to test the local coupling hypothesis presented before.

It is important to note that the goal of the empirical system is to represent the average local response of the atmosphere to changes of SST. One of the direct consequences of this construction is that all atmospheric variability that does not result from local coupling with the ocean would not be represented by the one-dimensional coupled model. In other words, since the relationships used to construct the atmospheric system were estimated between local (regional) SST and the collocated variables, atmospheric variability introduced by teleconnections or large-scale circulations is not included in the model. Along the same lines, it is clear that oceanic and atmospheric variability results from local and non-local phenomena. For example, in the Pacific Ocean the depth of the thermocline in a particular ocean column can be a direct result of the strength of the surface winds on top of the column as well as a consequence of basin wide phenomena like ENSO, among others. Since our goal is to study the role of local thermodynamic coupling in the generation of ISO, the set of empirical equations should only represent the direct local association between SST and the different atmospheric variables and not the non-local effects.

5.2.1 Empirical relationships

The general procedure used to obtain the set of empirical relationships for surface air temperature and specific humidity is as follows. Basic features of the joint histogram between SST and each variable were considered. Specifically, the relationships were

constructed between pre-defined SST values that represent the center of different SST intervals (e.g. bins of SST) and the median of the atmospheric variable within each SST bin as given by the joint histogram. In other words, SST, which is the independent variable, is first divided in different bins of certain size in order to span the range of variability in the region. A total of twelve SST bins of 0.2°C starting at 28.3°C (center of the bin) were used. For each of the intervals of SST, the median of the atmospheric variable was found. Finally, the twelve pairs are used to estimate an empirical relationship between the two variables. All relationships were estimated using common regression analysis tools (e.g. least squares). This procedure guarantees the relationships effectively represent the local average response of the atmosphere to local (changes of) SST.

The SST data set used to construct the empirical relationships with specific humidity and air temperature as well the values for these two variables correspond to the 3-hourly TOGA COARE data set (November 1992 to February 1993, Curry et al 1999). Figure 64 (65) show the time series of surface air temperature (surface air specific humidity) during TOGA COARE, the scatter plot of SST and surface air temperature (specific humidity) and the relationship between the surface air temperature (specific humidity) and SST in the intervals selected. Following the technique described before, SST was divided in selected intervals. The red and green lines represent the behavior of the mean and the median of the surface air temperature (specific humidity) in each interval respectively. The blue lines correspond to the mean plus and minus one standard deviation of the variable in each SST interval. The scatter plot of SST and surface air temperature suggests the existence of a linear relationship between both variables in the region, as expected. For specific humidity, the relationship appears to be quadratic. The respective relationships equations for SST-surface air temperature and SST-surface air specific humidity are: $SAT = 0.54SST + 12.21$ (both variables in °C) where SAT stands for surface air

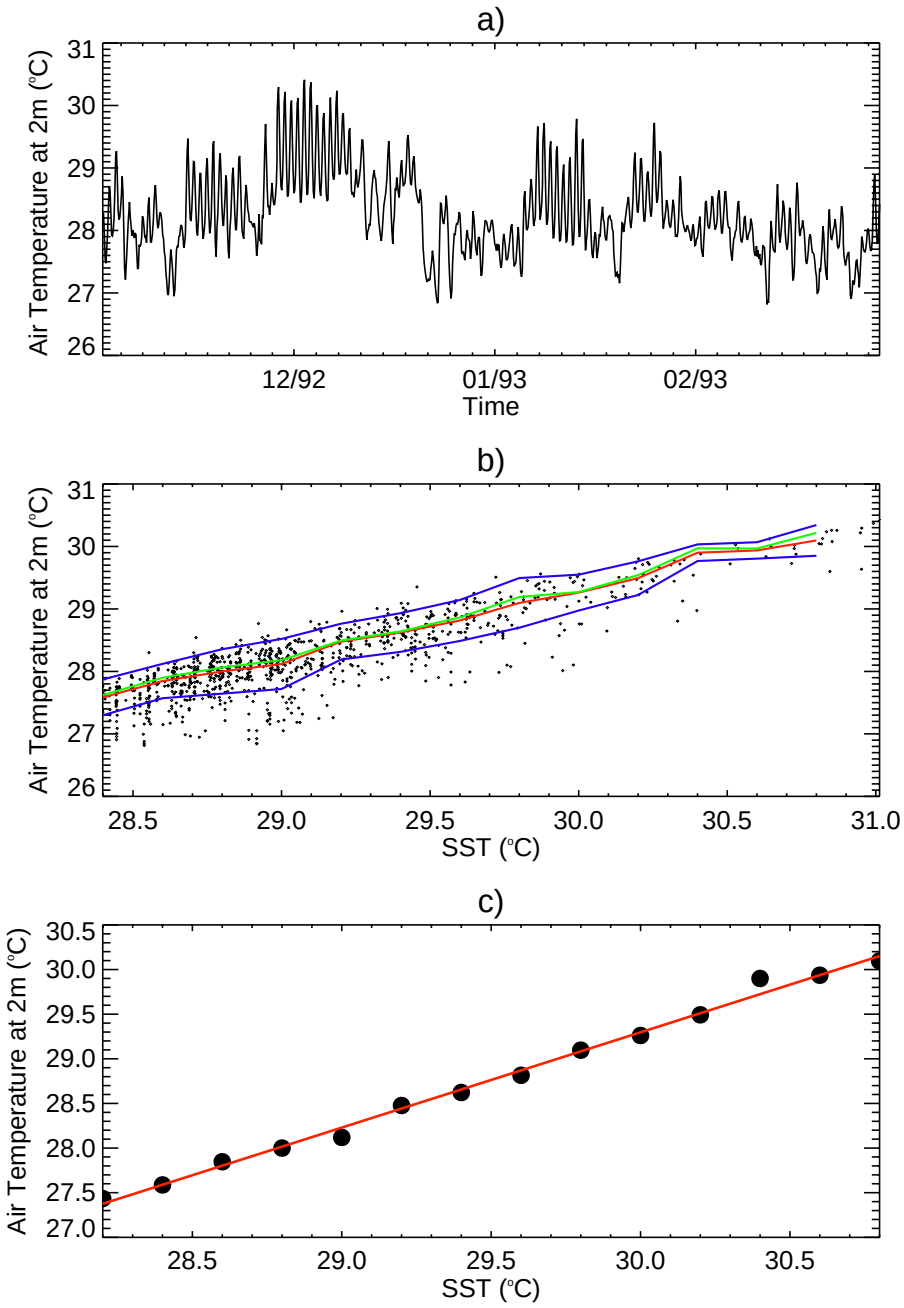

Figure 64: a) Time series of surface air temperature; b) Scatter plot of SST and air temperature: Red and green lines represent the behavior of the mean and the median of the surface air temperature. Blue lines correspond to the mean plus and minus one standard deviation; c) Scatter plot of mean air temperature and SST in each interval (black circles) and the estimated linear relationship ($SAT = 0.54SST + 12.21$) between both variables (red line). Air temperature data from TOGA-COARE.

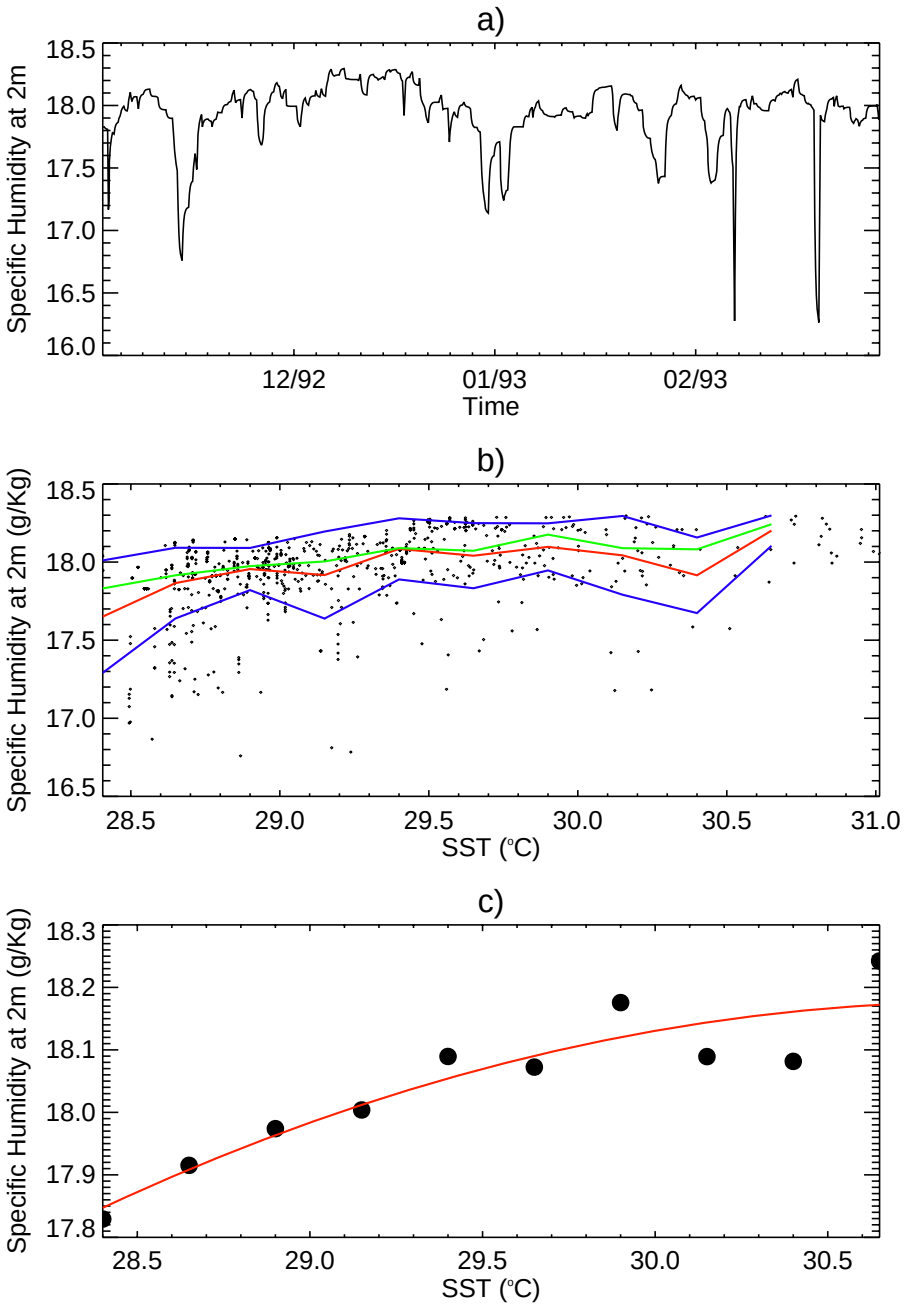

Figure 65: Same as Figure 64 but for specific humidity at 2m ($SHum = -5 \times 10^{-2} SST^2 + 3.1 SST - 29.85$, $SHum = 18.2$ g/kg for $SST > 30.6$)

temperature, and $SHum = -5 \times 10^{-2} SST^2 + 3.1 SST - 29.85$ where $SHum$ stand for specific humidity and is in g/kg. When $SST > 30.6$, the specific humidity is specified to be a constant value $SHum = 18.2$ g/kg. The equations account for 90.6% (r=0.952) and 71.3% (r=0.844) of the variance of surface air temperature and specific

humidity among the intervals selected, respectively.

5.2.2 Empirical Prognostic Relationships

In order to include feedback mechanisms between the ocean and the atmosphere, prognostic equations of the most relevant variables involved in the local ISO component were incorporated. The main processes considered are the changes in surface radiative and turbulent fluxes which in turn are controlled mainly by changes of convection, represented by OLR, and the changes of surface wind speed, both relative to SST. Chapter 2 shows evidence that the variability of OLR and surface winds relative to SST and vice versa is very important to understand the life cycle of the ISO. The goal of this section is to find relationships for the locally induced tendencies of OLR and surface wind speed that are driven by SST.

One of the most important changes in the atmosphere due to the intraseasonal oscillation is the change in cloudiness; in nature this has an impact in the latent heating and radiative forcing within the atmospheric column as well as at the surface. Deep convective clouds form in the active phase of the ISO introducing negative anomalies of outgoing long wave radiation (OLR) at the top of the atmosphere. It is for this reason that one of the most essential components in the empirical atmosphere is the relationship between SST and OLR. This relationship is key because it summarizes several complex physical processes that are related to formation of deep convective clouds due to local changes in the surface forcing that, in most models, are accounted for by the use convective and cloud parameterizations, or in more recently years, by the use of cloud resolving models.

Most of the atmospheric and oceanic variables in the western Pacific warm pool show evidence of interannual variability as well as long-term tendencies. It is important to emphasize at this point that while the ISO itself presents interannual changes in both magnitude and frequency, it is a ubiquitous feature of the western Pacific

warm pool, in particular during boreal winter. Interannual variability controlled by other phenomena like ENSO and long-term trends act to change the background state of the coupled system. Such changes of background state are not arising from local interaction, but are regionally and globally induced. Since the background state changes due to large-scale phenomena, the local relationship between SST and OLR tendencies will depend on such changes. Given that our goal in this chapter is to study the local ISO mechanism, a different approach was followed to exclude the effects of both the annual cycle and interannual variability in the region.

The best approach to exclude the effects of interannual variability is to use high resolution data from a field experiment during an intraseasaonal event as it was the case during TOGA COARE IOP. Unfortunately, there is no high resolution OLR data available during TOGA COARE. For this reason, the SST-OLR prognostic relationship was constructed using the daily NOAA interpolated OLR and daily SST. The region considered to construct the relationship corresponds approximately to the Equatorial Western Pacific Warm Pool and is defined by the following boundaries: 10°S to 5°N, 155 to 175°E. Since OLR data is only available in a daily temporal scale the SST data used for this relationship corresponds to the daily SST data from Tropical Rainfall Measuring Mission (TRMM) satellite Microwave Imager (TMI) measurements retrievals, with a spatial resolution of 0.25 degrees from 40°S to 40°N (available at `www.ssmi.com/tmi/tmi_description.html`). The TMI SST data set is suitable for studies of subseasonal variability since it is derived from microwave-based measurements, which is virtually unaffected by cloud coverage allowing reliable measurements of SST variability during the entire life cycle of the ISO. Figure 66 shows the time series of SST in the region selected as well as its geographical localization and its average wavelet spectrum. In addition to a marked annual cycle, the SST in the region presents considerable subseasonal variability including a spectral peak between 25 and 80 days. Figure 66 also shows an increase of SST in the region during the last

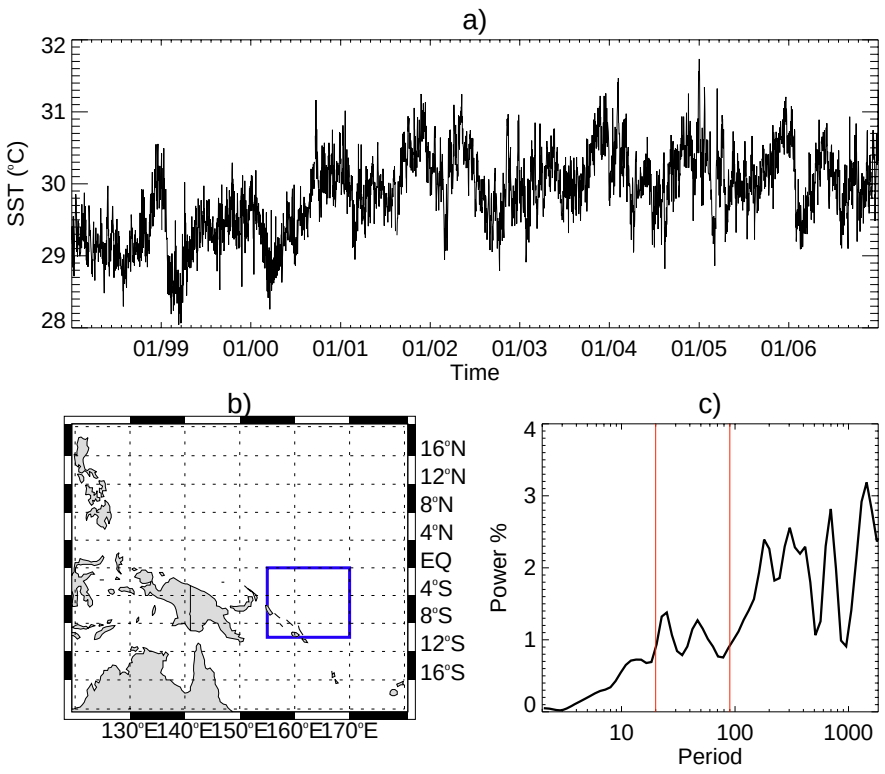

Figure 66: a) Time series of TMI SST in the selected region (10°S to 5°N, 155 to 175°E); b) Geographical reference of the region considered to estimate the empirical relationships (blue box) and c) average wavelet spectrum of the SST time series.

decade that matches well with results obtained by Agudelo and Curry (2004). The SST-OLR relationship was calculated using data for the period from 1998 to 2006.

To avoid potential errors in the estimation of the relationship introduced mainly by the upward trend in SST in the region, the relationship was constructed using unfiltered data from periods of intraseasonal variability during winter. The first step was to identify intraseasonal events for the period 1998-2006 during an extended winter season (NDJFM). The events were identified using filtered OLR in the 25-80 day band. ISO events were selected to correspond to OLR minima in the intraseasonal band with an absolute magnitude greater than one standard deviation. A total of 14 events were selected. For each of the events, the relationship between SST(t) and the OLR tendency (ΔOLR) given by $OLR(t+1) - OLR(t)$ was studied by considering

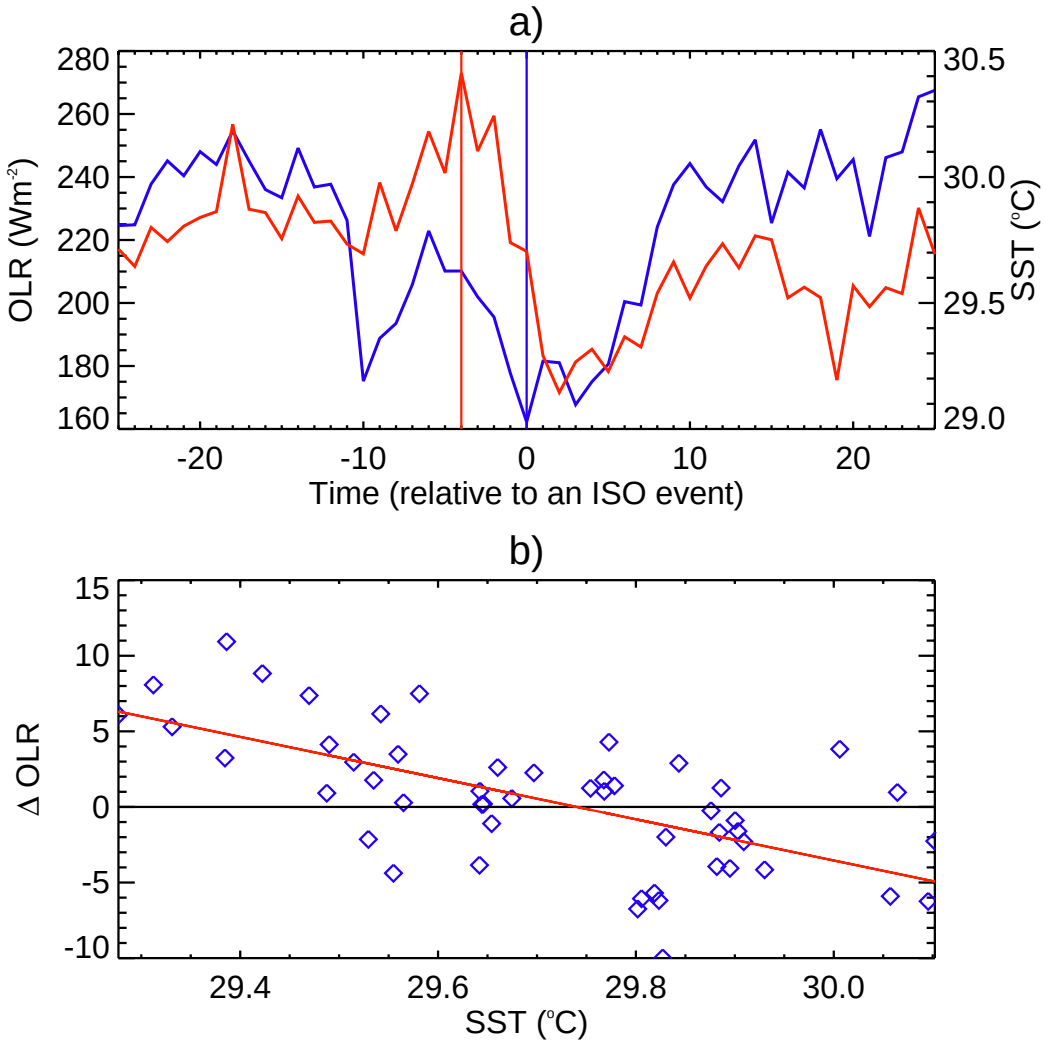

Figure 67: a) Evolution of SST (red line) and OLR (blue line) during one of the selected intraseasonal events. Vertical lines mark the maximum of SST and the minimum of OLR values during the ISO event; b) Estimated relationship between SST and OLR tendency (OLR(t+1)-OLR(t)) for the selected ISO event.

25 days before and after the maximum of convection (a total of 50 days for each event). Figure 67a shows an example of the SST (red line) and OLR (blue line) evolution during one of the selected intraseasonal events. Vertical lines mark the maximum of SST and the minimum of OLR during the ISO event. Consistent with findings using TOGA COARE data (Chapter 2), SST reaches the maximum value during the transition from suppressed to active convection (i.e. from maximum to

minimum OLR). The example shows the coupling between SST and convection in the intraseasonal time scale. In addition to the ISO, the OLR shows an oscillation with a higher frequency. It is also clear from the weak SST variability in the higher frequency band that the coupling in this spectral range is not as strong as during the ISO. This suggests that the higher frequency variability in OLR is not locally induced by coupled processes. Figure 67b shows the relationship between SST and OLR tendency for the same ISO event. The diagram suggests that for values of $SST > 29.72$ °C the tendency of OLR is to decrease.

A similar relationship is observed for the other 13 ISO events selected. The main difference between the events is the threshold of SST that determines the sign of the OLR tendency (29.72 °C in the previous example), ranging from 29.25°C to 30.2°C. As it was explained before, this difference is due to the variability of the background state of the coupled system (long-term trends and interannual variability) which acts as the reference point for the intraseasonal anomalies. In other words, SST variability introduced by the ISO corresponds to anomalies around the slow changing background state. Since we are interested in the average behavior of the coupled system during an ISO event, all the events were combined in a single scatter plot by subtracting the mean SST of each individual event and adding the mean SST of all events. Figure 68 shows the combined scatter plot for the 14 selected ISO events as well as the estimated relationship to be used in the empirical atmosphere which is given by $\Delta OLR = 258.23 - 8.68SST$ (r=0.51 for all the 1450 data points) where ΔOLR is the 24-hour OLR tendency in Wm^{-2} and SST in °C.

To estimate an empirical prognostic relationship for surface wind speed, hourly surface winds and SST data from TOGA COARE were available. The first step was to calculate the difference between the value of surface wind speed at certain time of the day and the value at the same time on the previous day. This was calculated for each of the 24 hours. In this manner the effects of the diurnal cycle, which is clearly

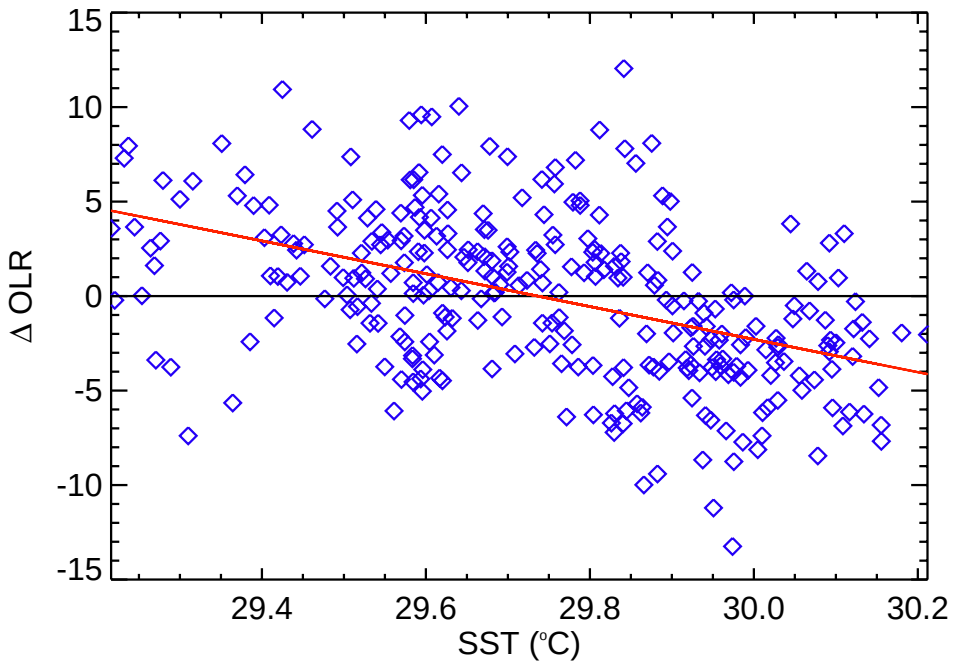

Figure 68: Scatter plot of SST and OLR tendency for the 14 selected ISO events. Red line represents the estimated relationship ($\Delta OLR = 258.23 - 8.68SST$)

not a result of local coupling but of solar forcing, are excluded from the prognostic relationship. The diurnal cycle, which appears to play an important in the observed ISO (Webster et al. 1997), is taken into account by including a realistic diurnal solar forcing as will be explained in the next section. A single prognostic relationship was obtained using all the tendencies or differences calculated for every hour. The scatter plot between both magnitudes (Figure 69a) suggests the existence of a linear relationship in which, in average, positive tendencies of surface wind speed are induced for values of SST greater than ∼29.4 °C. The red, green and blue lines represent the average, median and standard deviation (around the mean) of surface wind speed tendencies for each of the selected SST intervals, respectively. The amount of data for SST greater than 30.4 °C was not enough to be used in the estimation of the statistical relationship; however, it is clear from the Figure 69a that the use of these points will only strengthen the empirical relationship obtained. Figure 69b is a zoom of Figure 69a only considering values of SST smaller than 30.4 °C. Figure 69c shows

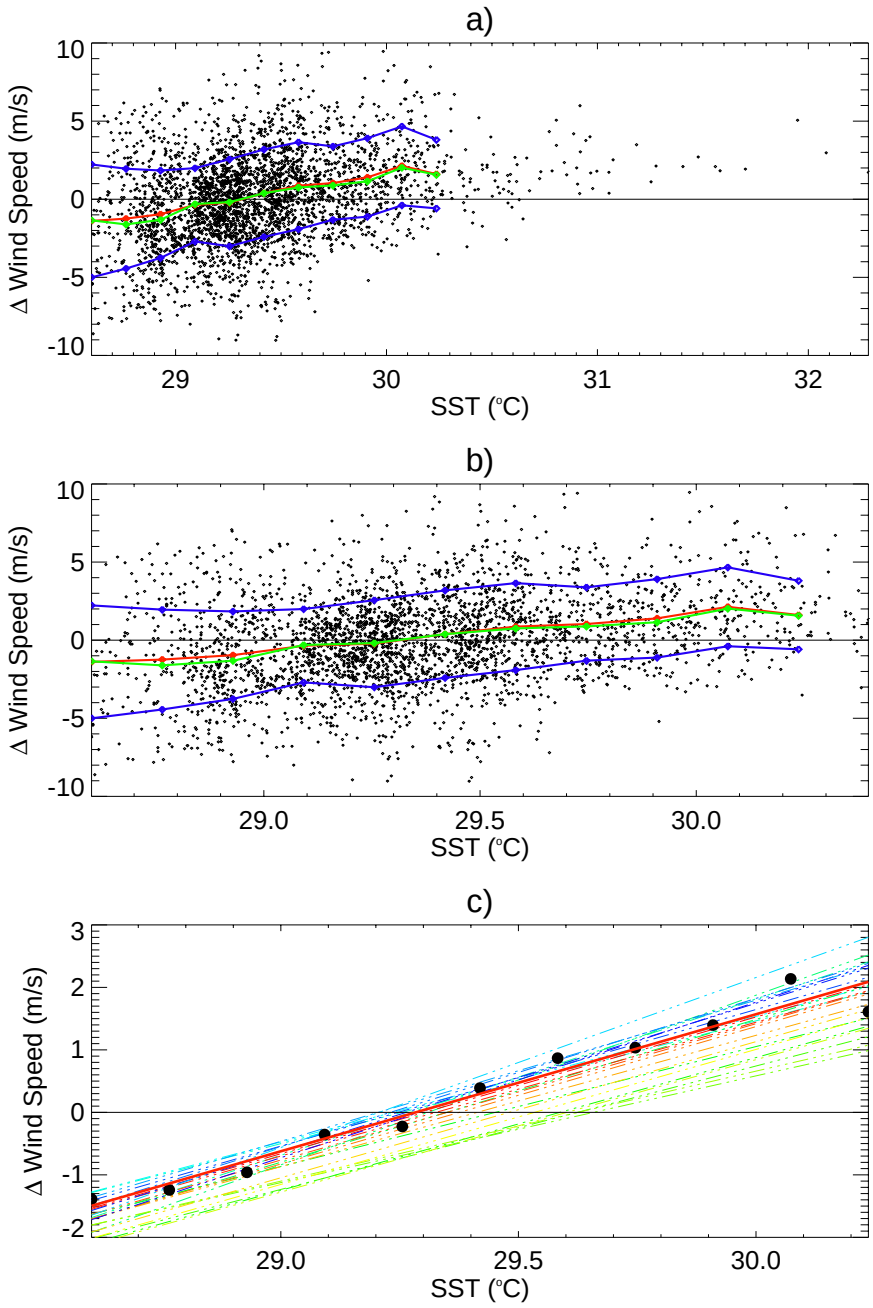

Figure 69: a) Scatter plot of SST and surface wind speed tendency; b) zoom of a) for SST values smaller than 30.4 C; c) Scatter plot of mean surface wind speed tendency and SST in each interval (black circles) and the estimated linear relationship ($\Delta SWS = 2.2SST - 64.23$) between both variables (red line). 24 different colored dashed lines represent the relationship for each hour of the day. Blue colors correspond to hours before sunrise (local time), green colors to mid afternoon hours (around 4 pm local time).

the SST and wind speed tendencies for each interval (black circles) as well as the estimated linear relationship (red line) given by $\Delta SWS = 2.2SST - 64.23$ (r=0.97 for the SST intervals selected) where ΔSWS is the 24-hour tendency in ms-1 and SST is in °C. The twenty four different dashed lines represent the relationship for each hour of the day. Their similar behavior and small spread suggest that daily tendency of surface wind speed given by SST is similar during the entire diurnal cycle.

In summary, the prognostic relationships considered for the empirical atmosphere suggest that as SST increase (decrease) above certain threshold, OLR tends to decrease (increase) and surface wind speed tends to increase (decrease). Both relationships, which agree with the evidence presented in Chapter 2, introduce negative feedbacks in the coupled system by changing the surface fluxes: When SST is high; positive anomalies of wind speed are introduced in the system cooling down the ocean by mixing and evaporation (increased latent heat flux). Similarly, when SST is high, negative anomalies of OLR are introduced in the system reducing the amount of solar radiation reaching the ocean, which in turns results in negative anomalies of SST. The combination of the solar forcing and the negative dynamic and thermodynamic feedbacks could potentially result in a coupled oscillation in the model. If this is the case, the time scale of the oscillation would not be artificially imposed by approach followed to estimate the empirical relationships, but by the nature of coupling between the ocean and the atmosphere represented in the model.

In order to obtain an empirical relationship for precipitation, we followed the same approach used to construct the diagnostic relationships (e.g. SST-surface air temperature) but in this case the two variables considered were OLR and precipitation. In the tropics, OLR is a very good proxy for deep convection, which is the dominant source of rainfall in the west Pacific warm pool. Daily NOAA interpolated OLR and daily rainfall from the merged precipitation analysis of the Global Precipitation Climatology Project (GPCP) for the period 1998-2006 were used. Since the OLR is

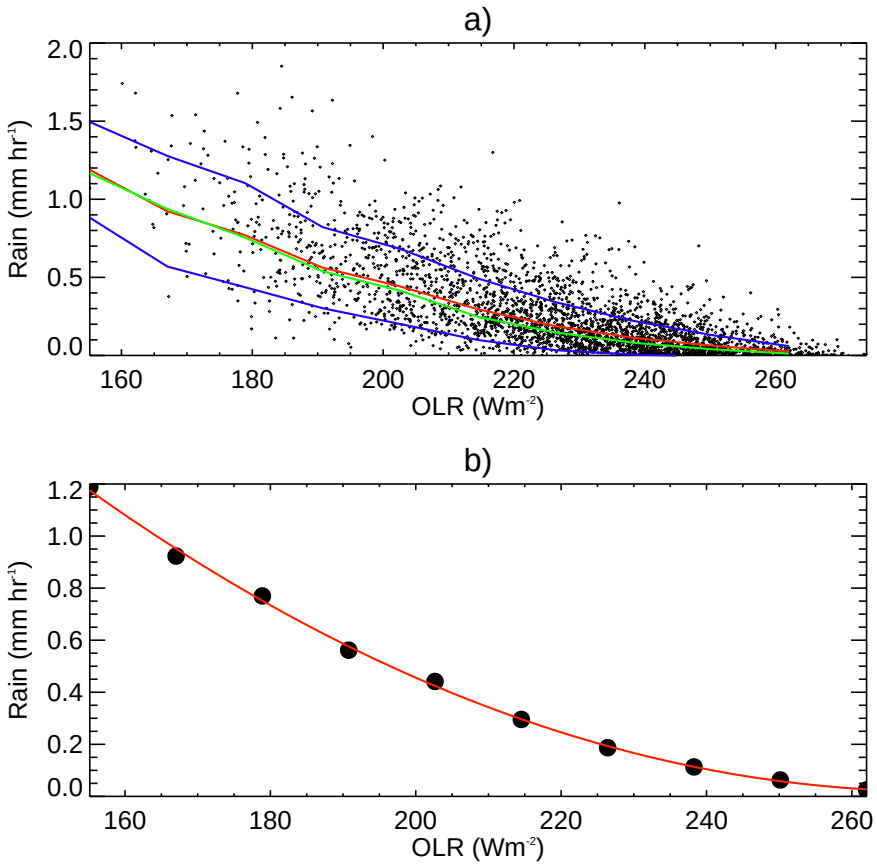

Figure 70: a) Scatter plot of OLR and rainfall in the warm pool: Red and green lines represent the behavior of the mean and the median of rainfall. Blue lines correspond to the mean plus and minus one standard deviation b) Scatter plot of OLR and rainfall in each interval (black circles) and the estimated linear relationship ($PPT = 8.53 \times 10^{-5} OLR - 0.046 OLR + 6.31$) between both variables (red line).

related to the SST, precipitation is indirectly controlled in the model by SST values. Figure 70 shows the scatter plot of OLR and rainfall in the warm pool as well as the relationship estimated between both variables in the selected OLR intervals (ten equally-spaced intervals from 150 to 260 Wm^{-2}). The resulting relationship is given by the quadratic equation $PPT = 8.53 \times 10^{-5} OLR - 0.046 OLR + 6.31$ (r=0.99 for the ten intervals selected), where PPT is the precipitation in mm/hr and OLR is in Wm^{-2}. PPT was set to zero for $OLR > 220$ Wm^{-2}.

5.2.3 Radiative Component

The radiative processes in the model are represented by a simple semi-empirical scheme designed to estimate the solar and long wave (greenhouse effect) radiation that reaches the surface of the ocean as well as the long wave radiation emitted at the surface of the ocean. The radiative scheme is based on astronomical and empirically derived relationships.

The solar radiation flux at the top of the atmosphere was computed at every time step of the model based on astronomical approximations. The amount of solar radiation incident on the top of the atmosphere depends on the latitude (which is an input for the model), season and time of the day which together determine the astronomical geometric factors that describe the solar input. In general, the solar flux per unit surface area could be written as

$$Q = S_0(\frac{\bar{d}^2}{d}\cos\theta_s) \tag{1}$$

where S_0 is the solar constant (1367 Wm^{-2}), $\bar{d}$ is the mean distance for which S_0 is measured, d is the actual distance from the sun, and θ_s is the solar zenith angle. In the model we use a Fourier series formula for the $(\bar{d}/d)^2$ derived by Spencer (1971) as a function of the Julian day. The solar zenith angle is the angle between the local normal to Earth's surface and the line between a point on Earth's surface and the sun and it depends on latitude, season (declination angle) and time of the day (hour angle; 0 degrees at noon local time). The declination angle was also obtained from a formula by Spencer (1971).

Once the top of the atmosphere insolation is calculated, the surface shortwave radiation flux is estimated using an empirical relationship of average diurnal net surface insolation and OLR derived by Shinoda et al. (1998). The relationship allow us to predict the 24-hour-average surface insolation from OLR and is based on linear regression of OLR onto biased adjusted surface radiation time series in the 0N-10S,

60E-180 domain, which encompasses the warm pool region, and are derived from the Surface Radiation Budget project (Whitlock et al., 1995). The following is the regression relation used: $Qs = 0.93OLR - 1.03$, where Qs is the net surface insolation in Wm^{-2}, and OLR is Wm^{-2}. This empirical formula based on OLR appears to be superior to the insolation from NCEP reanalyses (Shinoda et al. 1998).

Since we need net surface insolation at a temporal resolution higher than daily, a further step is needed. In order to correct the solar radiation at every time step, the following procedure is followed: (i) The solar input at the top of the atmosphere is calculated for the specific time of the day determined by the step of the model, (ii) The 24-hour-average solar input at the top of the atmosphere is also calculated; (iii) the OLR obtained in the atmospheric model is used to calculate the 24-hour-average net surface insolation using Shinoda et al (1998) relationship; (iv) the top of the atmosphere insolation from (ii) and the surface shortwave flux estimated from (iii) are then used to obtain a correction factor or albedo; and (v) the albedo is then used to convert the solar input obtained in (i) for the top of the atmosphere to net surface insolation at a specific time of the day. This procedure is followed in order to include a realistic solar forcing at the surface that has a diurnal cycle with its magnitude modulated by convection.

The surface net long-wave radiation depends on the difference between the emitted long-wave radiation from the surface and the downward radiation received at the surface due to the greenhouse effect. The long-wave (ULW) radiation emitted from the surface was estimated according to the Stephan-Boltzmann equation, $ULW = \varepsilon\sigma SST^4$, where ULW is in Wm^{-2}, and SST in degrees Kelvin. In the previous equation, σ is 5.67 x 10^{-8} Wm^{-2} K^{-4}, and ε is the emissivity of the surface to account for deviations from a theoretical black body. For the ocean surface we used a constant value $\varepsilon = 0.985$.

In general, the downward long-wave radiation strongly depends on the amount

of greenhouse gases in the atmosphere and clouds. Hence variations in convection associated with ISO introduce changes in the downward long-wave radiation. In order to account for those changes, an empirical relationship between OLR, which is a proxy for convection, and downward long-wave radiation (DLWR) flux at the surface from the ISCCP was constructed following the same approach as in the empirical diagnostic relationships. Figure 71 shows the ISCCP DLWR, the scatter plot of OLR and DLWR and the statistical relationship which is given by $DLWR = 1.7 \times 10^{-3}OLR - 0.6OLR - 377.26$ (r=0.99 for the ten OLR intervals selected), with DLWR and OLR in Wm^{-2}. The negative sign indicates the downward direction of the flux. In this case low (high) values of OLR are associated with high (low) absolute values of downward long-wave radiation. In other words, positive anomalies of "cloudiness" result in positive anomalies of downward long-wave radiation, as expected.

If the semi-empirical ocean-atmosphere model is run using only diagnostic equations, even for OLR and surface wind speed, the model reaches stability after approximately 2600 days of integrations following a rapid increase of temperature. Results of the integrations do not show an internal oscillation in the coupled system. SST asymptotically increases until near-stabilization around an unrealistically high value because the lack of mechanisms (negative feedbacks) to cool down the ocean (Figure 72), giving no chance to the development of any kind of oscillation. In this case the system converges to a state of permanent quiescent or suppressed phase. In summary, without the negative feedbacks it is not possible for the system to converge to an oscillation. Similar results are obtained for other variables like is the case of OLR and surface winds in which no oscillation is present and the model also reaches stability after approximately 2600 days. In this diagnostic case, the resulting equilibrium temperature is determined by a balance between incoming solar radiation, upper ocean mixing processes and evaporation which are primarily determined by the equilibrium OLR and surface wind speed respectively. Even though this result was expected, it

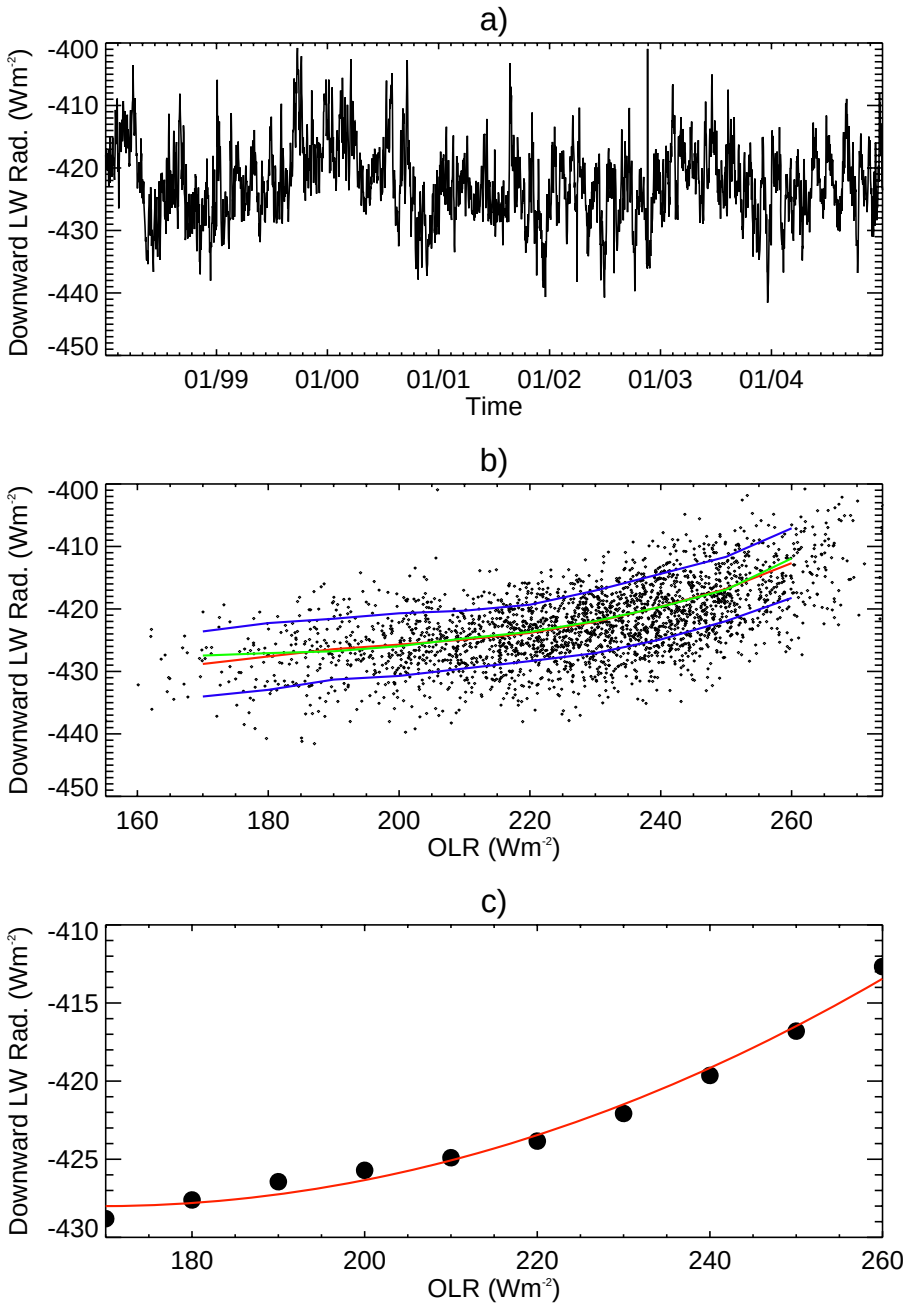

Figure 71: Same as Figure 64 but for OLR and downward long-wave radiation ($DLWR = 1.7 \times 10^{-3} OLR - 0.6 OLR - 377.26$).

is important to show that the model does not have an inherent oscillation if negative feedbacks between the atmosphere and the ocean do not exist.

In the second set of experiments, the OLR and surface wind speed prognostic equations were included in the model. In this case, the model does not estimate

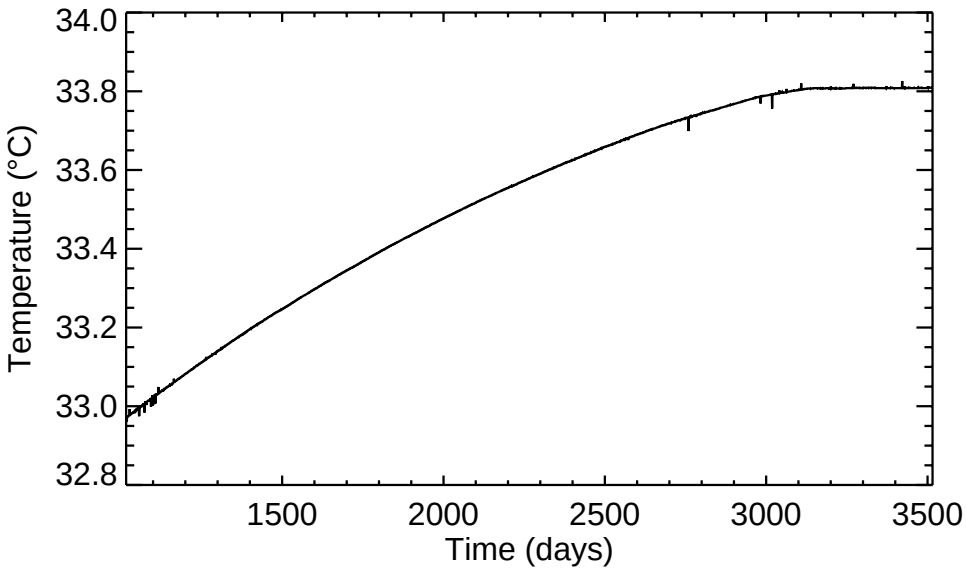

Figure 72: Model results for daily SST obtained using only diagnostic equations.

the absolute value of these two variables but it estimates their tendency for the next time step. Both prognostic equations introduce feedbacks between the ocean and the atmosphere that results in a remarkable broad-band intraseasonal spectral peak evident from the integrations. Different from the fully diagnostic model, the prognostic model converge to a quasi-periodic oscillation. Figure 73 and Figure 74 show the time series of surface wind speed and OLR generated by the prognostic coupled model for last 1000 days of integration, as well as their Fourier spectrum revealing the robust intraseasonal peak. The feedback mechanism between SST and surface wind speed in the intraseasonal band is summarized by the phase diagram between the intraseasonally filtered (25-80 days) SST and surface wind speed simulated by the model as shown in Figure 75. The mutual response between the two variables is similar to observations during TOGA COARE as shown in Figure 9.

If observations are compared to the model output, it is possible to see that the spectral peak in the intraseasonal band in the simulated OLR (Figure 74) is very similar to the spectrum obtained using observations (Figure 76). In both cases most of the OLR variability is contained in the intraseasonal band and the relative amount

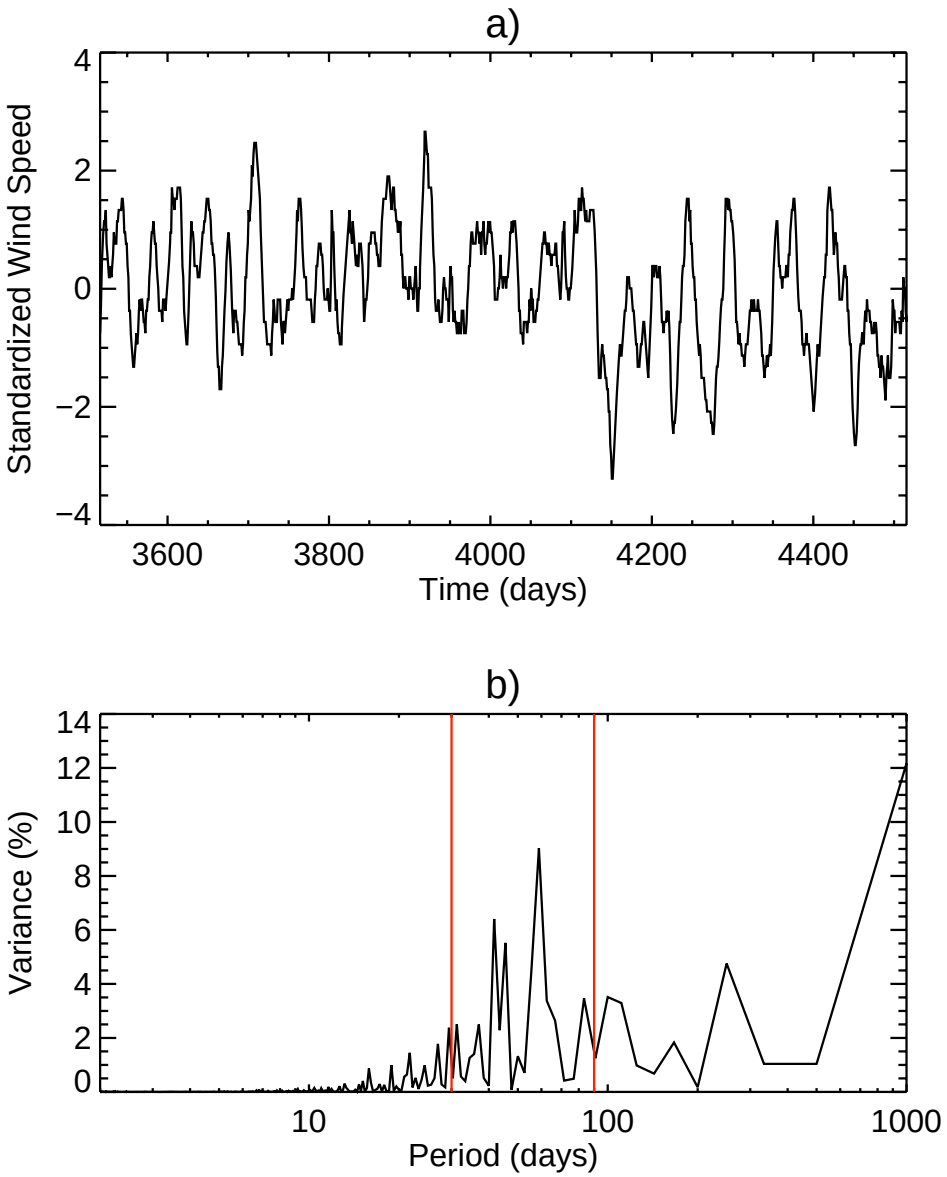

Figure 73: a) Time series and b) Fourier spectra of surface wind speed generated by the prognostic coupled model for the last 1000 days of integration.

of variance within the band is also very similar. The spectral differences are seen at higher frequencies where the observations show an additional biweekly peak that is not represented by the model results. However, the OLR variability at that time scale is mostly uncoupled (Figure 67). Since the model only represents the local coupled processes, it was expected that the observed uncoupled higher frequency OLR variability would not be resolved in the simulations. Another interesting feature

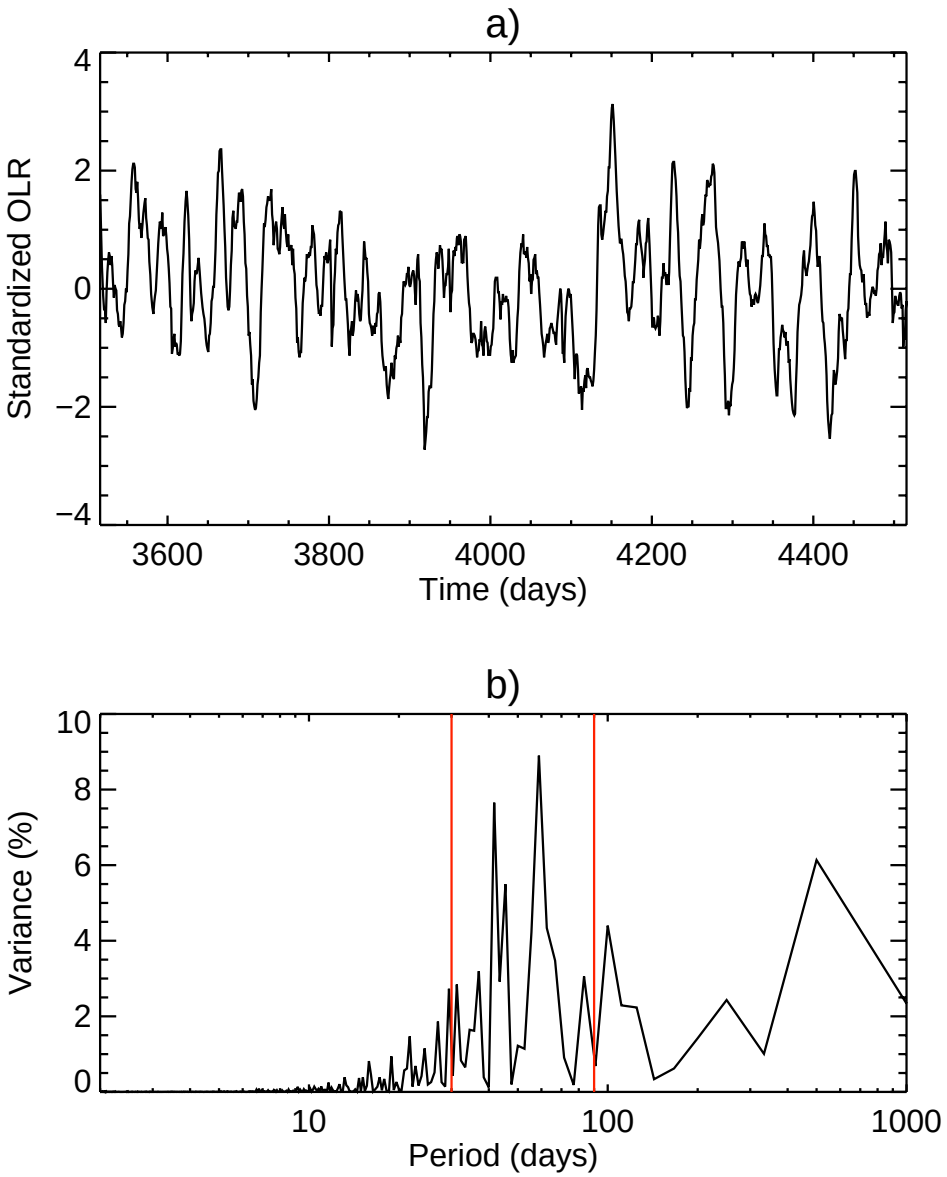

Figure 74: Same as Figure 73 but for OLR.

evident in the Fourier spectrum of simulated OLR is the fact that the oscillation is not regular, which is reflected in the broad spectral peak. This spectral feature has a major implication: The periodicity of the oscillation as well and the strength of the intraseasonal events is not constant. This irregular behavior that mimics the observations most likely originates in the non-linear nature of the ocean mixed layer model since the atmospheric prognostic equations are linear.

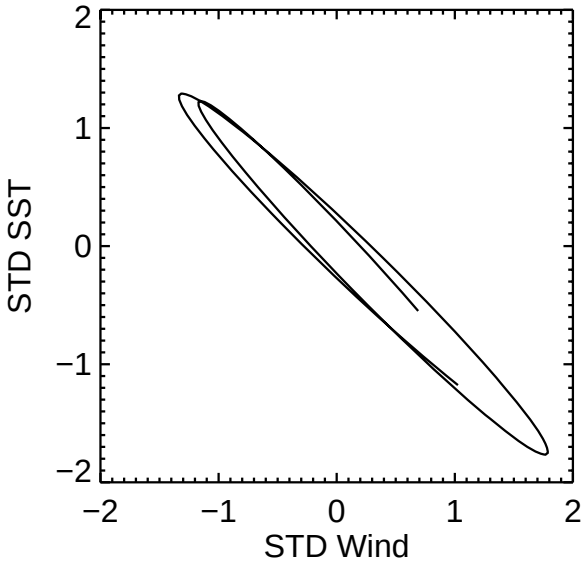

Figure 75: Phase diagram between filtered (25-80 days) SST and surface wind speed simulated by the prognostic model for two ISO cycles.

In summary, results of the simulations carried out with the very simple semi-empirical prognostic coupled model support the working hypothesis presented at the beginning of this chapter: Local coupling between the ocean and the atmosphere results in local intraseasonal variability mainly due to feedbacks between SST and both convective activity and surface wind speed which control the evolution of the surface radiative and latent heat fluxes in the model.

Different simulations were completed using several different initial conditions representing radically different oceanic profiles. Results suggest that while the state of the system (e.g. SST, surface wind speed, OLR, etc.) at a given time depends on the initial conditions, the attractor of the coupled system is invariant to changes in initial conditions. This means that the spectral features are not dependent on the initial conditions. Fourier spectra of all the runs using different initial conditions show a marked broad spectral peak in the intraseasonal band.

It is also interesting to test the sensitivity of the resulting oscillation to variations in the strength of the surface coupling. This test corresponds to explore the behavior

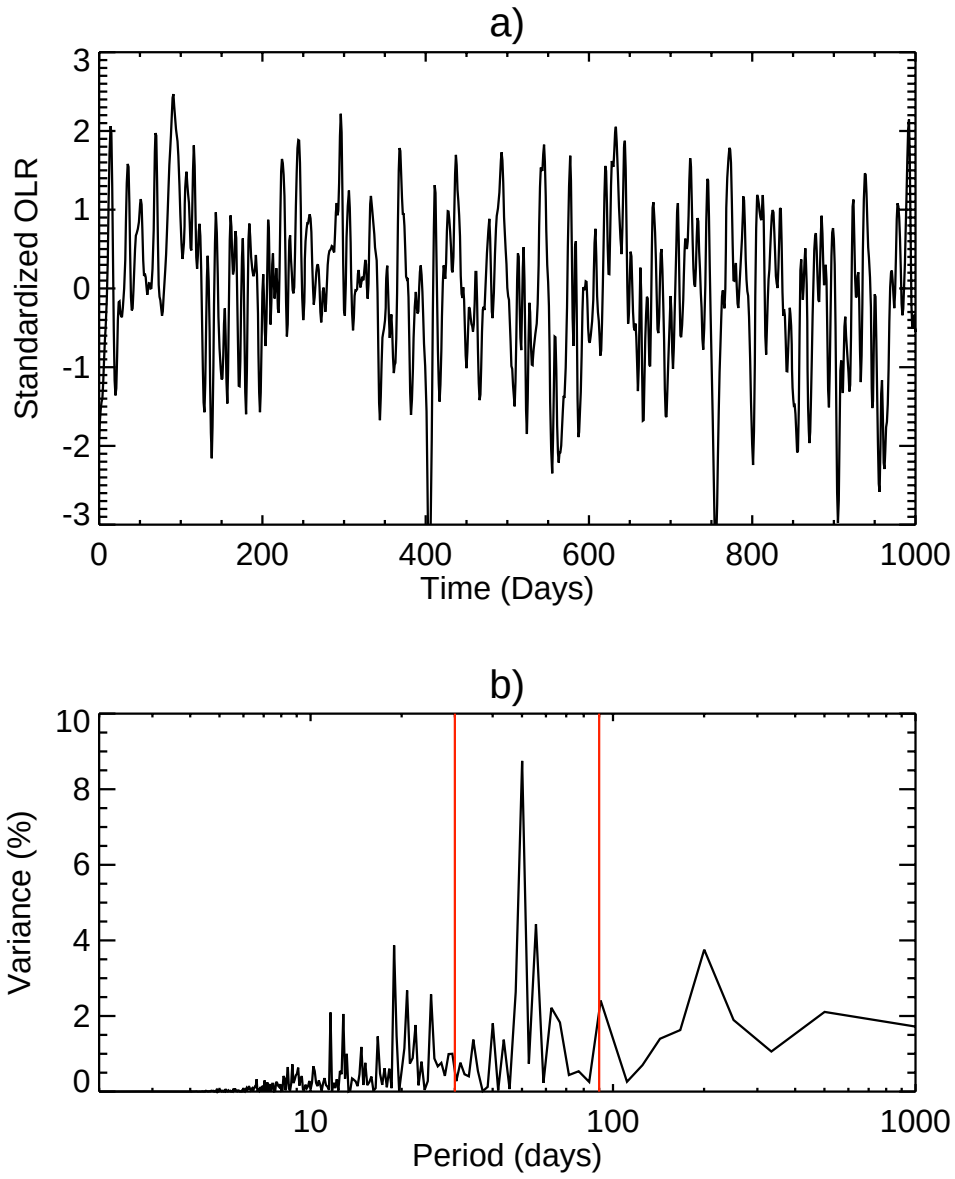

Figure 76: Same as Figure 73 using 1000 days of OLR observations starting January 1st 1998.

of the coupled systems around the average atmospheric response to changes in SST. In this context, strength of the surface coupling is associated with the magnitude of the OLR and surface wind speed tendencies in the prognostic equations, which then modulate the magnitude of the surface fluxes. Since the prognostic relationships are linear, changing the magnitude of the tendencies correspond to changing the slope of the linear relationships without changing the intercept in the SST axis. Figure 77a to

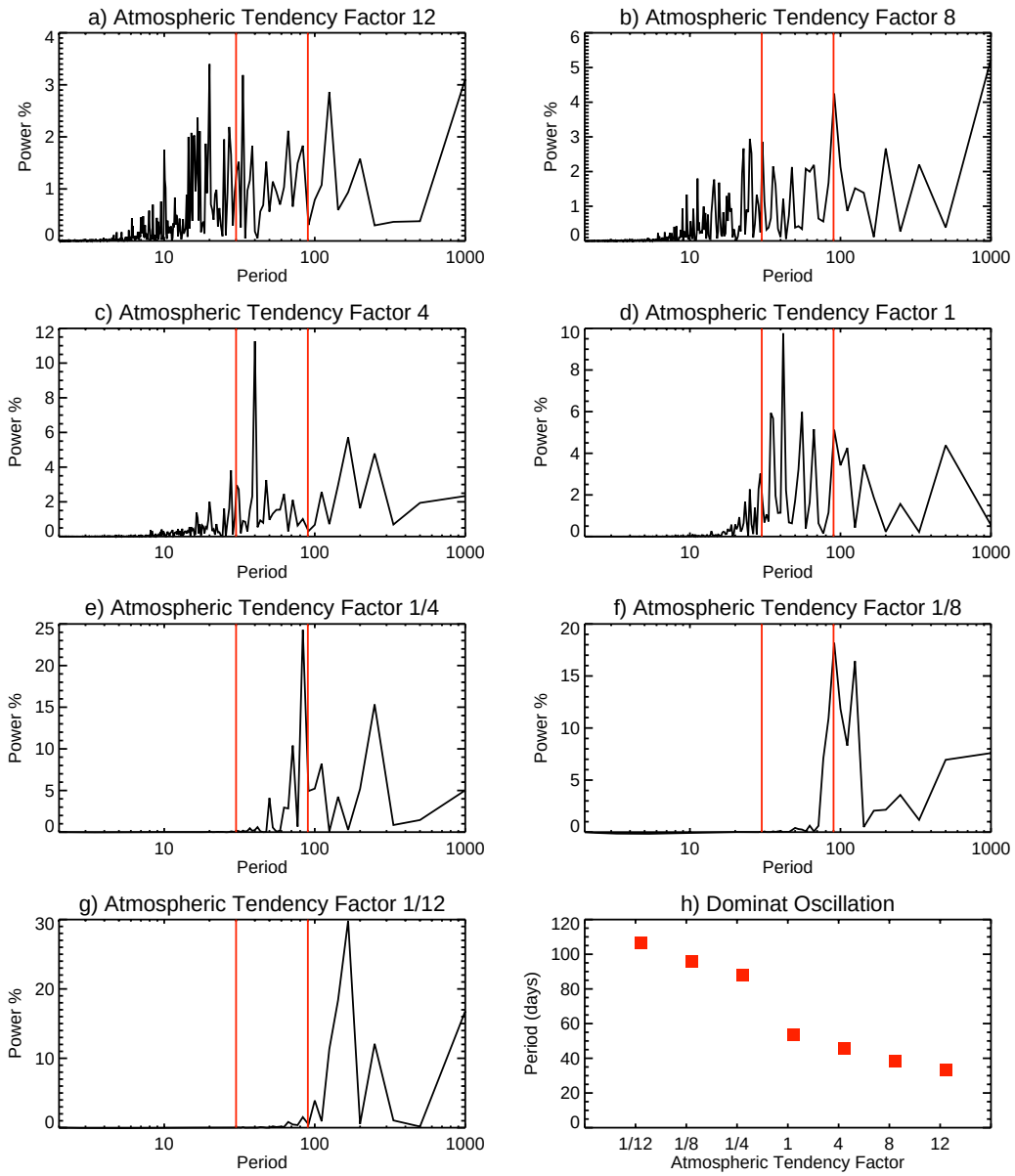

Figure 77: a) to g) Fourier spectra of the simulated OLR for different atmospheric tendency factors. h) Period of the dominant oscillation as a function of different atmospheric tendency factors.

Figure 77g summarize the results of this sensitivity test by showing the Fourier spectrum of OLR for different atmospheric tendency factors that change the strength of the atmospheric response (OLR and surface wind speed). The atmospheric tendency factor is just the magnitude by which the slopes of the prognostic equations (both OLR and surface wind speed) were multiplied. Figure 77h shows the period of the

dominant oscillation as a function of the atmospheric factors used in the sensitivity test. Results indicate that a more (less) responsive atmosphere leads to higher (lower) frequency oscillations. However, it is clear that there is a range of atmospheric responsiveness (tendency factor between $\sim$4 and $\sim$1/4) in which the model converge to intraseasonal oscillations. This is consistent with observations which indicate that the intraseasonal oscillation in nature is a very coherent feature that exists under very different large-scale climate backgrounds that tend to alter the degree of coupling between ocean and atmosphere. In other words, the existence of intraseasonal variability in the model does not depend, within a reasonable range, on the magnitude of the atmospheric response (values of parameters in prognostic equations) to variations of SST. In nature it is similar; while the exact magnitude of such response depends on the state of many variables at many levels (millions of degrees of freedom), the character of ISO is robust.

While the results previously presented indicate the importance of the local coupling in the generation intraseasonal variability, they don't provide a definitive conclusion about the role of the oceanic mixed layer determining the time scale of the oscillation.

In the mixed layer ocean model one of the variables that is prescribed is the depth of the ocean, here referred to as the active ocean depth. This is the column of water where the model is integrated and all the vertical processes included in the model take place. In order to analyze the effect of the active ocean depth in the time scale of the oscillation, a series of experiments were conducted with the model set with the same specifications as before but with different active ocean depths. By doing this, the depth of the oceanic mixed layer could be at most equal to the active ocean depth prescribed in the model.

It is clear that the mixed layer should be determined by salinity and temperature and that by changing the ocean depth we are artificially limiting the model to a mixed

layer depth that might not be dictated by the conditions of the ocean, especially when values of the active ocean depth are small. However, we are interested in testing the response of the model to the changes in the active ocean depth and whether or not it influences the resulting oscillation. In all the simulations we monitored the model evolution to ensure that not numerical errors were introduced by reducing the active ocean depth. Other ways of changing the mixed layer depth are for example including advection or increasing the entrainment. Those should also be tested in order to have a better assessment of the importance of the mixed layer depth.

Figure 78 shows the Fourier spectrum for each of the simulated OLR time series for 12 different active ocean depths ranging from a 5 m to 150 m. The spectral features of the simulated OLR are very different for each of the active ocean depths used. For shallow active oceans the model converges to a higher frequency oscillation than for deeper active oceans. This finding is summarized in Figure 79 by showing the period of the resulting dominant oscillation in the simulations as a function of the active ocean depth. The period of the dominant oscillation is defined as the center of the spectral band that contains more variance than all the other spectral bands with the same spectral width. The dominant oscillation can be thought as the period corresponding to the maximum power in the smoothed Fourier spectrum (moving average of the spectrum). In this manner we account for the presence of broad spectral peaks. Figure 79 clearly shows how the period of the dominant oscillation increases as the active ocean depth increases. This increase appears to be in an asymptotical manner. There is a sharp increase for depths between 5 and 50 meters and then a slow, non-statistically significant increase from 50 to 150 meters (i.e. almost flat). When the ocean is shallow, the SST seems to responds quickly and vigorously to variability in turbulent and radiation fluxes at the surface resulting in higher frequency and relatively narrow spectral peaks as can be seen in the first panel of Figure 78. In the model, this is because surface wind speed tendencies are stronger for higher SSTs

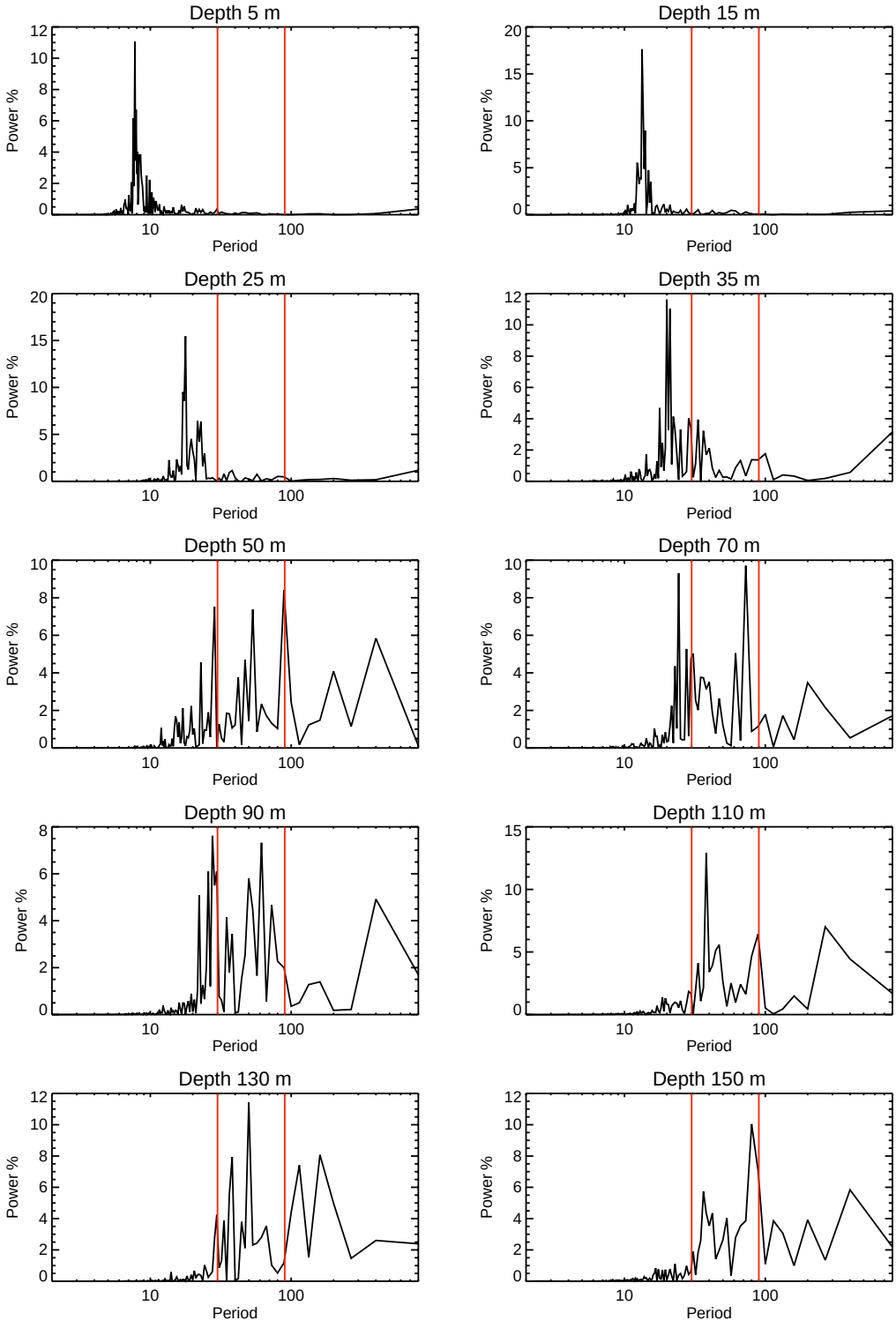

Figure 78: Fourier spectrum of OLR simulated by the model for 12 different active ocean depths from 5 m to 150 m.

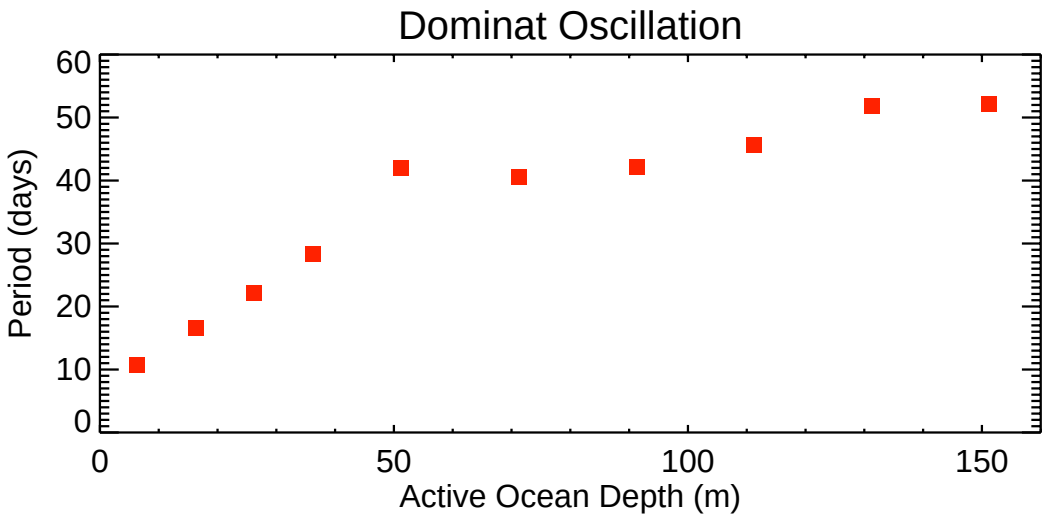

Figure 79: Period of the resulting dominant oscillation in the model vs. the prescribed active ocean depth.

(which are due to shallow oceans and the inability to mixed the heat further down), and due to the non-linear nature of mixing and evaporation, the SST is cooled faster, resulting in higher frequency oscillations for shallower oceans. This is consistent with observations as it was pointed out in previous paragraphs.

For active ocean depth of 35 meters or deeper when the model is allowed to develop an oceanic mixed layer of about 35 meters, an asymptotical behavior is present, the mixed layer depth converges and it is independent of ocean active depth. When the oceanic mixed layer is not allowed to develop as in observations (active ocean depths less than 35 meters) the resulting oscillation has a higher frequency. This limit of 35 meters is also consistent with observations that suggest that the average depth of the mixed layer in the warm pool region is about 30 meters deep. These results suggest that the oceanic mixed layer plays a role in the life cycle of the ISO and its temporal scale.

So far results suggest the important role of the processes which control the local coupling in generating a local intraseasonal oscillation as well as the importance of the oceanic mixed layer depth in determining the time scale of such oscillation.

Also, it is relevant to mention that is well known that most of the ISO events in the Indian Ocean-West Pacific warm pool propagate eastward (known as the Madden-Julian Oscillation) which could not be studied by using our one dimensional coupled model as the one presented in this chapter. However, one possibility for the existence of the MJO is that the intraseasonal oscillation is generated locally according to the atmosphere-ocean coupling previously described and then projects onto the equatorial zonal (convectively-coupled) modes resulting in the eastward propagation of the convective anomalies. Currently we are planning to use the WRF tropical channel model coupled with a mixed layer ocean model in order to test this hypothesis.

CHAPTER VI

CONCLUSIONS

In the Tropics, and in particular in the Indian Ocean-West Pacific basin, the intraseasonal oscillation (ISO), which corresponds to anomalies in the 30-80 day band, is one of the most important and robust modes of atmospheric and oceanic variability that significantly affects the circulation throughout the global Tropics and subtropics. In spite of its importance there is still a lack of understanding about the mechanisms that trigger and modulate the lifecycle of the ISO. In addition, climate and forecasting models lack of skill representing the ISO. Processes associated with the life cycle of an ISO event are complex and involve both the ocean and the atmosphere, resulting in modulation of the convective activity which can be separated into three different phases: suppressed, transition and convective phases. We have hypothesized that local coupling between the ocean and the atmosphere is essential for the existence and evolution of the intraseasonal oscillation in the Indo-Pacific warm pool region, and particularly that thermodynamical processes during the transition between the suppressed and active phases are critical to the development of the onset and evolution of the active phase of the ISO. One of the objectives of this analysis was to identify the key processes of the transition phase that lead to the existence of a long-lived convective envelope, and to evaluate the skill of numerical models with different degrees of complexity in reproducing those processes in order to detect when and why models fail to represent the life-cycle of the ISO.

In this study we presented a detailed diagnostic analysis of the life-cycle of the transition stage between suppressed and deep convection, evaluated the skill of the ECMWF coupled model in forecasting the vertical structure of circulation and moist

convective anomalies associated with the ISO, and evaluated the performance of a coupled single column model in simulating the ISO. In addition, we designed a semi-empirical coupled model in which only processes identified as relevant in diagnostic analysis are included in the atmospheric component of the model. The semi-empirical model was used to determine whether or not the local coupling between the ocean and the atmosphere could result in intreaseasonal variability and to study the role of the oceanic mixed layer in the time scale of the resulting ISO.

The diagnostic study has provided a synthesis of observations of the two ISOs occurring during the TOGA COARE IOP that clarifies the role of clouds, moisture and convection during the ISO transition through application of a satellite-based cloud classification scheme that includes information on precipitation types as well as cloud top temperature/height. During the transition phase low-level moistening of the troposphere appears to precondition the atmosphere for the formation of deep convection. Sea surface temperature is higher during the transition due to the lack of clouds and weak surface winds during the undisturbed phase. Positive anomalies of SST, which are the source of the necessary energy to maintain the strong moist convection observed in association to the ISO, are as well the source of atmospheric instability. SST anomalies cause changes in atmospheric boundary layer temperature creating anomalous surface pressure gradients, winds and low level mass convergence which may lead to convection. Surface winds are strengthened and exert stress over warmer than average surface oceanic waters, leading to enhanced evaporation. In this case surface evaporation appears as a necessary (but not sufficient) condition for the low-level moistening. Large-scale subsidence plays a very important role since it inhibits local development of deep convection hence favoring the moisture build-up from positive anomalies of low level humidity and the build-up of CAPE preconditioning the atmosphere for deep convection. As a result of the moistening, there is a reduction of cloud-free areas and formation of midtop non-precipitating clouds during

the transition phase. Warm (shallow) nonprecipitating clouds tend to be present at all times, and their variability is not associated, at least directly, with the ISO. Once deep convection is initiated, intense precipitation and upper tropospheric warming due to latent heat release is observed. Westerly winds reach maximum strength during or short after the maximum convection. The clouds associated with the active convection reduce the amount of sunlight reaching the surface, cooling the surface of the ocean. With the reduction of SST, the active phase ends. ISO events modify not only the atmospheric structure but also the oceanic mixed layer, inducing temperature and salinity changes.

The low-level moistening during the transition phase appears also as an important feature of the ISO event occurred during the JASMINE experiment that took place over the Bay of Bengal during summer 2004. Composite analysis of intraseasonal anomalies of specific humidity of 38 winter and 31 summer ISO events confirms that the low level moistening is a robust feature that is important for the development of ISO events during both seasons.

To gain a better understanding of the problems that numerical models have in simulating and forecasting the ISO, we evaluated the skill of the ECMWF coupled model to reproduce the processes that occur during the transition from suppressed to active convection. The regional and local vertical structure of ISO from the numerical forecasts during the different phases of the oscillation was also studied. We explored extended numerical simulations during the TOGA COARE case, which took place during winter, as well as important ISO events during the summers of 2002 and 2004. This is important because most studies only address the predictability and prediction of the winter ISO.

We found that the forecast skill of the tropospheric vertical structure associated with the ISO in the Indo-West Pacific region during winter strongly depends on the state of the atmosphere at the beginning of each forecast run. In addition, there are

states of the system for which the skill of the forecast is always low. Those states coincide with convective events, for which the skill of the forecast decreases regardless of the starting date of the forecast. Forecasts for 5-day average anomalies of zonal winds in the equatorial Indian Ocean-West Pacific region were shown to be skillful up to about 13 days. Forecasts of specific humidity have no skill whatsoever indicating the model's lack of skill to simulate moist convective processes. During summer the general results are similar however, the time scale of skillful forecasts during summer is between 5-7 days, half of what was observed for winter. Even though the number of cases evaluated is limited, these results suggest that the skill of the forecast is greater for winter ISO cases than for summer events. A possible explanation for this seasonal difference is the fact that the circulation structure of the summer ISO is more complex than during winter as it has not only an eastward propagating convective center but also a northward propagating one. Results for the summer analysis suggest the model is always forecasting an active-like phase of the monsoon. This active-like phase corresponds to the annual character of the monsoon. Since the model is not able to skillfully forecast the generation of positive and negative specific humidity anomalies in the Indian Ocean around the equator, convective anomalies would not propagate from the equator resulting in a monsoon without intraseasonal modulation.

When comparing model results with the ERA-40 data set, it was found that forecast temperature profiles are about 1 degree cooler than ERA-40 near the surface and about 0.5 degree warmer around 500mb. The model also tends to simulate a dryer atmosphere compared to the ERA-40. These discrepancies limit the model's capability to reproduce of deep convective events associated with the ISO.

For the transition phase we showed that the ECMWF coupled model was not able to reproduce, even in the short term, the observed moisture build-up associated with ISOs during TOGA COARE or during two different ISO cases that took place during the boreal summers of 2002 and 2004. The model was unable to develop the

low level moistening of the atmosphere if those conditions are not already part of the initial conditions. The observed CAPE build-up prior to the convective stage was absent in the model simulations. Predictability of the active convective period of the ISO is poor when initialized before the transitional phases of the ISO. However, when initialized with the lower tropospheric moisture included, predictability increases substantially, although the model convective parameterization appears to trigger convection too quickly without allowing an adequate buildup of convective available potential energy during the transition period. Overall, the analysis suggests deficiencies in parameterizations of convection and air-sea interactions. The model appears to produce subsidence that is too weak or a cloud parameterization that is insensitive to subsidence. In summary, the analysis of the ECMWF simulations points out towards model inadequacies that, if corrected, could lead to improved simulations and predictions of the ISO.

A coupled single column model was used to further detect and study the problems of numerical models simulating long-lived convective activity. The atmosphere component of the model is the single column version of the NCAR Climate Community System Model and the oceanic module to the mixed layer ocean model developed by Kantha and Clayson (1994, 2004). Results of the analysis of the vertical structure of the atmosphere in the simulations, and in particular of those features associated with moist convection, suggest a high degree of sensitivity to the estimation of the surface fluxes. Such sensitivity serves as further evidence of the importance of the local thermodynamical coupling in the evolution of the ISO. In general the single column coupled model poorly represented the slow atmospheric moistening and the extended convective periods. One of the problems encountered was that the model underestimated the surface latent heat flux, resulting in a drier atmosphere compared to observations. The model generated convective precipitation during the entire simulation period, not allowing the moistening of the atmosphere and the accumulation

of convective potential energy. Furthermore, the model's deep convection parameterization generates convective bursts, which could potentially be one of the reasons some global climate model have spectra that are too 'red' (i.e. too much high-frequency variability). Circulation and temperature anomalies introduced by this type of high frequency convective bursting could potentially limit considerably the skill of numerical models to simulate and forecast the ISO. Convective bursts inhibit the build up of CAPE that is needed to sustain extended convective activity. The existence of convective bursting in models might be the result of self-suppression processes associated with deep convection in convective parameterizations (Lin et al. 2006a). In the wake of a deep convection event, unsaturated convective downdrafts significantly dry and cool the boundary layer (e.g. Houze 1977), suppressing the immediate formation of convective updrafts that suppress the development of new deep convection and, thus, decrease the persistence of precipitation. Future research will be conducted in order to address this issue as well as to the development or improvement of triggering functions of convection based on the ISO caracteristics. We consider the possibility that a better triggering function (or a secondary one) that considers the life-cycle of the ISO, will control the convective bursting. Lin et al. (2006) showed that while similar versions of the Tiedke (1989) scheme are used in the ECMWF and the MPI (Max Planck Institute model), MPI results in a better representation of the MJO. The main difference between the two versions of Tiedke scheme is in the convective trigger: the MPI model uses a moisture convergence trigger while the ECMWF model uses an instability trigger.

In general, our results suggest that some models tend to quickly develop convection from local instabilities rather than slowly build up the energy (CAPE) needed to sustain the kind of extended convective events associated with the observed ISO. Models like the ECMWF, which appeared to generate a more stable atmosphere compared to observations, also inhibit the build-up of CAPE. One of the consequences

of the lack of CAPE is that the amplitude of the ISO in the models quickly goes to zero as the integration time increases.

To test the hypothesis that local thermodynamic coupling between the atmosphere and the upper ocean in the tropical western Pacific warm pool controls the life cycle of the intraseasonal oscillation and in particular its time scale, we designed a semi-empirical one-dimensional coupled model to reproduce the coupled ISO over long integration periods including only local processes and without a convective parameterization. The semi-empirical model consisted of a one-dimensional ocean mixed layer model that is driven by an empirically-derived atmospheric model whereby surface meteorological and flux variables are related statistically to changes in SST. To obtain the variables needed by the ocean mixed layer model from the atmospheric model, we constructed a set of empirical relationships between time series of local SST and surface wind speed, specific humidity, air temperature, precipitation, surface pressure, downward long wave and solar radiation at the surface. Empirical diagnostic equations which directly link the values of SST with the values of a particular atmospheric variable, simultaneously (same time, same day) were constructed for all the variables except for surface winds and cloudiness in which prognostic equations were used. These empirical prognostic equations predict the values of the atmospheric variables for the next time step of the integration. This setting assures that feedbacks with the upper ocean are controlled only by changes in surface winds and cloudiness which together modulate the turbulent and radiation fluxes and, we believe, control the strong coupling between the ocean and the atmosphere.

When the model was run using only diagnostic equations, SST asymptotically increases until near-stabilization around an unrealistically high value because the lack of mechanisms (negative feedbacks) to cool down the ocean, indicating that the model does not have an inherent oscillation if negative feedbacks between the atmosphere and the ocean do not exist. On the other hand when surface wind speed

prognostic equations were included, the model converges to a quasi-periodic oscillation and a remarkable broad-band intraseasonal spectral peak, very similar to the ISO spectrum obtained from observations. An important feature of the simulated OLR Fourier spectrum reflected in the broad spectral peak is the lack of regularity of the oscillation. The periodicity of the oscillation as well and the strength of the intraseasonal events is not constant. This irregular behavior that mimics observations most likely originates in the non-linear nature of the ocean mixed layer model since the atmospheric prognostic equations are linear. Since only unfiltered data was used in the derivation of the atmospheric model the resultant oscillation in the simulations is a product of the coupled mechanisms represented in the model and not a result of any kind of artificial forcing within the set of empirical relationships. The model results supports our hypothesis that local coupling between the ocean and the atmosphere results in local intraseasonal variability mainly due to feedbacks between SST and both convective activity and surface wind speed which control the evolution of the surface radiative and latent heat fluxes in the model. We also tested the sensitivity of the resulting oscillation to variations in the strength of the surface coupling. Results indicated that the existence of intraseasonal variability in the model does not depend, within a reasonable range, on the magnitude of the atmospheric response (values of parameters in prognostic equations) to variations of SST. This conclusion points to the robust character of the ISO in nature.

The role of the oceanic mixed layer in determining the time scale of the oscillation was also studied using the semi-empirical model. A series of experiments were conducted with the model set to different ocean depths. By changing the active ocean depths we found that for shallow active oceans the model converges to higher frequency oscillations than for deeper active oceans. The period of the dominant oscillation increases asymptotically as the active ocean depth increases. When the ocean is shallow, the SST seems to respond quickly and vigorously to variability in

turbulent and radiation fluxes at the surface resulting in higher frequency and relatively narrow spectral peaks. When the model is allowed to develop an oceanic mixed layer of about 35 meters the mixed layer depth converges and it is independent of ocean active depth. This limit of 35 meters is also consistent with observations that suggest that the average depth of the mixed layer in the warm pool region is about 30 meters deep. These results suggest that the oceanic mixed layer plays an important role in the life cycle of the ISO and in the determination of its temporal scale. Future testing involving different approaches to control the modeled mixed layer depth should be carry out in order to confirm the results obtained in this study highlighting the importance of the oceanic mixed layer in the life-cycle of the ISO.

Results of the semi-empirical single column model lead to further questions that will be addressed in future research. One of them refers to the well-known fact that most of the ISO events in the Indian Ocean-West Pacific warm pool propagate eastward (MJO), which was not considered in our study. While our results point to the importance of local thermodynamical coupling for the generation of local intraseasonal oscillation, one possibility for the existence of the MJO is that the intraseasonal oscillation is generated locally according to the mechanism previously described and then projects onto the equatorial zonal (convectively-coupled) modes resulting in the eastward propagation of the convective anomalies. To test this hypothesis, we plan to use a coupled tropical channel version of the WRF model with a mixed layer ocean model (e.g. Kantha and Clayson mixed layer model).

It is well known that the maximum amplitude of the ISO activity occurs over the Indian Ocean and the West Pacific warm pool. One issue to address in future research is why there is no robust intraseasonal variability in the Atlantic. It is observed that the distribution of intense ISO activity coincides with the regions where SST is greater than 28°C. As it was mentioned before, high SST provides the source of atmosphere instability and moisture necessary to sustain long-lived convection. High

SST regions in the tropics also coincide well with the integrated atmospheric heating, which is a major driver of the atmospheric circulation (Webster and Lukas 1992). Over the Atlantic, the average temperature is below 28°C limiting the formation of intraseasonal events. In addition, the mixed layer in the Atlantic is deeper than in the West Pacific, which would result in a much slower response of the ocean to changes in the surface meteorology.

The local diagnostic relationship between SST and OLR in the Western Pacific warm pool used in the semi-empirical model is such that the minimum OLR does not coincide with the maximum SST but it occurs at about 29.5-30.0°C. Previous studies have found similar results when studying basing-wide convection in the Pacific using monthly data (e.g. Waliser and Graham 1993, Lat et al. 1997) and have addressed the potential development of "hot-spots" which refer to regions of high SST (>30°C) without convection during some periods of time. Some have referred to this as the "hot-spot paradox" (e.g. Tompinks 2001). One of the reasons for the development of the apparent hot-spots in the West Pacific is hypothesized to be in part due to the fact that the effects of the ISO lifecycle in the overall SST-convection relationship are not considered appropriately. Very warm SSTs in the West Pacific warm pool may only occur under conditions of suppressed convection, but at the same time anomalously high SST tends to drive convection, which subsequently acts to decrease SST. This will be addressed in detail in future research.

REFERENCES

[1] Agudelo, P. A., and J. A. Curry, 2004: Analysis of spatial distribution in tropospheric temperature trends. *Geophys. Res. Lett.*, **31**, L22207, doi: 10.1029/2004GL020818.

[2] Bergman, J.W., P. D. Sardeshmukh, 2004: Dynamic Stabilization of Atmospheric Single Column Models. *J. Climate* **17**, 1004-1021.

[3] Chang, C. P., and H. Lim 1988: Kelvin wave-CISK: A possible mechanism for the 30-50 day oscillations, *J. Atmos. Sci.*, **45**, 1709-1720

[4] Ciesielski, P.E., R.H. Johnson, P.T. Haertel and J. Wang 2003: Corrected TOGA COARE sounding humidity data: Impact on diagnosed properties of convection and climate over the warm pool. *J. Climate.*, **16**, 2370-2384.

[5] Clayson, C. A., and A. Chen, 2002: Sensitivity of a Coupled Single-Column Model in the Tropics to Treatment of the Interfacial Parameterizations. *J. Climate.*, **15**, 1805-1831.

[6] Clayson, C. A., J. A. Curry, and C. W. Fairall, 1996: Evaluation of turbulent Fluxes at the ocean surface using surface renewal theory. *J. Geophys. Res.*,**101**, 28503-28513.

[7] Clayson, C. A., and L. H. Kantha, 1999: Turbulent kinetic energy and dissipation rate in the equatorial mixed layer. *J. Phys. Oceanogr.*, **29**, 2146-2166.

[8] Curry, J. A., C. A. Clayson, W.B. Rossow, R. Reeder, Y.-C. Zhang, P.J. Webster, G. Liu, and R.-S Sheu, 1999: High-Resolution Satellite-Derived Dataset of

the Surface Fluxes of Heat, Freshwater, and Momentum for the TOGA COARE IOP. *Bull. Amer. Meteor. Soc.*, **80**,2059-2080.

[9] Emanuel, K. A., 1987: An air-sea interaction model of intraseasonal oscillations in the tropics, *J. Atmos. Sci.*, **44**, 2324-2340.

[10] Fairall, C.W., E.F. Bradley, D.P. Rogers, J.B. Edson, G.S. Young, 1996b: Bulk parameterization of air-sea fluxes for TOGA COARE. *J. Geophys. Res.* **101**, 3747-3764.

[11] Feng, M., R. Lukas, P. Hacker, R.A. Weller, and S.P. Anderson, 2000: Upper-ocean heat and salt balances in the western equatorial Pacific in response to the intraseasonal oscillation during TOGA COARE, *J. Climate.*, **13**, 2409-2427.

[12] Flatau, M., P. J. Flatau, P. Phoebus, and P. P. Niiler, 1997: The Feedback between Equatorial Convection and Local Radiative and Evaporative Processes: The Implications for Intraseasonal Oscillations. *J. Atmos. Sci.*, **54**, 2373-2386.

[13] Fu, X., and B. Wang, 2004: Differences of boreal summer intraseasonal oscillations simulated in an atmosphere-ocean coupled model and an atmosphere-only model. *J. Climate*, **17**, 1263-1271.

[14] Fu, X., B. Wang, T. Li, and J. P. McCreary, 2003: Coupling between northward propagation intraseasonal oscillations and sea surface temperature in the Indian Ocean. *J. Atmos. Sci.*, **60**, 1733-1753.

[15] Gill, A., 1982: *Atmospheric-ocean dynamics*, Academics Press, New York, 662 pp

[16] Gill, A. E., 1980: Some simple solutions for heat-induced tropical circulation. *Quart. J. Roy. Met. Soc.*, **106**, 447-462.

[17] Godfrey, J. S., R. A. Houze, R. H. Johnson, R. Lukas, J.-L. Redelsperger, A. Sumi, and R. Weller, 1998: Coupled Ocean-Atmosphere Response Experiment (COARE): An interim report. *J. Geophys. Res.*, **103**, 14395-14450.

[18] Gutzler, D. S., G. N. Kiladis, G. A. Meehl, K. M. Weickmann, and M. Wheeler, 1994: The global climate of December 1992-February 1993. Part II: Large-scale variability across the tropical western Pacific during TOGA COARE, *J. Climate*, **7**, 1606-1622.

[19] Hack, J. J., and J. A. Pedretti, 2000: Assessment of solution uncertainties in single-column modeling frameworks. *J. Climate*, **13**, 352-365.

[20] Hack, J. J., B. A. Boville, B. P. Briegleb, J. T. Kiehl, P. J. Rasch, and D. L. Williamson, 1993: Description of the NCAR Community Climate Model (CCM2). *NCAR Tech. Note* **3361**, 108.

[21] Hartmann, D.L., 1994: *Global Physical Climatology*. Academic Press, 411 pp.

[22] Hendon, H. H. 1988:, A simple model of the 40-50 day oscillation, *J. Atmos. Sci.*, **45**, 569-584.

[23] Hendon, Harry H., Liebmann, Brant. 1990: The Intraseasonal (30-50 day) Oscillation of the Australian Summer Monsoon. *J. Atmos. Sci.*, **47**, 2909-2924.

[24] Hendon, Harry H., Liebmann, Brant, Glick, John D., 1998: Oceanic Kelvin Waves and the MaddenJulian Oscillation. *J. Atmos. Sci.*, **55**, 88-101.

[25] Hendon, H. H., and M. L. Salby, 1994: The life cycle of the Madden-Julian oscillation. *J. Atmos. Sci.*, **51**, 2207-2219.

[26] Higgins, R. W., and S. D. Schubert, 1996: Simulations of persistent North Pacific circulation anomalies and interhemispheric teleconnections. *J. Atmos. Sci.*, **53**, 188-207.

[27] Higgins, W and W. Shi, 2001: Intercomparison of the principal modes of interannual and intraseasonal variability of the North American monsoon system. *J. Climate*, **14**, 403-417.

[28] Higgins, R. Wayne, Mo, Kingtse C. 1997: Persistent North Pacific Circulation Anomalies and the Tropical Intraseasonal Oscillation. *J. Climate*, **10**, 223-244.

[29] Hollinger, J.P., J.L. Peirce, and G.A. Poe, 1990: SSM/I instrument evaluation, *IEEE Trans. on Geosci. Remote Sens.*, **28**, 781-790.

[30] Holtslag, A. A. M., and B. A. Boville, 1993: Local versus nonlocal boundary-layer diffusion in a global climate model. *J. Climate*, **6**, 1825-1842.

[31] Hoyos, C. D., and P. J. Webster, 2007: The Role of Intraseasonal Variability in the Nature of Asian Monsoon Precipitation . *J. Climate*, **20**, 4402-4424.

[32] Hoyos, C. D., 2006: Intraseasonal *Variability: Processes, Predictability and Prospects for Prediction*. PhD Thesis, Georgia Institute of Technology, 188 pp. (http://hdl.handle.net/1853/10530) handle.net/1853/10530)

[33] Houze, R. A., 1977: Structure and dynamics of a tropical squallline system. *Mon. Wea. Rev.*, **105**, 1540-1567.

[34] Hye-Mi Kim, C. D. Hoyos, P. J. Webster, and I. Kang, 2007: Sensitivity of MJO simulation and predictability to sea surface temperature variability. *J. Climate*, submitted.

[35] Inness, P. M. and J. M. Slingo 2003: Simulation of the Madden-Julian oscillation in a coupled general circulation model. Part I: Comparison with observations and an atmosphere-only GCM. *J. Climate,* **16**, 345-364

[36] Johnson, R. H., T. M. Rickenbach, S. A. Rutledge, P. E. Ciesielski, and W. H. Schubert, 1999: Trimodal characteristics of tropical convection. *J. Climate*, **12**, 2397- 2418.

[37] Johnson, R. H., and X. Lin, 1997: Episodic trade wind regimes over the western Pacific warm pool. *J. Atmos. Sci.*, **54**, 2020-2034.

[38] Jones, C., D. E. Waliser and C. Gautier, 1998: The Influence of the Madden-Julian Oscillation on Ocean Surface Heat Fluxes and Sea Surface Temperature. *J. Climate*, **11**, 1057-1072.

[39] Jones C., L. M. V. Carvalho, R. W. Higgins, D. E. Waliser and J.-K. E. Schemm. 2004: A Statistical Forecast Model of Tropical Intraseasonal Convective Anomalies. *J. Climate*, **17**, 2078-2095.

[40] Jones, C., and J.-K. E. Schemm, 2000: The influence of intraseasonal variations on medium-range weather forecast over South America, *Mon. Weather Rev.*, **128**, 486-494.

[41] Jones, C., 2000: Occurrence of extreme precipitation events in California and relationships with the Madden-Julian oscillation. *J. Climate*, **13**, 3576-3587

[42] Jones, C., and B. C. Weare 1996: The role of low-level moisture convergence and ocean latent heat flux in the Madden-Julian Oscillation: An observational analysis using ISCCP data and ECMWF analyses, *J. Climate*, **9**, 3086-3104.

[43] Kantha, L. H., and C. A. Clayson, 2004: On the effect of surface gravity waves on mixing in the oceanic mixed layer. *Ocean Modelling*, **6**, 101- 124.

[44] Kantha, L. H., and C. A. Clayson, 1994: An improved mixed layer model for geophysical applications. *J. Geophys. Res.*, **99**, 25235-25266.

[45] Kawamura, R., 1991: Air-sea coupled modes on intraseasonal and interannual time scales over the tropical western Pacific, *J. Geophys. Res.,* **96**, 3165-3172.

[46] Kemball-Cook, S.R., and B.C. Weare, 2001: The onset of convection in the Madden-Julian oscillation. *J. Climat*e, **14**, 780-793.

[47] Kemball-Cook, S. R., B. Wang, and X. Fu, 2002: Simulation of the intraseasonal oscillation in the ECHAM4 model: The impact of coupling with an ocean model. *J. Atmos. Sci.*, **59**, 1433-1453.

[48] Kemball-Cook, S.R., and B.C. Weare, 2001: The onset of convection in the Madden-Julian oscillation. *J. Climate,* **14**, 780-793.

[49] Kessler, W. S., , M. J. McPhaden, and K. M. Weickmann, 1995: Forcing of intraseasonal Kelvin waves in the equatorial Pacific. *J. Geophys. Res.*, **100**, 10613-10631.

[50] Kessler, W. and R. Kleeman, 2000: Rectification of the Madden-Julian Oscillation into the ENSO cycle. *J. Climate*, **13**, 3560-3575.

[51] Kikuchi, K., and Y. N. Takayabu, 2004: The development of organized convection associated with the MJO during TOGA COARE IOP: Trimodal characteristics, *Geophys. Res. Lett.*, **31**, L10101, doi:10.1029/2004GL019601.

[52] Krishnamurti, T. N., D. K. Oosterhof, and A. V. Mehta, 1988: Airsea interaction on the time scale of 30 to 50 days, *J. Atmos. Sci.*, **45**, 1304-1322.

[53] Kuma, K. I., 1994: The Madden and Julian and tropical disturbances in an aqua-planet version of JMA global model with T63 and T159 resolution. *J. Meteor. Soc. Japan,* **72**, 147-172.

[54] Lau, K.-M., and L. Peng 1987: Origin of low-frequency (intraseasonal) oscillations in the tropical atmosphere. Part I: Basic theory, *J. Atmos. Sci.*, **44**, 950-972.

[55] Lau, K.M., P.H. Chan, 1986: The 4050 Day Oscillation and the El Ni no/Southern Oscillation: A New Perspective. *Bull. Amer. Meteor. Soc.*, **67**, 533-535.

[56] Lau, K.-M., P. H. Chan, 1988: Intraseasonal and Interannual Variations of Tropical Convection: A Possible Link between the 4050 Day Oscillation and ENSO? *J. Atmos. Sci.*, **45**, 506-521.

[57] Lau, K.-M., H.-T. Wu, and S. Bony, 1997: The role of large-scale atmospheric circulation in the relationship between tropical convection and sea surface temperature. *J. Climate*, **10**, 381-392.

[58] Lau, K.-M., and C.-H. Sui. 1997: Mechanisms of Short-Term Sea Surface Temperature Regulation: Observations during TOGA COARE. *J. Climate*, **10**, 465-472.

[59] Lawrence, D, and P. J. Webster, 2002: The boreal summer intraseasonal oscillation and the South Asian monsoon. *J. Atmos. Sci.*, **59**, 1593-1606.

[60] Lee, M.-I., I.-S. Kang, J.-K. Kim, and B. E. Mapes, 2001: Influence of cloud-radiation interaction on simulating tropical intraseasonal oscillation with an atmospheric general circulation model. *J. Geophys. Res.*, **106**, 14219-14233.

[61] Liebmann, B., and C. A. Smith, 1996: Description of a complete (interpolated) outgoing longwave radiation dataset. *Bull. Amer. Meteor. Soc.*, **77**, 1275-1277.

[62] Liebmann, B, and D. L. Hartmann, 1984: An Observational Study of Tropical-Midlatitude Interaction on Intraseasonal Time Scales During Winter. *J. Atmos. Sci*, **41**, 3333-3350.

[63] Lin, X., and R. H. Johnson., 1996: Kinematic and Thermodynamic Characteristics of the Flow over the Western Pacific Warm Pool during TOGA COARE. *J. Atmos. Sci.*, **53**, 695-715.

[64] Lin, J.L., G.N. Kiladis, B.E. Mapes, K.M. Weickmann, K.R. Sperber, W.Y. Lin, M. Wheeler, S.D. Schubert, A. Del Genio, L.J. Donner, S. Emori, J.-F. Gueremy, F. Hourdin, P.J. Rasch, E. Roeckner, and J.F. Scinocca, 2006a: Tropical intraseasonal variability in 14 IPCC AR4 climate models. Part I: Convective signals. *J. Climate,* **19**, 2665-2690.

[65] Lin, J.L., G.N. Kiladis, B.E. Mapes, and K.M. Weickmann, 2006b: Tropical intraseasonal variability in DEMETER seasonal-to-interannual prediction models. *Quart. J. Roy. Meteor. Soc.*, submitted.

[66] Lin, J. L., B. E. Mapes, M. H. Zhang and M. Newman, 2004: Stratiform precipitation, vertical heating profiles, and the Madden-Julian Oscillation. *J. Atmos. Sci.*, **61**, 296-309.

[67] Lin, J. L., and B. E. Mapes, 2004: Radiation budget of the tropical intraseasonal oscillation. *J. Atmos. Sci.*, **61**, 2050-2062.

[68] Liu, G., J.A. Curry, and R.S. Sheu, 1995: Classification of clouds over the western equatorial Pacific Ocean using combined infrared and microwave satellite data. *J. Geophys. Res.*, **100**,13811-13826.

[69] Loschnigg, J., and P. J. Webster, 2000: A coupled ocean-atmosphere system of SST regulation for the Indian Ocean. *J. Climate,* **13**, 3342-3360.

[70] Lukas, R., and E. J. Lindstrom, 1991: The mixed layer of the western equatorial Pacific Ocean. *J. Geophys. Res.*, **96**, 3343-3357.

[71] Madden, R. A., and P. R. Julian, 1972: Description of global-scale circulation cells in the tropics with a 40-50 day period. *J. Atmos. Sci.*, **29**, 1109-1123.

[72] Madden, R. A., and P. R. Julian, 1994: Observations of the 40-50 day tropical oscillation: *A review. Mon. Weather Rev.*, **122**, 813-837.

[73] Maloney, E., and D. Hartmann, 1998: Frictional moisture convergence in a composite life cycle of the Madden-Julian oscillation. *J. Climate*, **11**, 2387-2403.

[74] Maloney, E. D. and Hartmann, D. L., 2000: Modulation of hurricane activity in the Gulf of Mexico by the Madden-Julian oscillation. *Science*, **287**,2002-2004.

[75] McPhaden, M. J., and B. A. Taft, 1988: Dynamics of seasonal and intraseasonal variability in the eastern equatorial Pacific. *J. Phys. Oceanogr.*, **18**, 1713-1732.

[76] McPhaden, M. J., 1999: Genesis and evolution of the 1997-98 El Nio. *Science*, **283**, 950-954.

[77] Mellor, G. L., and T. Yamada, 1982: Development of a turbulence closure model for geophysical fluid problems, *Rev. Geophys. Space Phys.*, **20**,851-875, .

[78] Mo, K. C., 2000: Intraseasonal Modulation of Summer Precipitation over North America. *Mon. Wea. Rev.*, **128**, 1490-1505.

[79] Mo, K. C.,and R. W. Higgins, 1998a: Tropical Influences on California Precipitation. *J. Climate*, **11**, 412-430.

[80] Mo, K. C., and R. W. Higgins, 1998b: Tropical convection and precipitation regimes in the western United States. *J. Climate*, **11**, 2404-2423.

[81] Nakazawa, T., 1988: Tropical super clusters within intraseasonal variations over the western Pacific. *J. Meteor Soc. Japan,* **66**, 823-839.

[82] Nogues-Paegle, J., and K. C. Mo, 1997: Alternating Wet and Dry Conditions over South America during Summer. *Mon. Wea. Rev.*, **125**, 279-291.

[83] Palmer, T. N., and D. A. Mansfield, 1984: Response of two atmospheric general circulation models to sea-surface temperature anomalies in the tropical east and west Pacific. *Nature*, **310**, 483-485.

[84] Park, C. K., D. M. Straus, and K.-M. Lau, 1990: An evaluation of the structure of tropical intraseasonal oscillations in three general circulation models. *J. Meteor. Soc. Japan,* **68**, 403-417.

[85] Peixoto, J.P., and A.H. Oort, 1992: *Physics of Climate*. American Institute of Physics, 520 pp.

[86] Paegle, J. N., L. A. Byerle, and K. C. Mo, 2000: Intraseasonal modulation of South American summer precipitation, *Mon. Wea. Rev.*, **128**, 837-850.

[87] Randall, D.A., K.-M. Xu, R.C.J. Somerville, and S. Iacobellis, 1996: Single-Column Models and Cloud Ensemble Models as Links between Observations and Climate Models. *J. Climate*, **9**, 1683-1697.

[88] Randall, D. A., and D. C. Cripe, 1999: Alternative methods for specification of observed forcing in single-column models and cloud system models. *J. Geophys. Res.*, **104**, 24527-24546.

[89] Rossow, W.B., and L.C. Garder, 1993: Cloud detection using satellite measurements of infrared and visible radiances for ISCCP. *J. Climate*, **6**, 2370-2393.

[90] Schlüssel, P., A. V. Soloviev, and W. J. Emery, 1997: Cool and fresh water skin of the ocean during rainfall. *Bound.-Layer Meteor.*, **82**, 437-472.

[91] Shinoda, T., H. H. Hendon, and J. Glick, 1998: Intraseasonal variability of surface fluxes and sea surface temperature in the tropical western Pacific and Indian Oceans. *J. Climate*, **11**, 1685-1702.

[92] Simmons, A. J., and J. K. Gibson, 2000: *The ERA-40 project plan*, ERA-40 Proj. Rep. Ser. 1, 62 pp., ECMWF, Reading, UK.

[93] Slingo, J. M., and Coauthors, 1996: Intraseasonal oscillations in 15 atmospheric general circulation models: Results from an AMIP diagnostic subproject. *Climate Dyn.*, **12**, 325-357.

[94] Slingo, J. M., 1987: The development and verification of a cloud prediction scheme for the ECMWF model. *Quart. J. Roy. Meteor.Soc.*, **113**, 899-927.

[95] Spencer, J.W., 1971: *Fourier series representation of the position of the Sun.* Search 2(5): 172 pp

[96] Stephens, G. L., P. J. Webster, R. H. Johnson, R. Engelen, and T. L'Ecuyer, 2004: Observational Evidence for the Mutual Regulation of the Tropical Hydrological Cycle and Tropical Sea Surface Temperatures. *J. Climate* **17**, 2213-2224.

[97] Stephens, G. L., and Coauthors, 2002: The CloudSAT Mission and the A-TRAIN. *Bull. Amer. Meteor. Soc.* **83**, 1771-1790.

[98] Sui, C. H. and K. M. Lau, 1992: Multiscale phenomena in the tropical atmosphere over the western pacific, *Mon. Wea. Rev.*, **120**, 407-430.

[99] Terray, L., E. Sevault, E. Guilyardi and O. Thual, 1995: *OASIS 2.0*, user's guide and reference manual. Technical report. [Available from CERFACS, France].

[100] Tiedtke, M., 1989: A comprehensive mass flux scheme for cumulus parameterization in large-scale models. *Mon. Wea. Rev.*, **117**, 1779-1800.

[101] Tompkins, A. M., 2001: On the Relationship between Tropical Convection and Sea Surface Temperature. *J. Climate*, **14**, 633-637. DOI: 10.1175/1520-0442(2001)014¡0633:OTRBTC¿2.0.CO;2

[102] Vitart, F. 2004: Monthly Forecasting at ECMWF. *Mon. Wea. Rev.* **132**, 2761-2779.

[103] Waliser, D. E., and N. E. Graham, 1993: Convective cloud systems and warm-pool sea surface temperatures: Coupled interactions and self-regulation. *J. Geophys. Res.*, **98** (D7), 12881-12893.

[104] Waliser, D. E., K. M. Lau, W. Stern and C. Jones. 2003a: Potential Predictability of the Madden-Julian Oscillation. *Bull. Amer. Meteor. Soc.* **84**, 33-50.

[105] Waliser, D. E., and Coauthors, 2003b: AGCM simulations of intraseasonal variability associated with the Asian summer monsoon. *Climate Dyn.*, **21**, 423-446.

[106] Waliser, D., S. Schubert, A. Kumar, K. Weickmann, and R. Dole, 2003c: Proceedings from a workshop on "Modeling, Simulation and Forecasting of Subseasonal Variability", *NASA/CP 2003-104606*, **25**, 62.

[107] Waliser, D. E., K. M. Lau, and J. H. Kim, 1999: The influence of coupled sea surface temperatures on the Madden-Julian oscillation: A model perturbation experiment. *J. Atmos. Sci.*, **56**, 333-358.

[108] Wang, B., P. J. Webster, and H. Teng, 2005: Antecedents and self-induction of active-break south Asian monsoon unraveled by satellites, *Geophys. Res. Lett.*, **32**, L04704, doi:10.1029/2004GL020996.

[109] Wang, J., H. L. Cole, D. J. Carlson, E. R. Miller, K. Beierle, A. Paukkunen, and T. K. Laine, 2002: Corrections of Humidity Measurement Errors from

the Vaisala RS80 Radiosonde-Application to TOGA COARE Data. *J. Atmos. Oceanic Tech.*, **19**, 981-1002.

[110] Wang, B., and X. Xie, 1998: Coupled modes of the warm pool climate system. Part I: The role of air-sea interaction in maintaining Madden-Julian oscillation. *J. Climate,* **11**, 2116-2135.

[111] Weare, B. C., P. T. Strub and M. D. Samuel, 1980: *Marine Climate Atlas of the Tropical Pacific Ocean*, Dept. of Land, Air and Water Resources, University of California, Davis.

[112] Webster, P. and C. Hoyos 2004: Prediction of Monsoon Rainfall and River Discharge on 15-30-Day Time Scales. *Bull. Amer. Meteor. Soc.*, **85**, 1745-1765.

[113] Webster, P. J., E. F. Bradley, C. W. Fairall, J. S. Godfrey, P. Hacker, R. A. Hopuze jr., R. Lukas, Y. Serra, J. M. Hummon, T. D. M. Lawrence, C. A. Russel, M. N. Ryan, K. sahami, P. Zuidema, 2002: The Joint Air-Sea Monsoon Interaction Experiment (JASMINE) Pilot Study. *Bull. Amer. Met. Soc.*, **83**, 1603-1630.

[114] Webster, P., C. A. Clayson and J. A. Curry. 1996: Clouds, Radiation, and the Diurnal Cycle of Sea Surface Temperature in the Tropical Western Pacific. *J. Climate*, **9**, 1712-1730.

[115] Webster, P. J., 1994: The Role of Hydrological Processes in Ocean-Atmosphere Interaction. *Rev. of Geophys.*, **32**, 427-476.

[116] Webster, P. J., and R. Lukas, 1992: TOGA-COARE: The Coupled Ocean-Atmosphere Response Experiment. *Bull. Amer. Meteor. Soc.*, **73**, 1377-1416.

[117] Webster, P. J., 1972: Response of the Tropical Atmosphere to Local, Steady Forcing. *Mon. Wea. Rev.*, **100**, 518-541.

[118] Weickmann, K. M., 1991: El-Nio Southern Oscillation and Madden-Julian (30-60 day) Oscillations during 1981-1982. *J. Geophys. Res.*, **96C**, 3187-3195.

[119] Weickmann, K. M., 1983: Intraseasonal circulation and outgoing longwave radiation modes during Northern Hemisphere winter, *Mon. Weather Rev.*, **111**, 1838-1858.

[120] Weller, R.A., and S.P. Anderson, 1996: Surface meteorology and air-sea fluxes in the western equatorial Pacific warm pool during the TOGA Coupled Ocean Atmosphere Response Experiment. *J. Climate*, **9**, 1959-1990.

[121] Wheeler, M., and G. N. Kiladis, 1999: Convectively Coupled Equatorial Waves: Analysis of Clouds and Temperature in the Wavenumber-Frequency Domain. *J. . Atmos. Sci.*, **56**, 374-399.

[122] Whitaker, J.S. and K.M. Weickmann, 2001: Subseasonal variations of tropical convection and week two prediction of wintertime western North American rainfall. *J. Climate*, **14**, 1524-1534.

[123] Whitlock, C. H., and Coauthors, 1995: First global WCRP shortwave surface radiation budget dataset. *Bull. Amer. Meteor. Soc.*, **76**, 905-922.

[124] Wick, G., 1995: Evaluation of the variability and predictability of the bulk-skin SST difference with application to satellite-measured SST. Ph.D. thesis, University of Colorado, Boulder, CO, 139 pp.

[125] Wolff, J. E., E. Maier-Reimer and S. Legutzke, 1997: *The Hamburg Ocean Primitive Equation Model*. Deutsches Klimarechenznetrum, Hamburg, Technical Report No. **13**.

[126] Woolnough, S. J., J. M. Slingo, and B. J. Hoskins. 2000: The Relationship between Convection and Sea Surface Temperature on Intraseasonal Timescales. *J. Climate*, **13**, 2086-2104.

[127] Yasunari, T., 1980: A quasi-stationary appearance of the 30-40 day period in the cloudiness uctuations during the summer monsoon over India. *J. Meteorol. Soc. Jpn*, **58**, 225-229.

[128] Zhang, C., 2005: Madden-Julian Oscillation. *Rev. Geophy.*, **43**, RG2003, doi: 10.1029/2004RG000158.

[129] Zhang, C. and M. J. McPhaden, 2000: Intraseasonal Surface Cooling in the Equatorial Western Pacific. *J. Climate,* **13**, 2261-2276.

[130] Zhang, C., 1996: Atmospheric intraseasonal variability at the surface in the western Pacific Ocean, *J. Atmos. Sci.*, **53**, 739-785.

[131] Zhang, G.J. and N. A. McFarlane, 1995: Sensitivity of climate simulations to the parameterization of cumulus convection in the CCC-GCM. *Atmos.-Ocean*, **3**, 407-446.

[132] Zheng, Y., D. E. Waliser, W. Stern, and C. Jones, 2004: The role of coupled sea surface temperatures in the simulation of the tropical intraseasonal oscillation. *J. Climate*, **17**, 4109-4134.